Cretaceous Palaeogeography of Eastern Australia: Connecting the Deep Earth to Surface Processes

Kara Matthews

Supervisors:

Professor Dietmar Müller

Dr Alina Hale

Thesis submitted in partial fulfilment of the requirements for Honours,

The University of Sydney,

2009

Acknowledgements

Thank you SO much Dietmar for absolutely everything this year. I am forever grateful for the opportunities you've provided me, and for all your guidance and support. Thanks too for your super-human patience when explaining the backstripping procedure (over and over and over again)…I *think* I finally get it! A million thanks Alina for all your patience this year explaining everything from the physics behind mantle convection to Python scripting! I absolutely could not have come this far without your help and enthusiasm, and all the analogies you made up to explain various physics principles.

Grace…where to start? Thank you so much for being such an amazing friend this year. I can say without a doubt that Honours wouldn't have been the same without you! The countless tea breaks, thai lunches and conversations about anything and everything got me through this year and made it loads of fun despite all the stress.

Thanks Mike for the time you spent with me at Caltech helping to better define my project. Your comments, suggestions and explanations throughout the year were also muchly appreciated. Thanks too, to Lydia for the time you spent with me at Caltech and for providing me with the framework from which my project evolved.

Thank you Sabin for making this year so much fun, for always being there for a good old chat…and for solving my computer dilemmas with a smile!! Thanks to everyone in EarthByte for providing such a fun and supportive working environment. Thank you Maria for always being there to answer my millions of questions about everything, and thanks Jo for getting me through those dark abstract writing days!

Mum and Dad, I can never thank you both enough for your love and support, and for teaching me the importance of working hard and being inquisitive. I would never have achieved this much without your encouragement. Thank you so much Steve for all your support this year! Despite being SO far away, you were always there to encourage me and remind me that I can do anything I put my mind to. Thanks Louise for being such a positive influence this year, and for initiating so many hot chocolate outings! Thanks too, to Vashti for always checking up on me and making sure that I wasn't feeling too stressed.

Abstract

We have used the geodynamic modelling software *CitcomS 3.0* to model the surface evolution of Australia since 140 Ma and constrain the location of the Cretaceous aged subduction zone that paralleled its eastern margin. Australia's palaeogeography was profoundly affected by mantle convection processes during the Cretaceous. Eastward passage of the Australian plate over subducted slab material induced negative dynamic topography in eastern Australia, causing widespread time-dependent subsidence and formation of a vast epeiric sea during a eustatic sea-level low. Although there exists a considerable amount of geological evidence for active convergence between Australia and the palaeo-Pacific at this time, the exact location of the subduction zone has remained elusive. To constrain the location of subduction we tested two end-member models, one with the subduction zone directly adjacent to the continent, and an alternative model with subduction translated 23° east. Our forward geodynamic models incorporate a rheological model for the mantle and crust, plate motions since 140 Ma and evolving plate boundaries, implemented in the *GPlates* software. While mantle rheology affects the magnitude of surface vertical motions, the timing of uplift and subsidence depends critically on plate kinematic reconstructions and plate boundary geometries. Tectonic subsidence analysis using the backstrippping method was performed on 42 wells from the Eromanga and Surat basins in eastern Australia. This revealed Cretaceous tectonic subsidence trends with which to compare our modelled dynamic topography. Simulations with subduction proximal to the active continental margin resulted in accelerated basin subsidence delayed by 20 Myr compared with these tectonic subsidence data. However this timing offset was reconciled when subduction was shifted eastward. Comparisons between whole mantle seismic tomography images and equivalent model temperature cross-sections further validate our proposed eastward shift in subduction. Finally an absence of subduction zone volcanism along Australia's east coast in the Early Cretaceous supports our conclusion that a back-arc basin existed east of Australia during the Cretaceous. Our models further allowed us to test alternative Tertiary plate boundary geometries east of Australia, in particular whether or not the proposed short-lived mid-Tertiary eastward dipping "New Caledonia subduction zone" may have been responsible for a prominent fast shear wave anomaly at ~1100 km depth beneath the Tasman Sea. Our models suggest that post 45 Ma westward dipping subduction along the Tonga-Kermadec Trench may have produced the slab material mapped by mantle tomography models in the lower mantle underneath the

Tasman Sea. An additional eastward dipping subduction zone does not appear to be required by the tomographic images, as proposed previously.

Contents

Table of Figures

List of Tables

1 Introduction

Plate tectonics and mantle convection have been shaping the surface of the Earth for billions of years. They form a highly complex, dynamically coupled system that is constantly modifying geological environments over a range of timescales. During the Cretaceous the palaeogeography of Australia was profoundly influenced by mantle processes. A vast inland sea dominated the eastern interior for 10 Myr (Exon and Senior, 1976), despite eustatic sea-level lows. These seemingly inconsistent phenomena are attributed to the eastward passage of the Australian plate over subducted oceanic lithosphere, originating from a subduction zone that separated Eastern Gondwanaland from the palaeo-Pacific Ocean (Panthalassa) (e.g. Veevers, 1984; Russell and Gurnis, 1994; Gurnis et al., 1998; Waschbusch et al., 2009). Subduction zones feed cold dense slabs into the mantle. These descending slabs have the propensity to viscously drag down the overlying crust, causing widespread time-dependent subsidence (Mitrovica et al., 1989). Although there exists a strong body of evidence to support dynamic vertical motions of the Australian continent since the Mesozoic, a geodynamic model for eastern Australia during the Cretaceous remains elusive. Additionally, the location of the subduction zone that spanned the eastern margin of Eastern Gondwanaland is poorly constrained; this is despite a wealth of knowledge concerning its earlier evolution during the Late Paleozoic to mid-Triassic (e.g. Jenkins et al., 2002).

Technological advances in high-performance computing and improvements to computer modelling software are facilitating endeavours to reconstruct the evolving surface of the Earth over timescales of millions of years. Modelling has become so robust that time-dependent geological data sets can be assimilated into global models, with smaller regions defined for higher-resolution investigations. In essence, these coupled models (Tan et al., 2006) represent an integrated approach to the study of geodynamics. By incorporating plate kinematics, evolving plate boundaries and crustal and mantle rheologies, current geodynamic modelling enables the most fundamental drivers of geological evolution to be closely scrutinised.

These geodynamic modelling technologies will be applied to the Australian region, from 140-0 Ma, in order to reconstruct surface vertical motions and constrain the location of the subduction zone that paralleled Eastern Gondwanaland during the Cretaceous. This information can be incorporated into current plate reconstruction models, whereby improving future geodynamic and kinematic modelling endeavours.

2 Objectives and Significance

2.1 Objectives

Our investigation has four primary aims. We endeavour to produce a geodynamic model for the Australian region for the Cretaceous that accurately reconstructs the large-scale vertical motions that have been identified from the sedimentary record. We also aim to constrain the location of the subduction zone that formed the eastern plate boundary. The Eromanga and Surat basins in the eastern interior will be the focus of our investigation, as their formation and evolution are critically linked to the dynamics of the subduction zone that formed the eastern plate boundary. Additionally, we aim to develop and employ a workflow that links a well-established high-performance computing software, the *CitcomS* mantle convection code, to a recently developed version of the *GPlates* software for plate kinematic reconstructions. Further we aim to link both geodynamic model outputs as well as geological and geophysical observations to the Generic Mapping Tools for post-processing and visualisation via the development of Python scripts. Comparisons with borehole tectonic subsidence curves will enable us to quantify the model's consistency with geological data. Seismic tomography will enable us to further validate the model and test its temporal robustness, as it will allow us to compare our predicted mantle structure with current tomography models for the southwest Pacific.

2.2 Significance

Geodynamic modelling allows us to analyse, quantify and visualise coupled deep Earth and surface processes that occur over timescales of millions of years. Increasing our understanding of events in the geological past improves our ability to understand present-day surface geologies and how they evolved. Constraining the plate boundary between Australia and the palaeo-Pacific (the Phoenix plate) at 140 Ma will facilitate future geophysical investigations. It will be possible to incorporate our plate boundary data into new plate reconstruction models used in studies of Eastern Gondwanaland and the early development of the southwest Pacific.

The Eromanga Basin in eastern Australia forms a significant portion of Australia's largest onshore hydrocarbon field, with its hydrocarbon potential recognised at least as early as 1924 (Armstrong and Barr, 1986). Large volumes of coal, oil and gas have been extracted from its Mesozoic strata, yet the Basin still remains highly unexplored compared to deeper Palaeozoic basins. The effects of mantle driven topography on oil forming basins are poorly understood. Therefore, at a time of global oil shortages it is critical to invest in research that aids exploration for new fields. A number of opal fields also lie in the Eromanga and Surat basins, with host-rocks being Cretaceous in age. Australia is a major producer of precious opals, and contributes to 95% of global production (Horton, 2002). The formation and preservation of both hydrocarbons and opals depends on palaeo-environments and crustal evolution, respectively. This further emphasises the importance of developing a geodynamic model for the surface evolution of Australia; that is, it holds the potential to aid future hydrocarbon and opal exploration efforts.

3 Background

3.1 Mantle Convection and Plate Tectonics – Setting the context

Plate tectonics is the surface expression of mantle convection. This is the ultimate connection between deep Earth and surface processes. In accordance with basic thermal convection, heat is redistributed via circulating fluid motion. In regions of plate convergence, subduction zones feed cold, dense, negatively buoyant oceanic crust into the upper mantle. To preserve conservation of matter, large-scale diffuse upwellings passively rise to impinge on the base of the lithosphere at regions away from subduction. These hot upwellings of lower density buoyant mantle material drive the creation of new oceanic crust at divergent margins. Plumes originating from convective instabilities also contribute to the convective cycle. They actively ascend through the mantle, forming hotspots, and in some instances contribute to the creation of new crust at mid-ocean ridges and cause spreading asymmetries (Müller et al., 1998).

This coupled, deep Earth to surface, system is responsible for producing the constantly evolving surface geology observable today, such as mountain ranges and volcanoes. Over hundreds of millions of years it has driven the formation and dispersal of supercontinents, continuously altered the Earth's climate through volcanism and control over circum-polar currents, deformed the Earth's surface whereby driving topography, and effectively redistributed heat from the mantle and core. Dynamic topography is one such surface phenomenon of mantle convection.

3.2 Dynamic Topography

Vertical motion of the Earth's surface, attributed to the passage of density anomalies through the mantle, is termed dynamic topography. Dynamic topography has contributed to Phanerozoic continental flooding (Gurnis, 1990), and recognising its influence has helped reconcile discrepancies between continental records of sea-level fluctuations and eustatic sea-level curves (e.g. Veevers, 1984; Lithgow-Bertelloni and Gurnis, 1997; Spasojević et al., 2008; DiCaprio et al., 2009). This phenomenon is not spatially restricted to the solid earth-fluid interface (Lithgow-Bertelloni and Gurnis, 1997). It can cause

deflection of internal boundary layers within the mantle, such as the 410 km and 660 km phase boundaries (Steinberger, 2007), as well as the core-mantle boundary.

Depending on the nature of the causal density anomaly, dynamic topography may be positive or negative; negative dynamic topography will be the focus of this investigation. Negative dynamic topography is related to the descent of positive density anomalies associated with past and present subduction (Figure 1). The downward passage of subducted slabs imparts a viscous drag on the overlying mantle, which in turn pulls the surface down. Positive dynamic topography, in contrast, is related to negative density anomalies, such as plumes, rising through the mantle and eventually impinging on the base of the lithosphere (Figure 1). The ascent of this anomalously buoyant material pushes the overlying mantle upwards, and consequently the overlying crust can be uplifted. The closer the density anomaly is to the surface, and the faster it is ascending or descending, the greater is its propensity to cause subsidence or uplift. Changes to the magnitude of dynamic topography results in relative subsidence or uplift of the surface. For example, diminishing influence of a sinking slab will result in relative surface uplift, despite a negative dynamic topography setting.

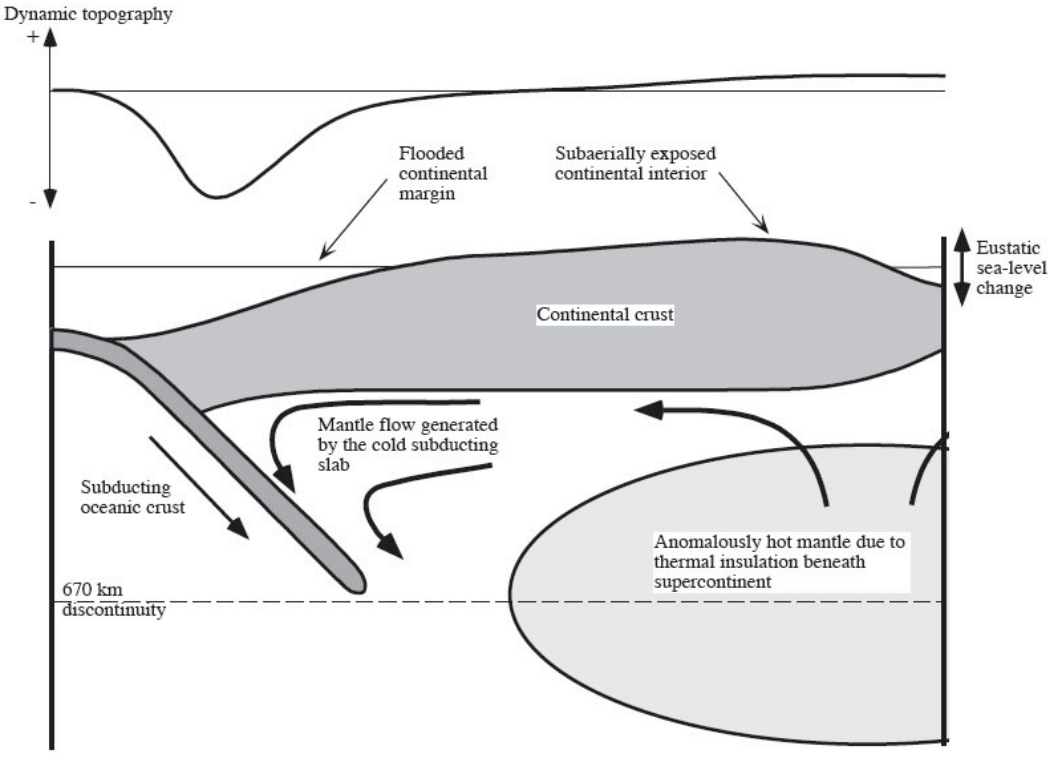

Figure 1. Schematic illustrating the relationship between dynamic topography and mantle flow (from Burgess et al., 1997). Descending cold slab material produces subsidence, whilst hotter more buoyant mantle material produces uplift.

As dynamic topography is intimately related to mantle convection, it naturally follows that major regions of long-wavelength subsidence and uplift are spatially and temporally related to zones of large-scale subduction and upwellings. The African and South Pacific 'superswells' are extensive regions of broadscale upwellings, whilst the western Pacific (particularly Southeast Asia) and South America are regions of widespread, presently active, subduction. Respectively they coincide with distinct regions of positive and negative dynamic topography (Figure 2). The African Superswell has produced positive dynamic topography that extends from the eastern and southern continental plateaux (such as the East African Plateau), where up to ~600 m of residual topography has been calculated (Lithgow-Bertelloni and Silver, 1998; Gurnis et al., 2000), into adjacent ocean basins where there is ~500 m of residual bathymetry (Nyblade and Robinson, 1994). Lithgow-Bertelloni and Silver (1998) attribute this laterally extensive deformation to upper and lower mantle negative density anomalies, originating from a core-mantle boundary upwelling.

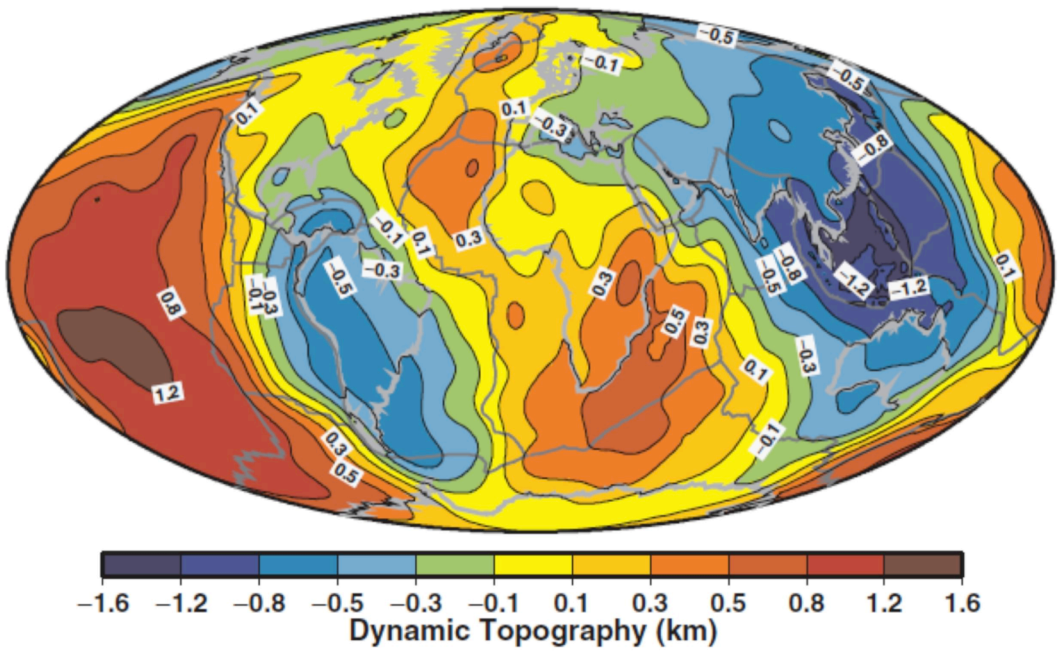

Figure 2. Dynamic topography for the whole mantle, with continents outlined in grey (from Conrad and Husson, 2009). Warmer colours correspond to uplift, and cooler colours to subsidence. The Pacific and African 'superswells', and the South American and western Pacific subduction zones, respectively form the four major regions of uplift and subsidence.

3.2.1 Temporal and Spatial Characteristics

Dynamic topography is transient, resulting in time dependent deformation. It is reversible, as the thermal anomaly itself exists for a finite period of time before it dissipates back into the convective cycle. For example, westward dipping Iapetus subduction beneath eastern North America in the Early Palaeozoic, resulted in long-wavelength downward tilting of the continent (Coakley and Gurnis, 1995; Burgess et al., 1997). When subduction terminated in the Early Silurian the crust rebounded and widespread erosion occurred. As a result, outcrop ages increase in the east and an unconformity characterises the sedimentary record ~420 Ma. Termination of eastward dipping Farallon subduction beneath western North America in the Neogene is also characterised by uplift, erosion and a subsequent stratigraphic unconformity (Burgess et al., 1997; Liu et al., 2008).

Currently, negative dynamic topography associated with subduction in the western Pacific is predicted to be decreasing due to the slab influence diminishing with depth; therefore invoking relative uplift (Figure 3) (Conrad and Husson, 2009). Whilst it is predicted that the uplift of Africa associated with the African Superswell will increase as mantle density anomalies continue to rise to the surface from the lower mantle (Figure 3) (Gurnis et al., 2000; Conrad and Husson, 2009). Geodynamic modelling suggests that the effects of dynamic topography may exist over a period of 100-200 Myr (Pysklywec and Mitrovica, 1998). In addition, motion between the overriding plate and the slab can result in the locus of maximum deflection migrating laterally away from the trench (Gurnis et al., 1998; Pysklywec and Mitrovica, 1998) producing an asymmetric accumulation of sediments (Pysklywec and Mitrovica, 1998).

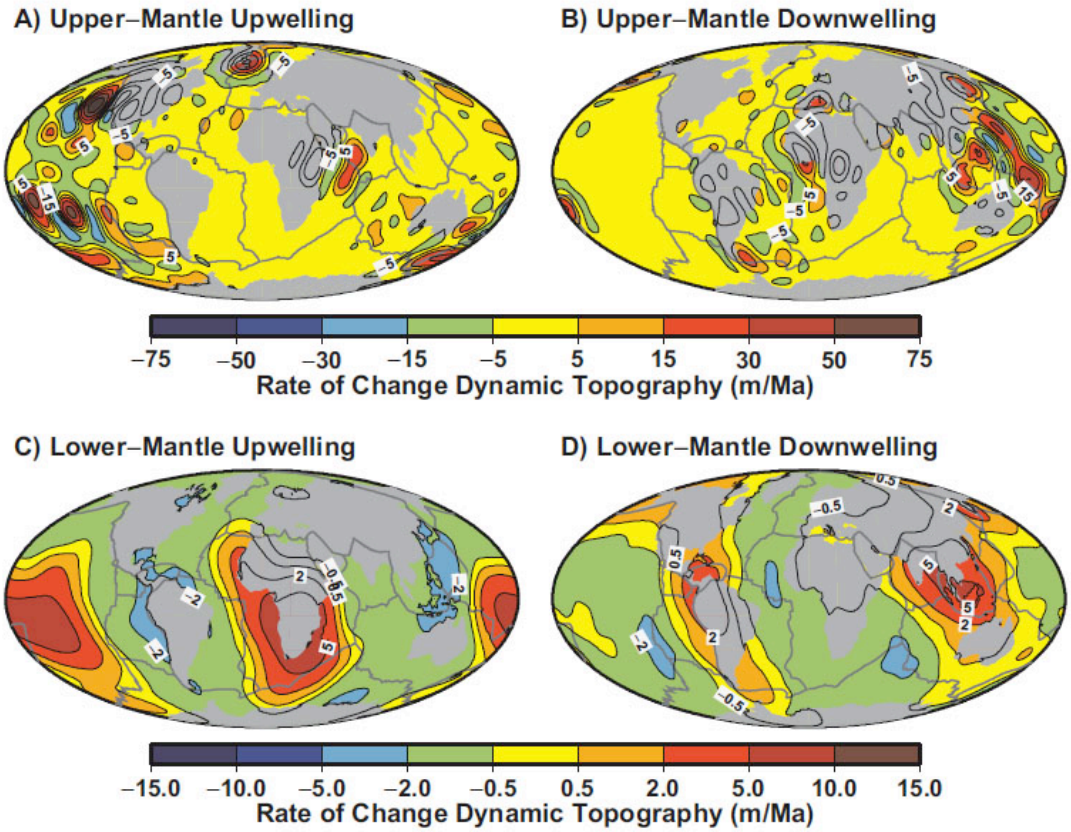

Figure 3. Rate of change of dynamic topography; corresponding to (A) upper-mantle upwellings and (B) downwellings, and (C) lower-mantle upwellings and (D) downwellings (from Conrad and Husson, 2009). The strengthening of the uplift signal beneath Africa is clearly illustrated in (C), which shows a positive rate of change in the region; the positive rate of change beneath Southeast Asia in (D), however, illustrates the predicted decrease in subsidence.

The horizontal extent of dynamic topography can reach over 1000 km (e.g. Mitrovica et al., 1989; Pysklywec and Mitrovica, 1998). The vertical component of dynamic topography, however, is a contentious issue (Wheeler and White, 2000; Sandiford, 2007). Observational case studies have typically yielded results on the order of several hundred metres (e.g. Wheeler and White, 2000; DiCaprio et al., 2009; Spasojevich et al., 2008), where as forward modelling supports surface deflections of over 1000 m (e.g. Pysklywec and Mitrovica, 1998; Lithgow-Bertelloni and Gurnis, 1997).

3.2.2 Significance of the 660 km Phase Boundary

The 660 km phase boundary separates the upper and lower mantle. It is an ‘olivine boundary’ where an endothermic phase change causes spinel to become unstable and change to the post-spinel minerals perovskite and magnesiowüstite. The interactions of

descending slabs with the 660 km phase boundary can have important implications for the fate of those slabs, as well as the evolution of negative surface dynamic topography (Pysklywec and Mitrovica, 1998; Steinberger, 2007).

There is a significant change in viscosity across this boundary between the upper and lower mantle, with the lower mantle at least 10 to 30 times more viscous (Gurnis and Hager, 1988), although estimates based on comparison with the geoid suggest a larger contrast (e.g. 50 times - Lithgow-Bertelloni and Gurnis, 1997). This increase in viscosity can act as an impediment to descending slabs, causing them to temporarily stagnate above the 660 km phase boundary before penetrating the lower mantle. Geodynamic modelling allowed Zhong and Gurnis (1997) to conclude that slab buoyancy (analogous to age) and trench mobility are the major controls on slab behaviour at this boundary.

Slab material from a fossil subduction zone between eastern Gondwanaland and the palaeo-Pacific (Panthalassa) is currently positioned beneath the Australian-Antarctic Discordance (AAD) (Gurnis et al., 1998). According to Gurnis et al. (1998), the slab material has partly stalled in the transition zone and, as a result of overlying plate divergence, is being drawn up by the South East Indian Ridge. Figure 4 shows residual depth anomalies for the Australian region. The seafloor is clearly significantly deeper in the vicinity of the AAD than predicted by an age-depth relationship.

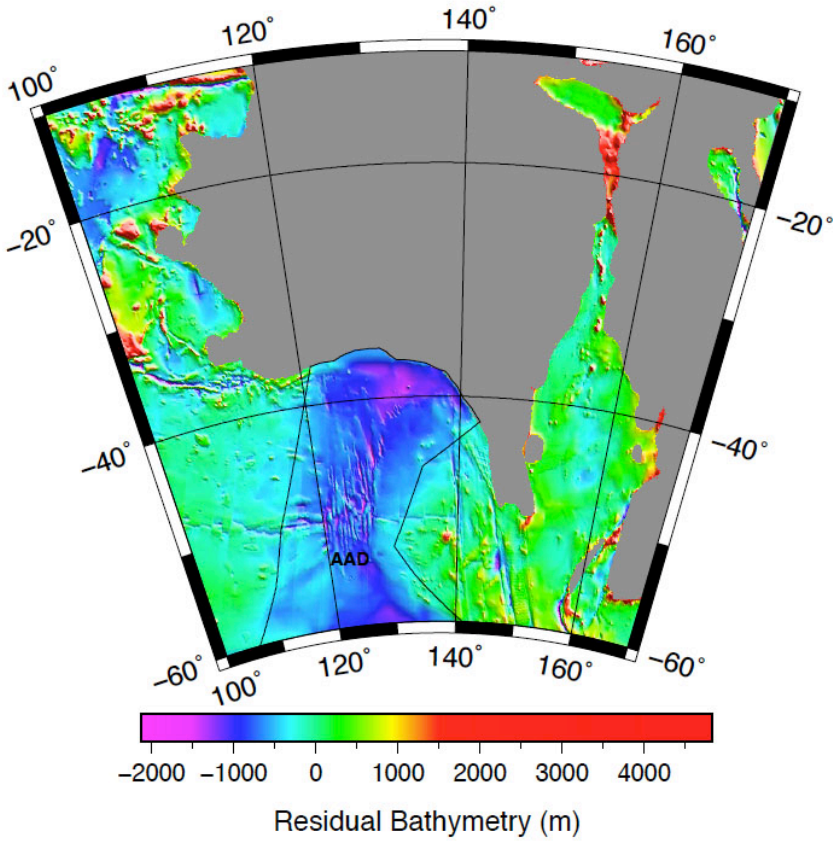

Figure 4. Residual bathymetry for the Australian region, computed using the age-depth relationship of Crosby (2007) and the age grid from Müller et al. (2008a). The Australian-Antarctic Depth Anomaly is outlined in black, continental crust is shaded grey, AAD – Australian-Antarctic Discordance.

The theoretical modelling of Pysklywec and Mitrovica (1998) suggests that slab material can stagnate in the transition zone for tens of millions of years. When the material eventually penetrates the lower mantle, episodes of large-scale mass transfer can cause part of the upper boundary layer to be dragged down with the flow (Figure 5) (Pysklywec and Mitrovica, 1998). These rare 'mantle avalanche' events are predicted to have a significant effect on surface dynamic topography, of up to ~2.5 km vertically and ~2500 km horizontally (Pysklywec and Mitrovica, 1997). Pysklywec and Mitrovica (1997) consider that a mantle avalanche may have produced dynamic topography in Western Canada during the Devonian and Carboniferous.

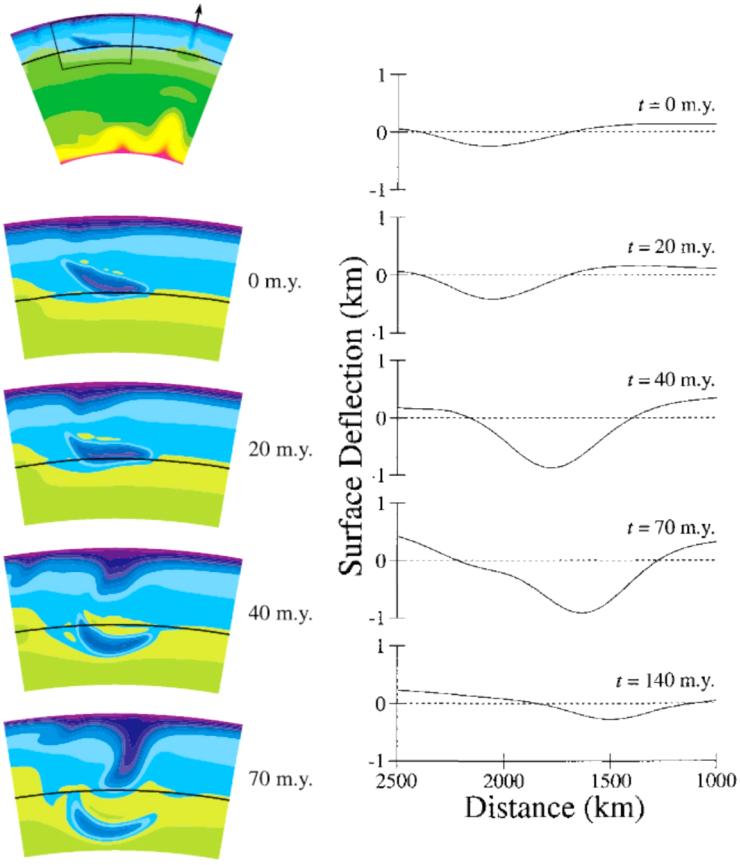

Figure 5. Pysklywec and Mitrovica's (1998) model of a subducted slab descending through the mantle. After being stalled for >20 Myr at the 660 km boundary (black line), the slab penetrates the lower mantle as a 'mantle avalanche' and causes the overlying material to be dragged down. Surface deflection is at a maximum during this event. The decrease in surface deflection at 140 Myr reflects the time dependence of dynamic topography. This figure also illustrates that surface deflection can migrate laterally.

3.3 Tectonic History of Eastern Australia

Surface plate boundary configuration has a profound influence on the evolution of continental geography and geomorphology. The intra-plate position of Australia, within the Indo-Australian Plate, contributes to its current tectonic stability. Fossil divergent margins border the continent to the east and west, whilst active convergent and divergent margins are hundreds of kilometres away to the north and south, respectively. In geologically resent times, however, Australia was dominated by very contrasting tectonic environments that have played a major role in shaping the present terrain.

Sites of Permian-Triassic and Jurassic-Eocene subduction form an extensive band bordering the present-day western Pacific: its continuation around the 'rim of fire'

separates the hot upper mantle of the Indian Ocean from that of the Pacific Ocean (Figure 6) (Anderson, 1994). According to Anderson (1994) continents have repeatedly moved towards these zones during supercontinent dispersal. The evolution of eastern Australia has been influenced by these dynamics, most recently Jurassic-Cretaceous subduction.

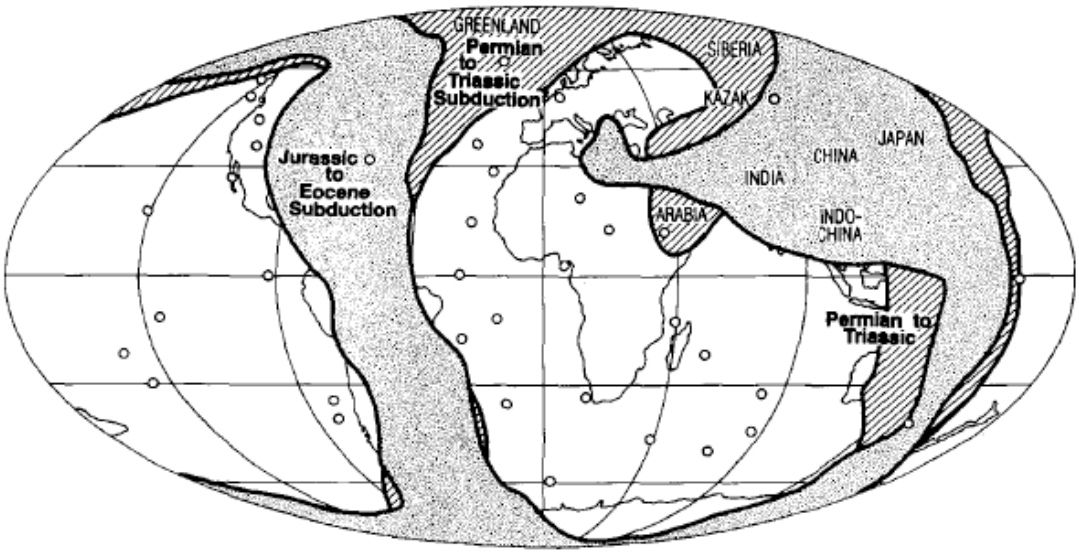

Figure 6. Jurassic to Eocene, and Permian to Triassic zones of subduction, and hotspot locations (circles) (from Anderson, 1994). It can be seen that subduction has tended to occur in the same regions.

During the Mesozoic a subduction zone paralleled the eastern margin of Eastern Gondwanaland, produced by convergence with the palaeo-Pacific (Figure 7). Convergence continued until early in the Late Cretaceous ~100 Ma (e.g. Veevers, 1984; Bradshaw, 1989; Laird and Bradshaw, 2004). Although, based on timing of metamorphism in the Southern Alps of New Zealand, Vry et al. (2004) propose it may have persisted until ~85 Ma along the New Zealand portion of the margin (south of Australia), ending with the oblique collision with the Hikurangi Plateau. These spatial and temporal observations suggest a southward decrease in the age of cessation.

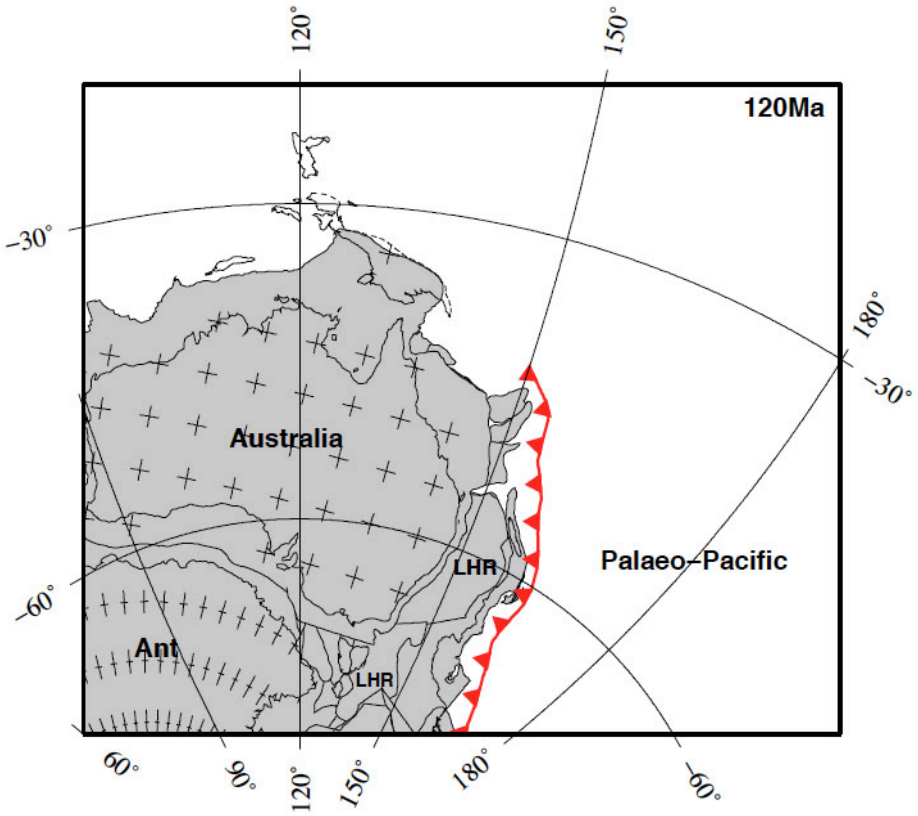

Figure 7. Tectonic reconstruction at 120Ma showing a convergent margin between Eastern Gondwanaland and the palaeo-Pacific. Ant – Antarctica, LHR – Lord Howe Rise.

The ensuing rifting and spreading of the Tasman Sea signified a change in the stress regime of the western palaeo-Pacific (Veevers, 2000). Tulloch and Kimbrough (1989) propose that an "extensional corridor" paralleled the convergent margin even before Tasman Sea rifting commenced. Evidence for Cretaceous extension related volcanism is preserved on island groups off the central Queensland coast and in the Maryborough Basin on the south Queensland coast, as well as the Lord Howe Rise and New Caledonia, rifted fragments of eastern Gondwanaland (Ewart et al., 1992). A major Cretaceous volcanic event ~120-105 Ma in the Whitsundays Volcanic Province (central Queensland) (Ewart et al., 1992), contributed to the volcanogenic sediment record of the eastern Australian basins; sediments were even dispersed as far south as the Otway and Gippsland basins along Australia's southeastern margin (Bryan et al., 1997).

Although convergence has been well established during the Cretaceous, the location of the subduction zone at this time remains uncertain. Whilst remnants of Palaeozoic convergent margin volcanism are abundant on the Australian continent (e.g. Leitch, 1975; Holcombe et al., 1997), evidence from the Cretaceous is limited (e.g. fluvial deposits of volcanic

detritus in eastern Australian basins – Veevers, 2000) and there remains much debate over the origin of these Cretaceous aged volcanics; whether they are convergence or extension related. Further more, the advance and retreat of the subduction zone during the Palaeozoic to Triassic demonstrates that subduction zones can be highly mobile (Jenkins et al., 2002; Holcombe et al., 1997). Therefore, subduction proximal to the continental margin during earlier Periods does not preclude a large back-arc region, with subduction several 100 km further east during the Cretaceous.

Regardless of the spatial aspects of Cretaceous subduction and the onset of extension, the change from convergence to divergence was a tectonically pivotal time. Veevers (1984, p.142) highlights that it was "*…a turning-point in the Phanerozoic history of Eastern Australia (that) cannot be overemphasized."*. Eastern Australia essentially evolved from a phase of tectonic activity to one of relative passivity.

3.4 Eastern Australian Basins

A succession of Permian-Triassic and Jurassic-Cretaceous intracratonic basins overlie Proterozoic and Palaeozoic rocks in eastern Australia. Two such basins, Eromanga and Surat, formed in the latter phase of basin development. The Eromanga-Surat Basin system covers an area of ~1.5×10^6 km^2 in eastern and central Australia (Figure 8), and overlies more than eleven pre-Jurassic basins, including the Bowen, Gunnedah, Cooper, Galilee, Pedirka, Simpson and Arkaringa basins. Along with the Carpentaria and Clarence-Moreton basins, the Eromanga and Surat basins comprise a dominant portion of the 1.7×10^6 km^2 Great Artesian Basin. Their surface evolution bears an interesting relationship with deep earth processes connected to Mesozoic subduction off eastern Australia; previous studies have found evidence for negative dynamic topography (e.g. Veevers, 1984; Gallagher et al., 1994; Russell and Gurnis, 1994; Waschbusch et al., 2009).

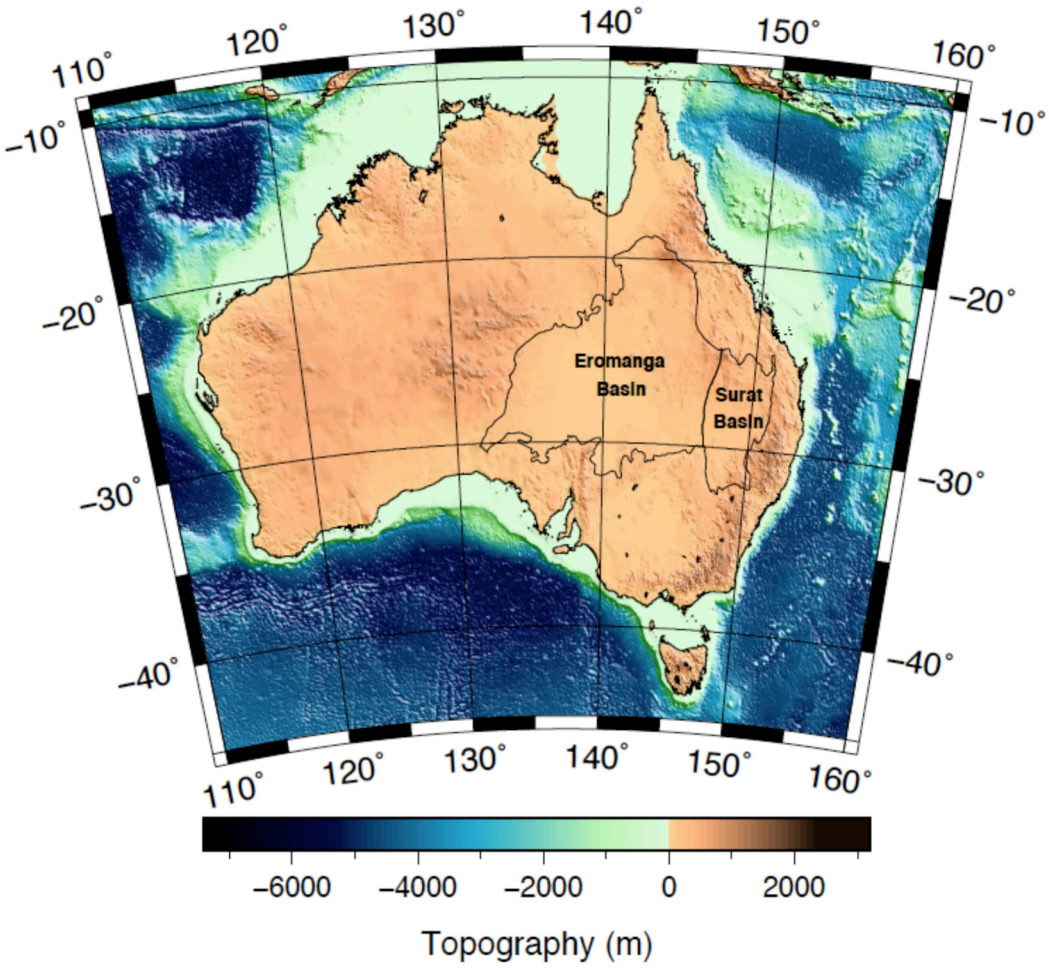

Figure 8. Topographic map of Australia showing the locations of the Eromanga and Surat basins.

3.4.1 Eromanga Basin

The Eromanga Basin is the most aerially extensive of the Jurassic-Cretaceous eastern Australian basins at ~1.2x10^6 km^2. It extends across four State/Territory borders (New South Wales, Queensland, Northern Territory and South Australia), between ~18°-32°S and ~132°-147°E (Figure 8). The Carpentaria Basin borders the Eromanga Basin to the north across the Euroka Arch; the Surat Basin, across the Nebine Ridge to the east; basement blocks and pre-Jurassic basins to the south and west. The maximum thickness of sediment preserved in the basin is ~2600 m (Draper, 2002). Extensive stratigraphic analysis of these preserved sediments elucidates the palaeogeography of the basin (e.g. Exon and Senior, 1976; Senior et al., 1978).

3.4.1.1 Palaeogeography

Freshwater conditions prevailed during the Jurassic, with sediments deposited in predominantly fluvial, and also lacustrine, environments. The porous and permeable, quartzose and arenaceous, sandstone layers form numerous aquifers across the basin, with the Hooray Sandstone being most fruitful (Senior et al., 1978). More localised lower energy swamp and deltaic environments facilitated the development of coal beds in several stratigraphic units.

Between the Early Cretaceous and the Late Albian-Early Cenomanian shallow marine conditions prevailed in the Basin. Transgression reached a maximum in the Aptian, however connection to the open ocean during this time was intermittently cut off (Senior et al., 1978). The Rolling Downs Group comprises the stratigraphic units laid down during this interval. It includes volcanogenic sands sourced from a northeasterly direction (e.g. Exon and Senior, 1976; Veevers, 1984). The thickness of volcanic deposits reaches an average of 500 m (Exon and Senior, 1976). The upper most unit of the Rolling Downs Group, and indeed the Eromanga Basin, is the Winton Formation. It was deposited in freshwater conditions following the final retreat of the sea to the north (Exon and Senior, 1976). See Table 1 for a summary of the generalised stratigraphy of the basin.

Table 1. Generalised stratigraphy of the Eromanga Basin (adapted from Exon and Senior, 1976; Senior et al., 1978).

Period	Stage/Epoch	Unit		Maximum Thickness (m)	Environment of Deposition and Lithology	Freshwater vs. Marine
Cretaceous	L. Albian to Cenomanian	Rolling Downs Group	Winton Formation	1200	*Fluvial and Minor Lacustrine*: Labile sandstone, siltstone and mudstone, mudclast conglomerate. Minor coal.	Freshwater
			Mackunda Formation	200	*Marine to Paralic*: Labile sandstone, siltstone and mudstone, mudclast conglomerate.	**Final Marine Retreat**
	L. Albian		Allaru Mudstone	270	*Shallow Marine*: Mudstone, siltstone. Minor fine-grained labile sandstone.	Predominantly Marine
			Toolebuc Formation	75	*Shallow Marine*: Shale, siltstone, labile sandstone.	
	L. Aptian to M. Albian		Wallumbilla Formation	350*	*Shallow Marine*: Mudstone and siltstone. Minor labile sandstone.	
	Neocomian to E. Aptian		Cadna-Owie Formation	80	*Paralic and Shallow Marine*: Quartzose to sublabile sandstone, and siltstone (increasing near base).	
			Hooray Sandstone	200	*Fluvial to Shallow Marine (in central west)*: Quartzose to sublabile sandstone, with interbeds of siltstone, conglomerate and coal.	**Marine Transgression**
Jurassic	L. Jurassic		Westbourne Formation	120	*Fluvial and Lacustrine*: Siltstone and mudstone. Minor quartzose to sublabile sandstone.	Freshwater
	M.–L. Jurassic		Adori Sandstone	71**	*Fluvial*: Quartzose to labile sandstone. Minor siltstone and mudstone.	
	M. Jurassic		Birkhead Formation	130*	*Fluvial and Lacustrine*: Siltstone, mudstone, labile sandstone. Minor coal.	
	E. Jurassic		Hutton Sandstone	250**	*Fluvial and Local Lacustrine*: Quartzose to sublabile sandstone, siltstone and mudstone. Minor conglomerate.	
		Unconformity (L.Triassic Erosion)				

* Northern Eromanga Basin
** Central Eromanga Basin

3.4.2 Surat Basin

The elongate N-S trending Surat Basin is ~$3x10^5$ km^2 and straddles the New South Wales-Queensland border between 24.5°S and 32°S (Figure 9). It is bordered to the north by the Bowen Basin which has been exposed by erosion; to the east by basement blocks of the New England Orogen and the Kumbarilla Ridge which is the western boundary of the Clarence-Moreton Basin; to the south by basement blocks of the Lachlan Fold Belt; to the west by the Nebine Ridge, the eastern boundary of the Eromanga Basin. Up to 2500 m of sediment have been preserved in the basin (Exon, 1976). This stratigraphic record helps chronicle the palaeogeography of the basin. Proximity and contemporaneous formation with the Eromanga Basin, accounts for the similarities in palaeogeography.

3.4.2.1 Palaeogeography

Exon (1976) observed that five fluvial cycles characterise the Jurassic and lowest stage of the Cretaceous (Table 2). These upward fining cycles are typified by coarse freshwater quartzose sandstones, grading to finer sandstones, siltstones and mudstones. The sandstone units form important aquifers (Exon, 1976). Coal and volcanogenic sediments further distinguish individual units. Coal deposits characterise the Mid-Jurassic Walloon Coal Measures and are found in the Late Jurassic Orallo Formation. Labile sands deposited during the Mid to Late Jurassic cycles reflect contemporaneous volcanism (Exon, 1976; Exon and Senior, 1976). These volcanic deposits reach an average thickness of 500 m (Exon and Senior, 1976). Depositional environments include the higher energy braided and meandering rivers, and the lower energy lakes, swamps and deltas.

Marine conditions encroached on the basin in the Early Cretaceous (Table 2). However environments cycled between marine and freshwater, with the stratigraphic record revealing a regression in the early Albian (Coreena Member), followed by a second transgression (Surat Siltstone). The youngest unit of the Surat Basin (Griman Creek Formation) was deposited in paralic conditions during the Albian and marks the ultimate retreat of marine conditions. Sedimentation rates were higher during this Cretaceous phase of marine transgression and regression at 15 cm per 1000 yrs, compared to 4 cm per 1000 yrs during the preceding Jurassic freshwater cycles (Exon, 1976). Exon (1976) suggests that this increase was due to an influx of volcanic detritus and eroded coastal sediments. See Table 2 for a summary of the generalised stratigraphy of the basin.

Table 2. Generalised stratigraphy of the Surat Basin (adapted from Exon, 1976; Exon and Senior, 1976).

Period	Stage/Epoch	Unit	Maximum Thickness (m)	Environment of Deposition and Lithology	Fluvial Cycle	Freshwater vs. Marine
Cretaceous	Albian	Griman Creek Formation	480	*Paralic and Freshwater*: Sandstone, siltstone, mudstone		Final Marine Retreat
		Surat Siltstone	150	*Marine*: Siltstone, mudstone, sandstone		Transgression
		Coreena Member (Wallumbilla Formation)	210	*Freshwater*: Siltstone, mudstone, sandstone		Partial Regression
	L. Aptian	Doncaster Mudstone (Wallumbilla Formation)	270	*Marine*: Mudstone, some siltstone		Marine Transgression
	Neocomian to E. Aptian	Bungil Formation	270	*Freshwater and Paralic*: Mudstone, siltstone, sandstone	5	
	Neocomian	Mooga Sandstone	300	*Freshwater*: Sandstone, some siltstone and mudstone		
Jurassic	L. Jurassic	Orallo Formation	270	*Freshwater*: Labile sandstone, siltstone, mudstone, coal	4	Freshwater
		Gubberamunda Sandstone	300	*Freshwater*: Sandstone, some siltstone and conglomerate		
		Westbourne Formation	200	*Freshwater and Paralic(?)*: Siltstone, mudstone, sandstone	3	
	M.–L. Jurassic	Springbok Sandstone	250	*Freshwater*: Labile sandstone, siltstone, mudstone		
	M. Jurassic	Walloon Coal Measures	650	*Coal Measures*: Labile sandstone, siltstone, mudstone, coal	2	
		Eurombah Formation	100	*Freshwater*: sandstone, some conglomerate, siltstone and mudstone		
	E. Jurassic	Hutton Sandstone	250	*Freshwater*: Sandstone, some siltstone and mudstone		
		Evergreen Formation	260	*Freshwater and Paralic*: Siltstone, mudstone, sandstone	1	
		Precipice Sandstone	150	*Freshwater*: Quartzose sandstone, some siltstone and mudstone		
Unconformity (L. Triassic Erosion)						

3.4.3 Basin Evolution

Subduction of the palaeo-Pacific beneath eastern Gondwanaland during the Mesozoic provided the back-arc setting in which these basins formed. Following a ~30 Myr period of erosion that ended the Triassic in eastern Australia (Senior et al., 1978; Gallagher, 1990), subsidence of the extensive peneplain created accommodation space (Waschbusch et al., 2009), on to which sediments of the Eromanga and Surat basins were deposited over an interval of ~100 Myr.

Basin formation can be attributed to several mechanisms. These mechanisms may all contribute to the evolution of a basin, and can occur concurrently in various permutations. Lithospheric stretching and thermal cooling induce the isostatic response of subsidence; flexure of the crust due to an external force, such as loading, can deflect the earths surface if the flexural rigidity of the crust is overcome; descending viscous mantle flow related to subduction can transiently draw down overlying crust (Mitrovica et al., 1989). Different subsidence mechanisms have contributed to the subsidence histories of the Eromanga and Surat basins.

Gallagher and Lambeck (1989) found that the Eromanga Basin subsided 5 to 10 times faster in the Cretaceous compared to the Jurassic. Tectonic subsidence curves for this time no longer conform to the previous linear to pseudo-exponential trend that characterised the Jurassic. Geodynamic modelling, apatite fission track analysis and backstripping to compute tectonic subsidence have all provided evidence in favour of a model of dynamic subsidence related to subduction (e.g. Veevers, 1984; Gallagher et al., 1994; Russell and Gurnis, 1994; Waschbusch et al., 2009) based on the principles outlined by Mitrovica et al. (1989).

During the Jurassic, subsidence rates were higher in the Surat Basin, with sediment thicknesses of 500-900 m recorded for the Eromanga Basin compared to 1500 m for the Surat Basin (Gallagher et al., 1994). A decrease in sediment thickness east of the Surat Basin, in the Clarence-Moreton Basin, led Gallagher et al. (1994) to consider the Surat Basin as a depocentre at this time. Subsidence rates increased in the Early Cretaceous in both basins, however a more incomplete sediment record for the Surat basin makes it difficult to determine if the Surat Basin continued to subside more rapidly.

Subsidence ended ~100Ma and was replaced by a phase of uplift (e.g. Veevers, 1984; Gallagher et al., 1994; Raza et al., 2009). As a result, the Eromanga and Surat basins were subjected to basin inversion and extensive erosion (Gallagher et al., 1994; Raza et al., 2009). Apatite fission track-analysis has revealed ~1.9 km of denudation in the Surat Basin (Raza et al., 2009) and up to ~1 km in the Eromanga Basin (Gallagher et al., 1994). Preservation of the Mesozoic sediment record is more temporally extensive for the Eromanga Basin. The youngest sediments in the Eromanga Basin date to 90 Ma (Gallagher et al., 1994), compared to Aptian/Albian (~99 Ma) for the Surat Basin (Raza et al., 2009). An absence of Cretaceous aged sediment in the Clarence-Moreton Basin continues this easterly increasing trend of stratigraphy truncation.

The Ceduna Depocentre, a structural unit of the Bight Basin in the Great Australian Bight, was a major sink for sediments eroded from the uplifted eastern Australian basins (Veevers, 1982; Veevers, 1984; Krassay and Totterdell, 2003). An extensive south-westerly draining river system, precursory to the present day Murray-Darling drainage system, transported sediments from the uplifted northeastern margin (Veevers, 1984). Jurassic to Late Cretaceous aged sediments form a number of supersequences that reach a maximum thickness greater than 15 km. The Late Cretaceous Hammerhead Delta delivered post uplift sediments to the shelf where they form the Hammerhead Supersequence (Krassay and Totterdell, 2003).

Uplift of the Eromanga and Surat basins is directly related to subduction ending. More specifically it has been attributed to the reversal of dynamic topography, and the significant change to the predominant tectonic regime that paralleled eastern Gondwanaland from convergence to extension (e.g. Gallagher et al., 1994; Russell and Gurnis, 1994; Raza et al., 2009). As the supply of descending slab material was no longer being replenished by subduction, the Australian plate tilted upwards again. Russell and Gurnis (1994) propose that uplift of 500 m extended up to 1000 km inland of the eastern margin. Northerly remnants of the Surat Basin have even been completely removed by erosion (Raza et al., 2009), attesting to the notion that a stratigraphic unconformity is the final vestige of dynamic topography (Burgess et al., 1997).

A contractional event during the Cenomanian (~95-90 Ma) further facilitated uplift along the eastern margin (Korsch et al., 2009). Korsch et al. (2009) inferred from seismic profiles of the Surat Basin that pre-existing faults in the underlying Bowen Basin were

reactivated, accommodating several hundred metres of uplift. For example, ~720 m of Surat Basin sediments were uplifted to the east of the Tingan Fault which trends N-S along the eastern boundary of the Bowen-Gunnedah Basin between ~28-28.5°S.

4 Methodology

4.1 Overview

In order to investigate the surface evolution of Australia since 140 Ma, and subsequently contrain the plate boundary configuration east of Eastern Gondwanaland during the Cretaceous, output from a series of geodynamic models was compared to two geological data sets. Geodynamic models allow us to simulate mantle evolution and surface vertical motions over millions of years. A tectonic subsidence analysis of borehole data, acquired along an E-W transect through the Eromanga and Surat basins, provided observational data with which to compare the tectonic subsidence predicted by the geodynamic models. Comparisons between seismic tomography data and the modelled present-day temperature structure of the mantle put further constraints on the models. In essence the latter two methods were used to validate the geodynamic models. Figure 9 summarises this three-tiered workflow.

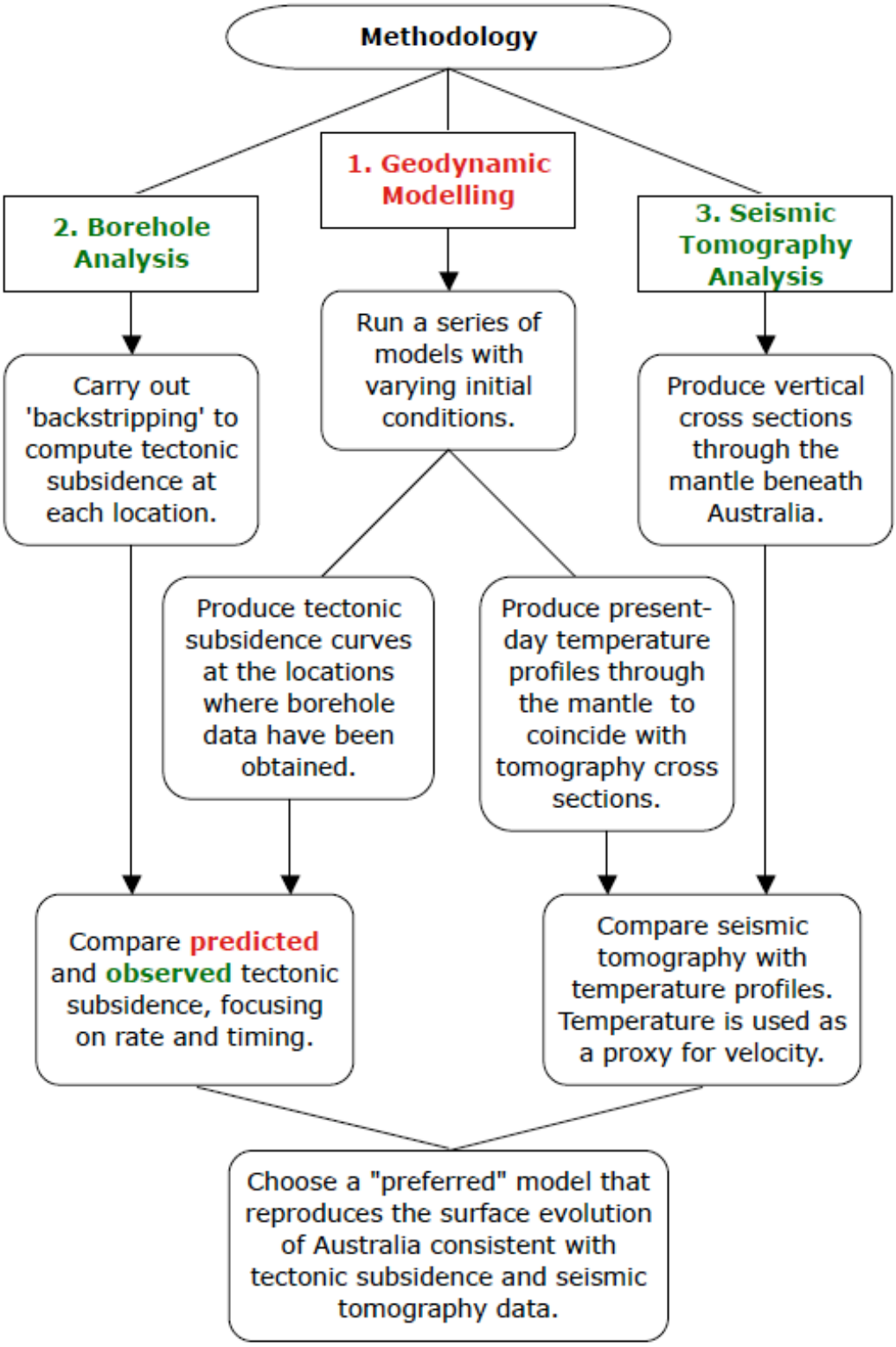

Figure 9. Flowchart illustrating the three-tiered approach to constraining the plate boundary configuration east of Australia during the Cretaceous. Geodynamic modelling is complemented by two methods to validate the findings.

4.2 Geodynamic Modelling

Geodynamic models can be used to simulate material deformation resulting from the interactions between the crust and mantle processes. Until geodynamic modelling advances to the stage of complete self-consistency, complex hybrid models assimilate kinematic data describing plate motions to allow for site and time specific investigation. By comparing output to geological observations, models can be assessed for their effectiveness in predicting mantle structure and surface vertical motions due to time-dependent mantle flow and plate motions.

The models utilised here fall in the class of 'Forward' models. Essentially they run forward in time from a given starting age, for a specified period of time. A set of starting conditions must be defined to initially govern the solving of the model. These initial conditions require reasonable assumptions to be made about the structure and rheology of the mantle and crust.

4.3 CitcomS

Our geodynamic models use the Computational Infrastructure for Geodynamics' (CIG) finite element code *CitcomS* (Zhong et al., 2000; McNamara et al., 2004; Tan et al., 2006). *CitcomS* enables geodynamic modelling within a partial (CitcomSRegional) or full (CitcomSFull) spherical domain by solving for thermo-chemical convection. Given an initial temperature, viscosity and density field, the finite element method (Hughes, 1987) is used to solve the governing equations: conservation of mass, conservation of momentum and conservation of energy. The "working variables", pressure and velocity, are iteratively calculated to convergence at each timestep, with the results used to compute values for the next timestep. Velocities are used to solve the diffusion-advection equation, which updates the temperature field.

The geodynamic models were designed to investigate dynamic topography of the eastern Australian region, specifically within the Eromanga and Surat basins during the Cretaceous, and ultimately constrain the location of the subduction zone that spanned the eastern margin of Eastern Gondwanaland at this time. This required the manipulation of initial and boundary conditions to improve the model's capacity to replicate the timing and magnitude of subsidence in the identified basins, as inferred from borehole data. The

workflow for producing and executing these models was adapted from that of DiCaprio (2009).

4.3.1 Model Specifications and Setup

The *CitcomS* models are 'coupled', consisting of a high-resolution regional model embedded in a lower-resolution global model (Figure 10 and Table 3). This integration was achieved using coupled *CitcomS* solvers (Tan et al., 2006). The regional model incorporates the Australian Plate, whereby producing high-resolution data for the area of investigation. As the regional model is embedded in the global model, the temperature and velocity fields are continuous at the regional-global model boundary. This allows temperature and velocity feedback between the two models. The global model essentially provides the side and bottom boundary conditions for the regional model.

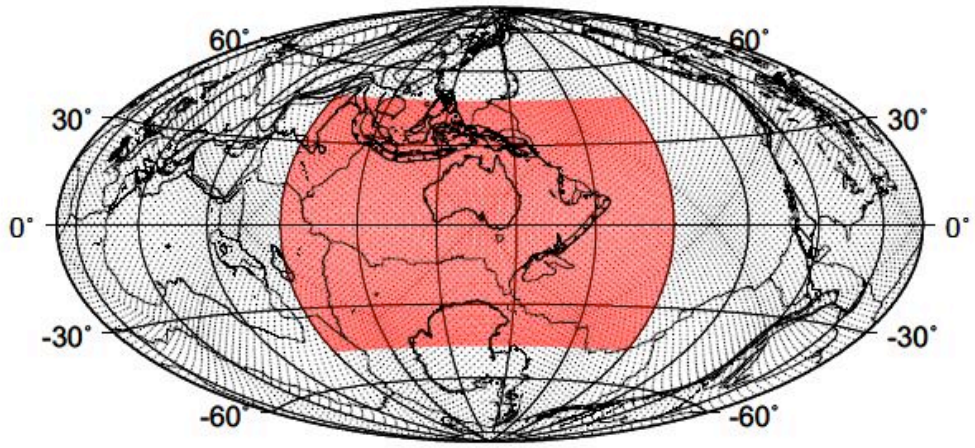

Figure 10. Global map highlighting the location of the regional modelling domain (red) within the containing global domain (from DiCaprio, 2009). Note that a rotated reference frame is used to avoid regional mesh compression at the poles, as discussed below.

The global mesh is divided into 12 'caps' (faint diamond outlines seen in Figure 10), each extending to the core-mantle boundary. The regional mesh is bounded by constant latitude (47.5ºN and 47.5ºS) and longitude (60º and 210º), and extends to a depth of ~2230 km. Eulerian meshes are used, with regular geometries. The mesh geometries and surface resolutions are listed in Table 3.

Table 3. Resolution of geodynamic models.

Model	Number of Nodes			Surface Resolution
	Latitude Direction	Longitude Direction	Z (Radial) Direction	
Global (per cap)	33	33	33	~200 km
Regional	257	257	65	~64 km (Long.) x ~40 km (Lat.)

All geographical data are rotated 37.5º northward to the equator (rotation pole, 225º/0º) prior to executing the model (Figure 10). This is required because during the Mesozoic Australia was located at high latitudes. The rotated reference frame avoids regional mesh compression caused by the extremely reduced longitudinal distances near the poles.

Model parameters that were kept constant between the simulations are listed in Table 4. When visualising CicomS model outputs, depth is non-dimensionalised with 0 as the centre of the earth and a value of 1 being equal to 6371km (the radius of the Earth) (from Table 4 below). Temperature is also non-dimensionalised ranging from 0-1, with a value of 1 being equal to 1500ºC, that is, the temperature difference between the core-mantle boundary and the surface (see Table 4 below).

Table 4. Variables held constant between model runs.

Variable	Notation	Value
Reference mantle density	ρ_0	3500 kg/m^3
Gravity	g	10 m/s^2
Surface temperature	T_0	0ºC
Temperature difference between CMB and the surface	ΔT	1500ºC
Radius	R_0	6371 km
Coefficient of thermal expansion	α	2x10^{-5} K^{-1}
Thermal diffusivity	κ	1x10^{-6} m^2/s
Reference viscosity	η_0	2x10^{21} Pas

4.3.2 Radial Mantle Structure

The global and regional mantle domains are radially divided into four layers, with varying temperature-dependent viscosities (Figure 11):

$$\eta = \eta_0 \times \exp\left(\frac{E_\eta}{T + T_\eta} - \frac{E_\eta}{1 + T_\eta}\right), \qquad (1)$$

where η_0 is the reference viscosity, T is temperature, η_E is a non-dimensional activation energy, η_T is the viscosity change due to the temperature offset in each layer. A lithosphere (0-100 km) is implemented with a high-viscosity to simulate mechanical rigidity. The remaining mantle is divided in to the upper mantle (100-410 km), a transition zone (410-660 km) and the lower mantle (660-2870 km). These boundaries also reflect distinct density differences within the mantle, measured as seismic discontinuities. At 410 km and 660 km depth, phase transitions of olivine and its heavier polymorphs (olivine to spinel, and spinel to post-spinel perovskite and magnesiowüstite), incur density jumps of ~100 kg/m^3 (Bina and Helffrich, 1994) and 236 kg/m^3 (Ita and Stixrude, 1992), respectively.

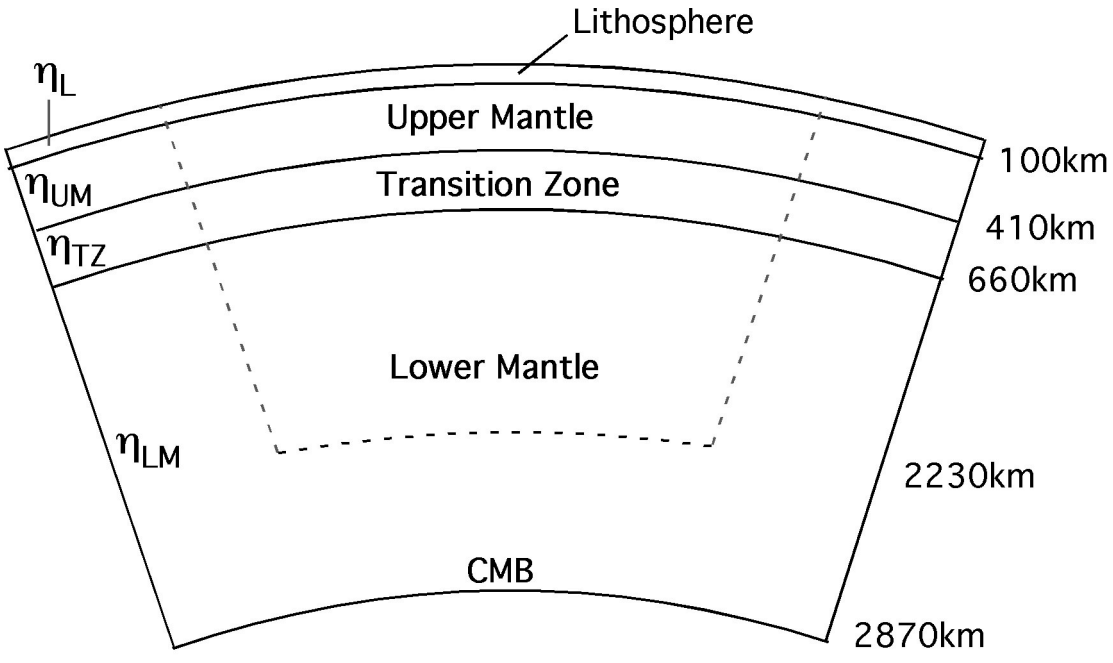

Figure 11. Schematic illustrating the division of the modelling domains into 4 layers; Lithosphere (0-100 km), Upper Mantle (100-410 km), Transition Zone (410-660 km) and Lower Mantle 660- 2870 km). Dashed lines define the regional embedded model. η_L – lower mantle viscosity, η_{UM} – upper mantle viscosity, η_{TZ} – transition zone viscosity and η_{LM} – lower mantle viscosity; values vary between models (see equation (1)). CMB – core-mantle boundary. (Not to scale)

4.3.2.1 Transition Zone Phase Boundaries

As a result of temperature differences between a cold descending slab and the hot ambient mantle, the 410 km and 660 km phase boundaries can become distorted. This results in the 410 km boundary becoming elevated across a slab, while the 660 km boundary is depressed (Figure 12). These differences are due to the temperature-pressure relationships of the phase changes (represented by their Clapeyron curves), and have implications for the descent of the slab.

A Clapeyron curve defines the temperatures and pressures at which two phases of the same mineral are in equilibrium. At 410 km the Clapeyron slope is positive, therefore the lower temperatures of the descending slab induce the phase change to occur earlier. The dense spinel polymorph, now at shallower depths, drags the slab down, providing an additional driving force to the descent of the slab. Contribution of the 410 km phase boundary is on the order of $\sim 1.6 \times 10^{13}$ Nm^{-1} (for a Clapeyron slope of 4.0 MPa/K), or around half that of the body force due to thermal contraction (the driving force due to the temperature contrast between the slab and the mantle) (Turcotte and Schubert, 2002). Contrasting effects of the 660 km phase boundary relate to the negative slope of the Clapeyron curve. As the phase change occurs at increased depths, due to the lower temperatures in the slab, the spinel structure persists for longer. The relative buoyancy of the spinal mineral impedes descent of the slab.

Clapeyron slopes for the 410 km and 660 km phase transitions were incorporated into the *CitcomS* models. Values of 4.0 MPa/K and -2.0 MPa/K were assigned to the 410 km and 660 km boundaries, respectively. These slopes are consistent with recent in situ X-ray diffraction studies (Morishima et al., 1994; Katsura et al., 2003; Katsura et al., 2004).

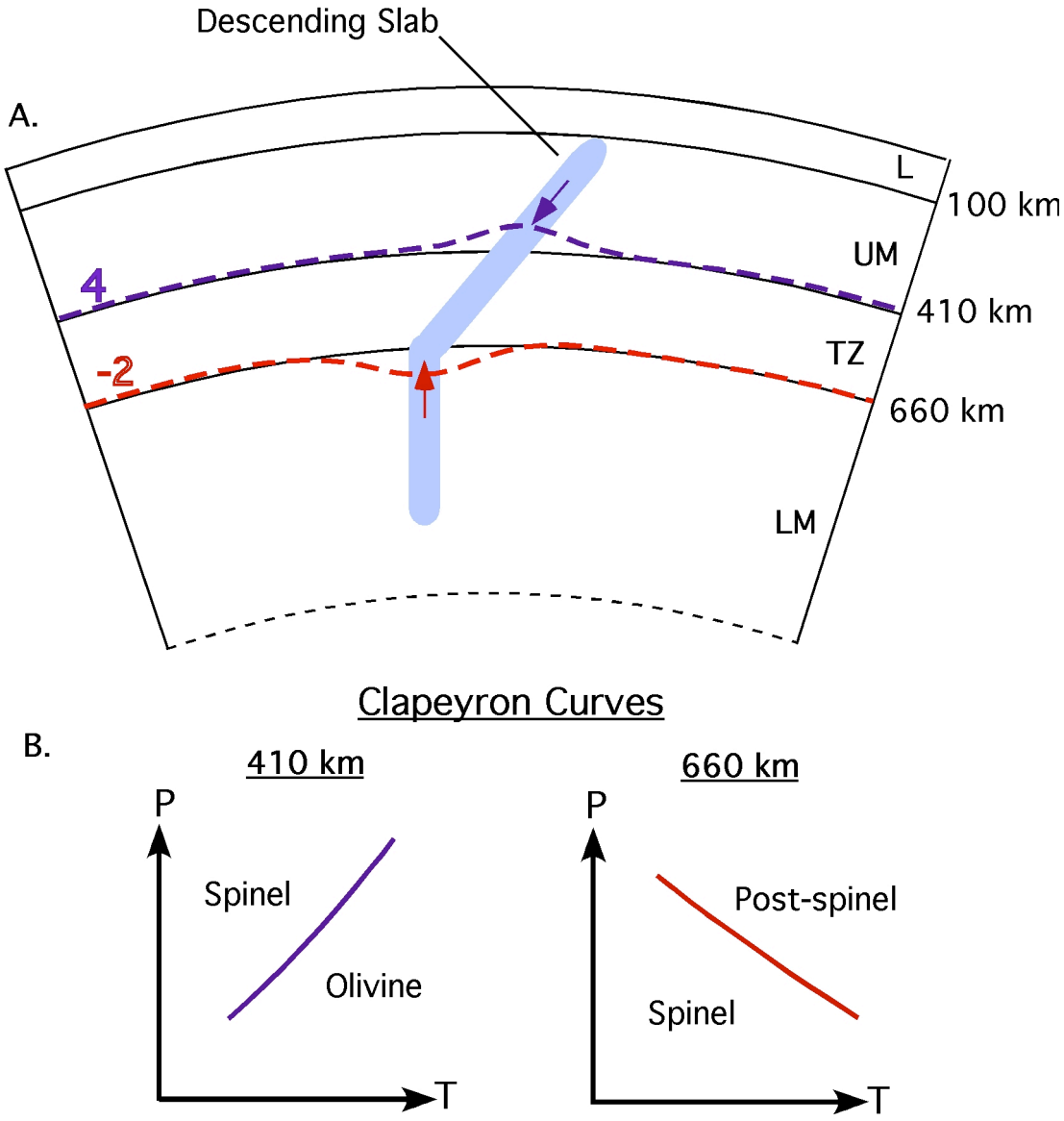

Figure 12. (A) Schematic of the upper half of the mantle with a subducted slab inserted (blue). The slab has been detached from the surface for simplification. The 410 km phase transition (purple dashed line) is deflected upwards in the vicinity of the slab, representing the influence of a positive Clapeyron slope inducing the phase change of olivine to spinel to occur earlier in the presence of colder temperatures. The reverse is true for the 660 km phase transition (red dashed line), where a negative Clapeyron slope delays the transition of spinel to post-spinel minerals. Coloured arrows reflect the influence of the phase transitions on the descent of the slab; at 410 km descent is facilitated, at 660 km it is hindered. Coloured numbers to the left indicate the values given to the Clapeyron slopes in the *CitcomS* models. (B) Simple graphs showing the pressure temperature relationships of the 410 km and 660 km phase transitions. At 410 km the slope of the Clapeyron curve is positive and at 660 km the slope is negative. P – pressure, T – temperature. (Not to scale)

4.3.3 Input Files

The *CitcomS* models require a series of input files describing the rheology of the mantle and crust, plate motions since 140 Ma and evolving plate boundaries. The initial conditions are implemented for the solving of the first timestep and are subsequently modified as the model advances. The boundary conditions are active for the duration of the model. They constrain the surface evolution of the model to be consistent with plate motions and plate boundary configurations since 140 Ma. See Table 5 below for a list of the different input files assimilated into the geodynamic models.

Table 5. Description of input files assimilated into *CitcomS* models.

Input File	Description	Model	Initial or Boundary Condition
Temperature	Describes temperature field with depth.	Global and Regional	Initial Condition
Tracer	Controls continental buoyancy and mantle wedge viscosity.	Regional	Initial Condition
Velocity	Dictates plate motions and boundaries.	Global and Regional	Boundary Condition
Lithospheric Age	Used to generate surface temperatures.	Global and Regional	Boundary Condition
Back-arc Basin (Temperature and Velocity)	Forces slab down in to the mantle to ensure it does not surface.	Regional	Boundary Condition

4.3.3.1 Initial Conditions

- **Temperature**

A slab is represented by a perturbation in the temperature field. Constructing an initial mantle temperature field is therefore required to introduce a slab into the model and specify its location and dip. Temperature values are non-dimensionalised, and range from 0 to 1. Mantle material is prescribed the maximum temperature of 1, whilst temperature of the slab increases to 1, symmetrically from a minimum value in the centre (~0.5). A half-space cooling model, based on the age of oceanic crust at the trench, was used to define

this temperature gradient in the slab (DiCaprio, 2009). The dip of the slab was kept fixed at 50º to a depth of 660 km, before vertically penetrating the lower mantle.

- **Tracers**

Active tracers were inserted into the regional mesh to provide continental buoyancy and reduce the viscosity of the mantle wedge. Due to compositional differences, continental crust is less dense than underlying continental lithosphere and mantle, and therefore more buoyant. The increase of continental buoyancy in the model therefore reflects these density differences that exist between difference layers in the earth. This buoyancy contrast also stabilised the layer, increasing its resistance to any negative buoyancy influences invoked by underlying material (DiCaprio, 2009).

During subduction, slab dehydration resulting from diagenesis and metamorphism, releases fluids into the mantle wedge, the region directly above the slab beneath the over riding plate (Tatsumi et al., 1983; Peacock, 1990; Ranero et al., 2003). This process reduces the viscosity of the wedge (e.g. Billen and Gurnis, 2001). A low viscosity mantle wedge can have important implications for the evolution of a subducting slab, for example influencing slab dip (Manea and Gurnis, 2007) and surface topography of the overlying crust by reducing the magnitude of observed dynamic topography (Billen and Gurnis, 2001; Billen et al., 2003). Tracers in the region of the mantle wedge reduced viscosity by 10% compared to the surrounding mantle material; consistent with the minimum decrease in mantle wedge viscosity suggested by the geodynamic modelling of Billen and Gurnis (2001).

4.3.3.2 Boundary Conditions

- **Lithospheric Ages**

Surface temperatures were computed from lithospheric ages of the ocean floor (Müller et al., 2008b) every 1 Myr as a boundary condition for the model. The half-space cooling equation (1) was used to derive a temperature from the lithospheric ages:

$$T^{HS} = T_S + (T_m - T_S) erf\left(\frac{z}{2\sqrt{kt}}\right), \qquad (2)$$

where T^{HS} is the half-space temperature, T_s is the surface temperature (non-dimensionalised), T_m is the mantle temperature, t is time and z is depth.
These surface temperatures were then linearly extrapolated to a depth of 80 km (2):

$$T_{i+1} = aT_i + (1-a)T_{i+1}^{HS} \text{ where } a = \begin{cases} \dfrac{y}{y_p} & y < y_p \\ 1 & y \geq y_p \end{cases}, \qquad (3)$$

where T_i is temperature at timestep i, T_{i+1}^{HS} is the temperature derived from the half-space cooling equation at the given timestep ($i+1$), y is depth and y_p is the end depth of 80 km.

- **Velocities**

The assimilation of plate velocity data from 140 Ma governed the model surface kinematics and plate boundary configurations in the regional and global meshes. These surface velocities were imposed in the latitude- and longitude-directions, with velocities in the z-direction set to zero. Plate boundary geometries refer to locations and types of plate boundaries, for example spreading ridges and subduction zones. These velocity data were acquired using the plate reconstruction software *GPlates* (Boyden et al., 2009). *GPlates* allows for the high-resolution time-dependent evolution of plate polygons (Gurnis et al., 2009-submitted) to define regions of differing velocities, as well as the generation of new plate boundaries. This latter function was essential for experimenting with different subduction zone locations during the Cretaceous. Plate polygons were updated at 1 Myr intervals, with velocities linearly interpolated at intervening times.

In order to reconstruct plates and generate plate velocities, *GPlates* requires plate rotation data; these data specify an Euler rotation pole, and the direction and magnitude of motion. The rotation data used to generate plate velocities for the *CitcomS* models were based on several different reference frames (Table 6).

Table 6. Reference frames used to reconstruct plates in *GPlates*.

Plates	Time Interval	Reference Frame	Reference
Pacific Plates	0 – 83.5 Ma	Moving hotspot reference frame	O'Neill et al. (2005)
	>83.5 Ma	Pacific hotspot reference frame	Wessel et al. (2006)
All Other Plates	0 – 100 Ma	Moving hotspot reference frame	O'Neill et al. (2005)
	>100 Ma	Fixed hotspot reference frame	Müller et al. (2008a)

- **Back-arc Basin**

Viscous flow in oceanic- and arc-corners at subduction zones, induced by plate motions, produce dynamic pressure forces along the lower and upper slab surfaces, respectively (e.g. Stevenson and Turner, 1977; Tovish et al., 1978). These pressure forces act perpendicular to the descending slab, and result in compression (positive pressure) or suction (negative pressure). If not counterbalanced by opposing torque forces (e.g. gravitational torque), dynamic pressure forces rotate (torque) the slab about its hinge axis, towards or away from the overriding plate. Net negative pressure acting on the upper surface of the slab causes the slab to be uplifted beneath the overriding plate. This phenomenon reduces dip angle and can ultimately result in flat slab subduction (Tovish et al., 1978).

Continuum modelling produces strong coupling between the lithosphere and mantle, potentially compounding the 'uplifting' effects of slab suction. Methods to remove the unwanted modelling effects of slab suction and force the slab into the upper mantle, include removing the region of the overriding plate adjacent to the trench (Christensen, 1996; Davies, 1999; Tan et al., 2002) and imposing a trench perpendicular velocity opposite to that of the converging plate (Christensen, 1996; Tan et al., 2002). Including a low-viscosity wedge may also reduce the influence of slab suction (Manea and Gurnis, 2007). Following Christensen (1996) and Tan et al. (2002), a back-arc region was defined with mantle temperature (essentially removing the plate) and trench perpendicular velocity, of a similar yet opposite magnitude to that of the oceanic plate.

4.3.4 Models

Mantle material properties and initial plate boundary configurations were varied in a series of model runs. An initial mantle material parameter analysis tested the influence of upper and lower mantle viscosities, convective vigour (Rayleigh number) and the temperature contrast between the slab and the mantle on dynamic topography in the Eromanga and Surat basins (Table 7). To constrain the location of the subduction zone during the Cretaceous, two end-member scenarios were tested; one with subduction adjacent to the reconstructed eastern continental margin, and a second with subduction translated 23º further east (Table 8) (Figure 13).

Our 'Reference Model' (RM) (Table 7), was chosen from a series of model runs from DiCaprio (2009) (Model 'M140_1', p.90). The radial viscosities and Clapeyron slope values in model RM match those in the preferred model (M2) of DiCaprio et al. (In Press) for predicting Late Miocene Subsidence of the Marion Plateau consistent with borehole tectonic subsidence data.

Table 7. Initial model runs with subduction adjacent to reconstructed continental margin.

Model Name	Rayleigh Number	Radial Viscosities ($\eta_L, \eta_{UM}, \eta_{TZ}, \eta_{LM}$)	Initial Temp. Contrast	Slab Depth (km)
RM*	1.3576×10^8	100, 1, 5 50	0.5	~2000
RM_1	1.3576×10^8	100, **0.5**, 5 50	0.5	~2000
RM_2	1.3576×10^8	100, **0.25**, 5 50	0.5	~2000
RM_3	1.3576×10^8	100, 1, 5, **250**	0.5	~2000
RM_4	**2.7146×10^8**	100, 1, 5 50	0.5	~2000
RM_5	**6.788×10^7**	100, 1, 5 50	0.5	~2000
RM_6	1.3576×10^8	100, 1, 5 50	0.25	~2000

*'Reference Model'

Table 8. Second set of model runs with subduction translated 23º east of reconstructed continental margin.

Model Name	Rayleigh Number	Radial Viscosities ($\eta_L, \eta_{UM}, \eta_{TZ}, \eta_{LM}$)	Initial Temp. Contrast	Slab Depth
Slab23E_RM	1.3576×10^8	100, 1, 5, 50	0.5	CMB*
Slab23E_1	1.3576×10^8	100, **2**, **10**, **100**	0.5	CMB*
Slab23E_2	1.3576×10^8	100, 1, **30**, **100**	0.5	CMB*
Slab23E_3	1.3576×10^8	100, **2**, **50**, **100**	0.5	CMB*

* Slab depth was extended to the core-mantle boundary (CMB) in the later series of model runs to reflect long-lived subduction between Eastern Gondwanaland and the palaeo-Pacific.

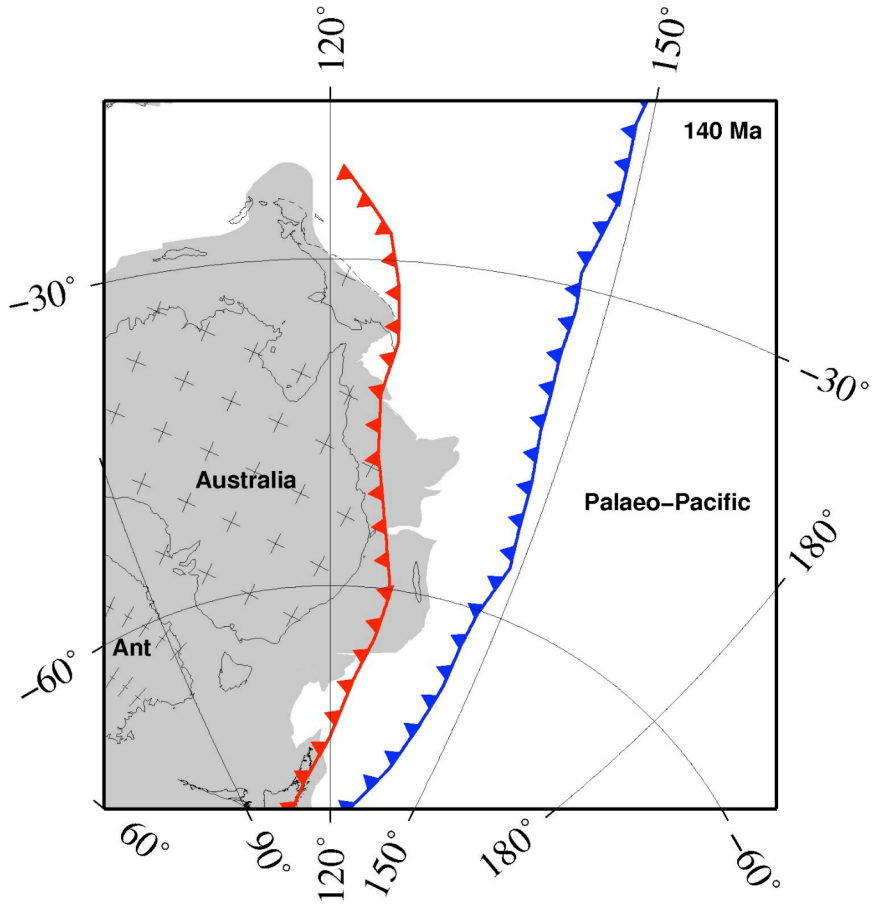

Figure 13. Tectonic reconstruction of Australia at 140 Ma. The location of the subduction zone used in the 'RM' model series (see text above) is coloured red and the location of the subduction zone shifted 23º east (from the 'Slab23E' model series) is coloured blue. Triangles point in the direction of the overriding plate. Ant – Antarctica. Grey shading represents the extent of present-day continental crust and has been included as a guide only.

4.3.5 Model Execution

All models were run on California Institute of Technology's High Performance Computing Cluster, in the Division of Geological and Planetary Sciences. Models are run in parallel and are designated 140 processors, 12 for the containing model and 128 for the embedded model. Each simulation took on average 2.5 days to solve and a further 0.5 days to post-process the output. This highlights that access to high-performance computing was an essential component of this project, which could not have been completed in the necessary timeframe otherwise.

Note: Using only 1 processor, each model would have taken ~1 yr to solve.

4.3.6 Extracting Modelled Dynamic Topography

CitcomS models a vertically "fixed surface", that is, while velocities are imposed in the latitude- and longitude-directions, velocity in the z-direction is set to zero. Hence, a second regional *CitcomS* model (with the same dimensions) with 'natural boundary conditions' is required to compute surface dynamic topography in the Australian region. Natural boundary conditions at the free surface, that is stress=0, enables displacements (velocities) to develop in the z-direction (vertical).

Mantle velocities (>200 km depth) at each timestep were fed in to this second regional model; velocities in the upper 200 km were ignored so as to ensure that the calculations reflected mantle signals rather than imposed plate velocities (Figure 14). Temperature was also set to ambient mantle temperature in this region for simplification. The model was then run for one timestep in order to calculate the effect of the imposed mantle velocity field on surface nodes. Dynamic topography was outputted as a non-dimensionalised displacement (u_i), representing the change in vertical displacement over that single timestep, which was then multiplied by a coefficient (c) to dimensionalise the dynamic topography (h):

$$h = u_i c \text{; where } c = \left[\left(\frac{1}{(\rho_0 - \rho_w) g} \right) \left(\frac{\eta_0 \times k}{R_0^{\,2}} \right) \right]^{-1}, \qquad (4)$$

where is ρ_0 the reference mantle density, ρ_w is density of water, g is gravity, η_0 is viscosity, k is thermal diffusivity and R_0 is the radius of the earth (Table 4).

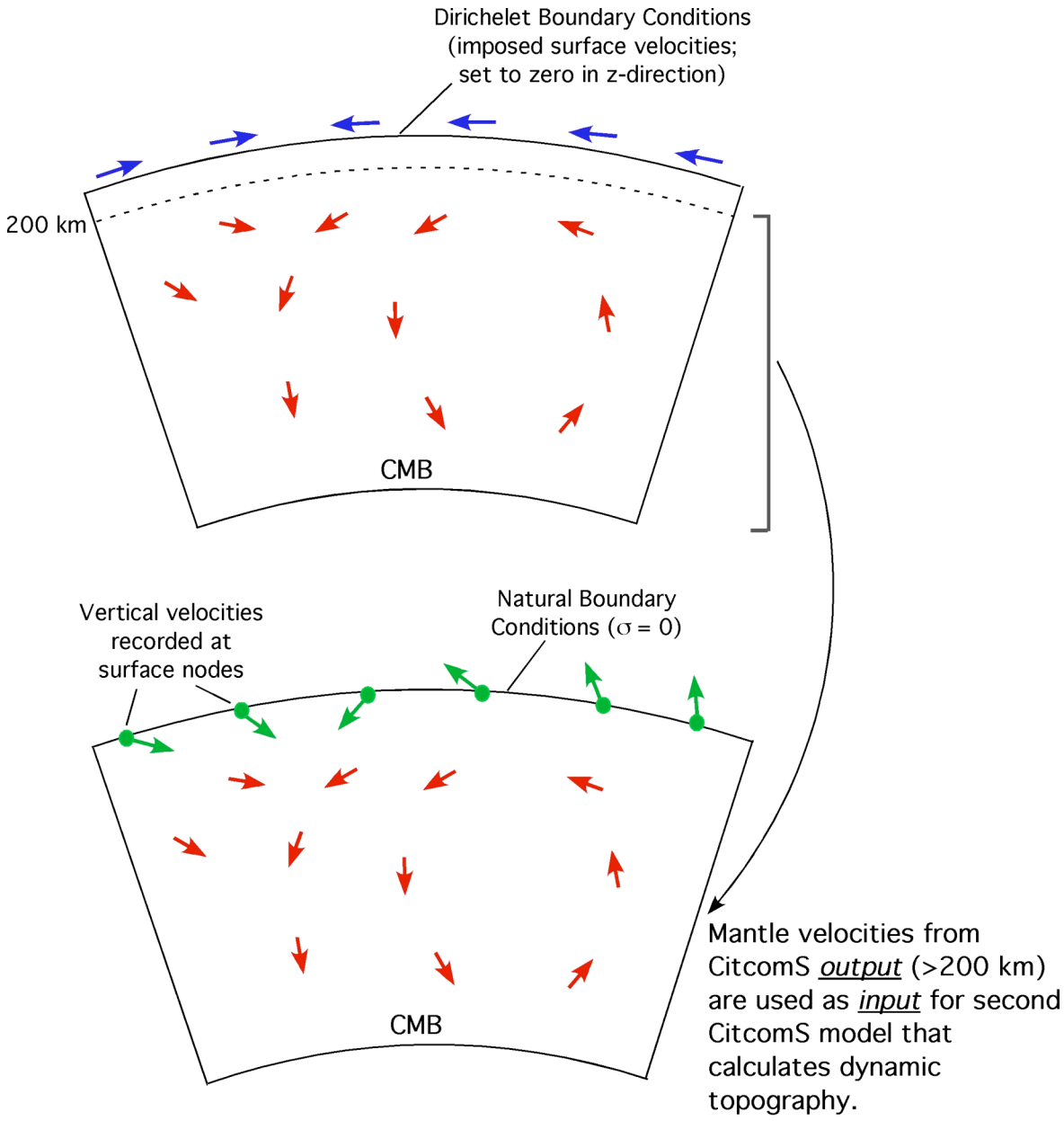

Figure 14. Schematic representing how mantle velocities are taken from *CitcomS* output (top image) and inserted into a second *CitcomS* model (bottom image) in order to derive values for dynamic topography. Blue arrows represent lateral surface velocities, red arrows represent mantle velocities and green arrows represent surface velocities in the z-direction. Green spots represent surface nodes where displacements are computed.

4.4 Borehole Analysis

Gallagher (1990) calculated the subsidence histories at 44 borehole locations along the Eromanga-Brisbane Geoscience Transect (Figures 15-16). This allowed him to quantify the subsidence trends of Permian to Triassic, and Jurassic to Cretaceous aged basins, in eastern Australia. The stratigraphic data for these boreholes were acquired and the 42 boreholes from the Eromanga and Surat basins were reanalysed.

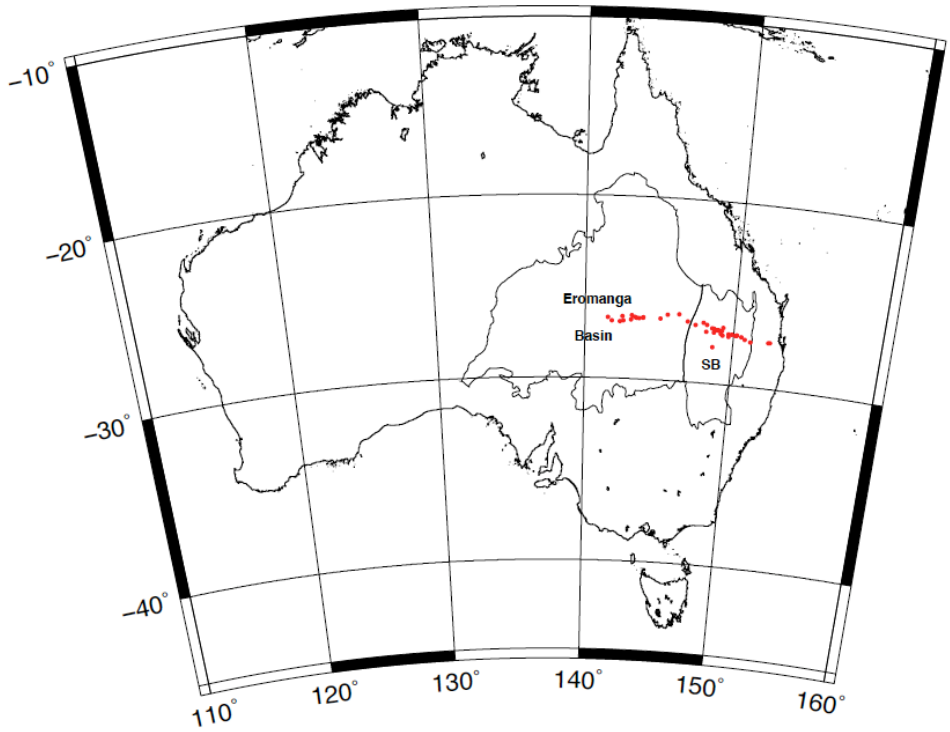

Figure 15. Map of Australia showing the outlines of the Eromanga and Surat basins (SB – Surat Basin) and locations of boreholes used to calculate tectonic subsidence (red dots). See Figure 16 for a zoomed-in view of the region.

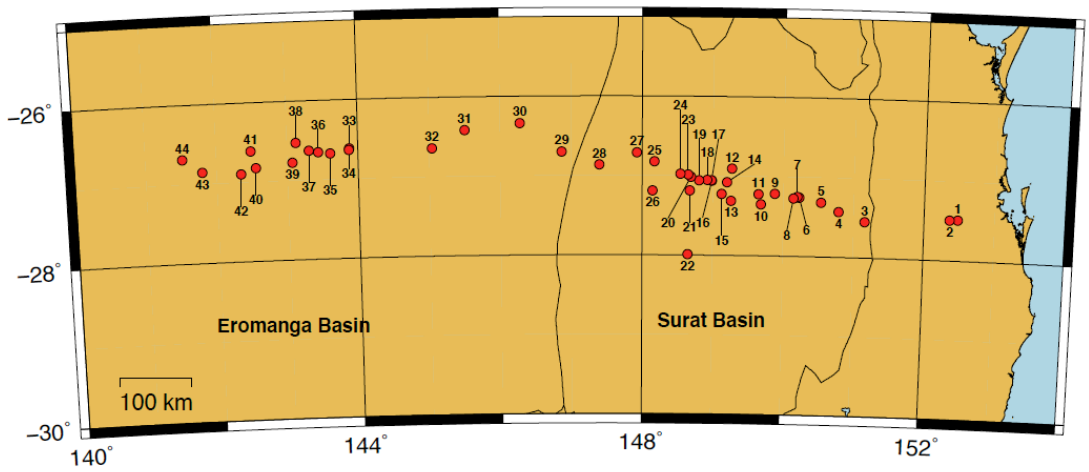

Figure 16. Zoomed-in view of borehole locations. 1 - Lockrose 1; 2 - Baylem 1; 3 - Cecil Plains West 1; 4 - Kumbarilla 1; 5 - Alick Creek 1; 6 - Lorraine 1; 7 - Leichhardt 1; 8 - Arlington 1; 9 - Meandarra 1; 10 - Paloma 1; 11 - Coalbah 1; 12 - Apple Tree 1; 13 - Red Cap 1; 14 - Myall Creek 1; 15 - Grantham 1; 16 - Newington 1; 17 - Newington 2; 18 - Taralga 1; 19 - Kincora 1; 20 - Narelle 1; 21 - Basketyard Creek 1; 22 - Bainbilla 1; 23 - Avondale South 1; 24 - Tory Boy 2; 25 - Glenroy 1; 26 - Hoolah 1; 27 - Strathmore 1; 28 - Scalby 1; 29 - Lowood 1; 30 - Charleville 1; 31 - Quilberry 1; 32 - Quilpie 1; 33 - GSQ Eromanga 1; 34 - Mongarlo 1; 35 - Eromanga 1; 36 - Kenmore 1; 37 - Black Stump 1; 38 - Mount Bellalie 1; 39 - Berellem 1; 40 - Boldrewood 1; 41 - Mount Howitt 2; 42 - Wareena 1; 43 - Barrolka East 1; 44 - Cook North 1.

Following the methodology of Gallagher and Lambeck (1989) and Gallagher (1990), tectonic subsidence of these boreholes was recalculated using the "backstripping" procedure. Results were obtained for 140-0 Ma to coincide with the timeframe of the *CitcomS* models, whereby allowing for a direct comparison between results.

4.4.1 The Backstripping Procedure

Basin analysis is a complex undertaking, as multiple subsidence mechanisms can operate concurrently over the lifetime of a basin. "Backstrippping" is a procedure for isolating the component of subsidence attributed to "tectonic driving forces" (Steckler and Watts 1978). That is, by calculating how a basement would have subsided in the absence of sediment loading (and optionally sea level fluctuations), this process reveals which primary driving mechanisms contributed to the formation and evolution of the basin. The inclusion of a sea level model into the backstripping procedure requires a robust sea level model – otherwise artefacts may be introduced into the model. Beyond the scale of a single basin system, this subsidence analysis tool enables comparisons to be made between basins, and

can allow conclusions to be drawn about the evolution of plate margins and tectonic histories of large intracratonic regions.

Backstripping requires data retrieved from a sedimentary section. That is, unit thicknesses, ages, lithologies and water depths at time of deposition. Combined with these observations, a number of assumptions regarding the lithology and burial history of each unit are required to complete the procedure. A major assumption relates to the time-dependent porosity of each layer.

4.4.1.1 The Decompaction Process

As sediments generally undergo compaction during burial, observed layer thicknesses do not equate to their thicknesses at time of deposition (Steckler and Watts, 1978). The weight of overlying layers of sediment causes a decrease in porosity as pore waters escape leaving the cavities to collapse. Therefore, to ascertain the correct position of the basement at a given time, a sedimentary unit must first be restored to its original thickness. This task of 'decompaction' is a complex iterative procedure that forms a vital component of backstripping. It is achieved using a porosity-depth relationship assumed to represent how the porosity of a given lithology decreases with increasing depth.

For example, a unit of sediments is placed at its correct depth along the porosity-depth curve; this depth will vary with time, naturally becoming greater as more units are deposited on top of it and the basin subsides beneath (Figure 17). It is then initially decompacted using the average porosity that corresponds to the occupied portion of the porosity-depth curve. This first result will be an overestimate, as the average porosity will not adequately reflect the decay of porosity with depth. As a result, the layer will be decompacted multiple times, each time with an adjusted average porosity value representing the slightly differing portion of the porosity-depth curve to which the layer corresponds. The thickness of the layer will become smaller (compared to the initial decompaction) and eventually converge. Although minor details of how decompation is carried out may vary between applications, the preceding example gives an overview of which calculations are involved.

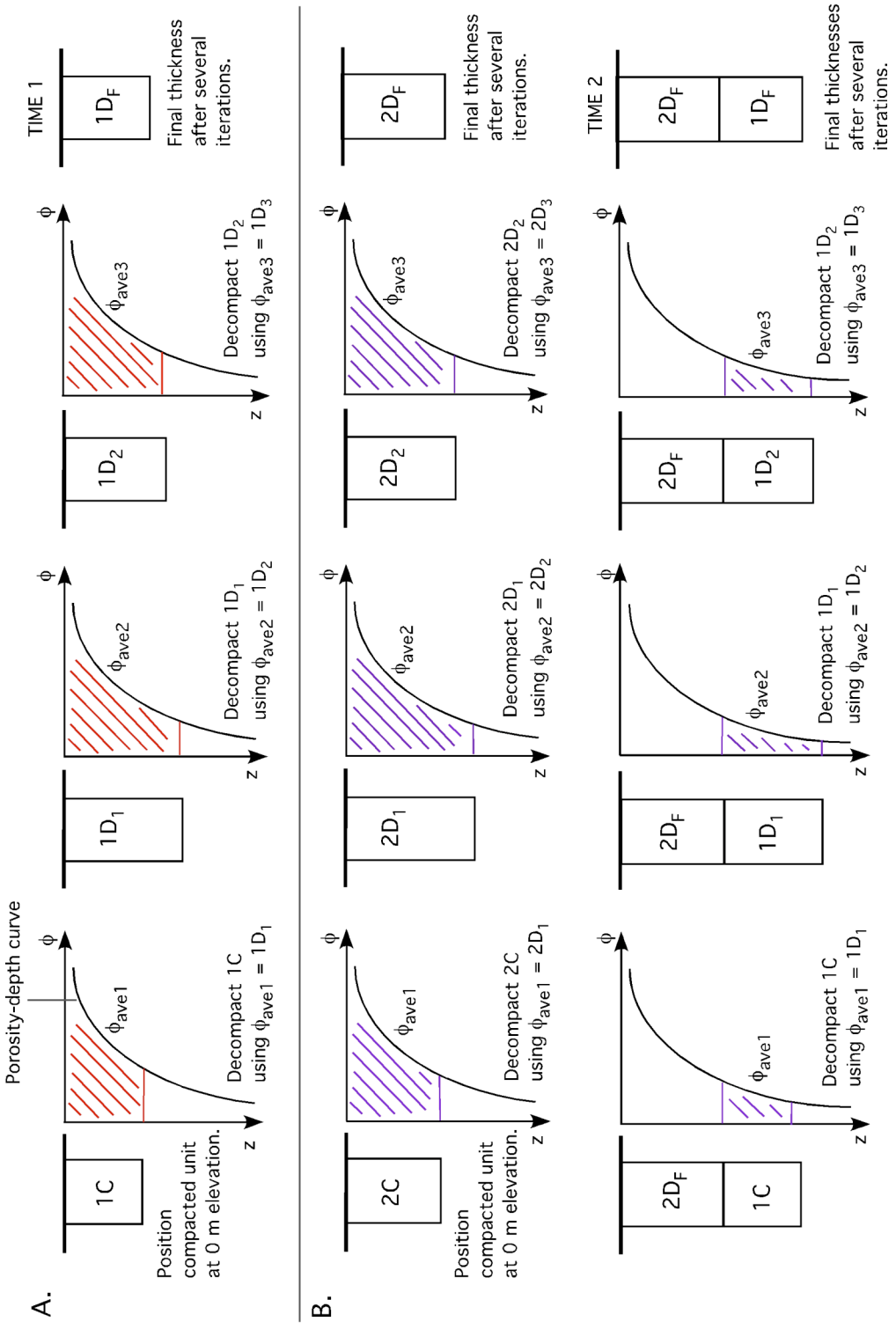

Figure 17. Schematic illustrating the decompaction process. (A) The oldest compacted unit (1'C') is placed at 0 m elevation (this is a datum that is set at 0 m at the beginning of the subsidence period being modelled) and decompacted (1'D_1') using the average porosity (ϕ_{ave1}) corresponding to the depth range the fully compacted unit occupies along the porosity-depth curve (red shaded section). This process is repeated, each time with a slightly adjusted porosity value ϕ_{ave2+} to match the adjusted depth the unit (D_{2+}) occupies along the porosity-depth curve. After several iterations the thickness of the layer will converge ($1D_F$). (B) This process is repeated for younger units. Each time the process is repeated, the thickness of older units will need to be recalculated sequentially from youngest to oldest, to reflect their new positions along the porosity-depth curve.

When performing the backstripping methodology it must also be considered that cementation can occur during the burial history of a sedimentary unit. This second mechanism for porosity reduction will have a different effect on the thickness of a layer during burial, and can result in an observed unit thickness being the same as its palaeo-thickness.

4.4.1.2 Calculating Tectonic Subsidence

The vertical motion of the basement is calculated forward in time by removing the loading effects of each layer individually in turn (oldest to youngest). To do this, the top of the fully decompacted unit is first placed at 0 m elevation (this is a datum that is set at 0 m at the beginning of the subsidence period being modelled) then all the sediments are removed and the basement is allowed to isostatically rebound to its water loaded position. To compute tectonic subsidence for the next time interval, the second unit is again fully decompacted and placed at 0 m elevation. The underlying first unit is then re-decompacted to account for its new deeper position along the porosity-depth curve, which will consequently result in its decompacted thickness being smaller than in the previous calculation. All the solid sediments are once more removed leaving the basement to readjust. This iterative process is repeated for subsequent units. Chronicling the depths to basement obtained after sediments are backstripped, reveals the tectonic subsidence history for the basin. This complicated procedure is outlined in Figure 18.

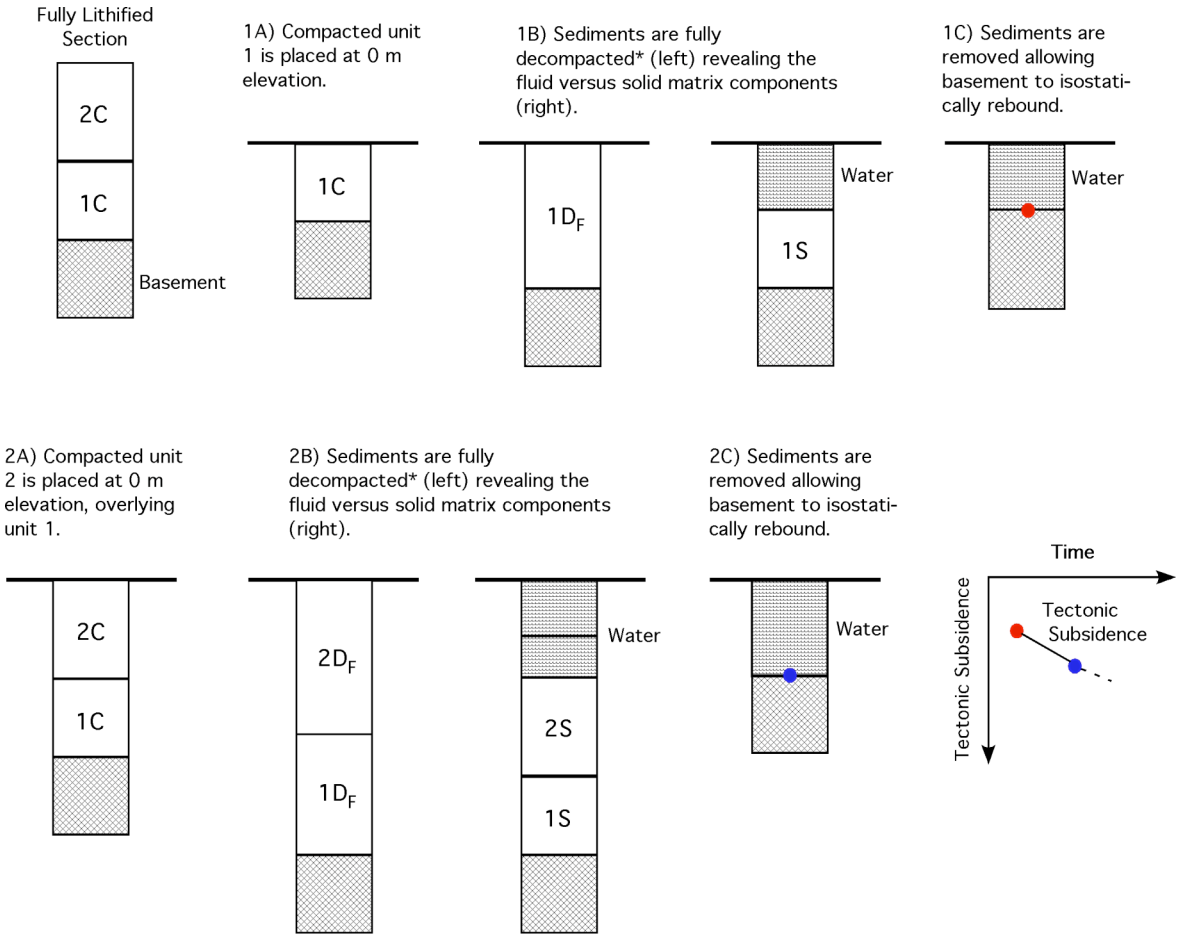

Figure 18. Schematic illustrating the basic principles of the backstripping procedure. C – compacted unit, D_F – fully decompacted unit, S – solid matrix component. *See Figure 17 for a pictorial representation of the decompaction procedure.

4.4.2 Application of Backstripping to Eastern Australia

Sediments from the 42 wells were decompacted using Gallagher's (1990) porosity depth relationship:

$$\phi(z) = \phi_o e^{-cz}, \qquad (5)$$

where ϕ is porosity, z is depth, ϕ_o is porosity at z=0 and c is a constant representing porosity decrease with depth. For simplicity it was assumed that there was no cementation. The tectonic subsidence was then calculated using the following equation that assumes Airy (local) isostasy:

$$H_b = \{[(\rho_m - \rho_s)H_s - \rho_m H_{sl}]/(\rho_m - \rho_w)\} + H_w, \qquad (6)$$

where H_b is the tectonic subsidence, H_s is the sediment thickness, H_{sl} is the difference between the sea-level at time of deposition and present sea-level, H_w is the water depth at time of deposition, ρ_m is mantle density, ρ_s is sediment density, and ρ_w is water density (i.e. sea-water). Gallagher (1990) considered Airy isostasy appropriate, as the scales of the basins are small enough that omitting any flexural responses to the sediment loading will not significantly alter the trends in the results. It is the trends in tectonic subsidence that are considered most valuable rather than precise magnitudes.

As shallow marine conditions prevailed during the Cretaceous (e.g. Exon, 1976; Exon and Senior, 1976; Senior et al., 1978) water depths (H_w) were not included in the backstripping calculations. Estimating palaeo-water depths is a complex procedure that involves the identification of microfossils and the range of water depths they inhabited. This assumption that sediments completely filled the accommodation space therefore avoids the error associated with uncertainties in assigning palaeo-water depths to individual units. It is therefore further assumed, that any error associated with excluding water depth would have been smaller than inaccuracies associated with microfossil analysis.

4.4.3 Inherent Calculation Errors

Although the computed tectonic subsidence data are referred to as "observational", backstripping is in fact a kind of 'model'. Due to the required assumptions and unknowns, the resultant subsidence "observations" are not purely unbiased by calculation parameters. The errors associated with the assumed porosity-depth relationship were quantified by testing different values of ϕ_0 and c (equation (5) above) (Table 9). These are represented by shaded error polygons in subsequent tectonic subsidence plots.

Table 9. Best fit, upper and lower values of ϕ_0 and c, for each type of lithology, used to compute tectonic subsidence (equation 4) (Gallagher, 1990).

Lithology	Best Fit		Upper		Lower		Grain Density ρ_g (kgm^{-3})
	ϕ_0 (%)	c (km^{-1})	ϕ_0 (%)	c (km^{-1})	ϕ_0 (%)	c (km^{-1})	
Sandstone	43.0	0.718	48.0	0.567	38.0	0.987	2670
Siltstone	45.7	1.158	51.0	0.965	41.0	1.310	2680
Shale	50.4	1.616	55.0	1.300	45.0	1.760	2680

4.4.4 Timescale Conversion

The formation ages of the original borehole data interpreted by Gallagher (1990) corresponded to the timescale of Harland et al. (1982). However, to uphold consistency and allow for a more valid comparison with the *CitcomS* models, these age data were converted to the timescales of Cande and Kent (1995) (0-83.5 Ma) and Gradstein et al. (1994) (>83.5 Ma). These latter two timescales were used in the generation of input files for the *CitcomS* models.

It can be seen from Figures 19-20 below, that there are only minor differences between the original timescale and the newer ones. During the Cretaceous, ages from Harland et al. (1982) are 1.5-4 Myr younger than Gradstein et al. (1994). Whilst during the Cenozoic, ages from Harland et al. (1982) are only 0.5-2 Myr younger than Cande and Kent (1995).

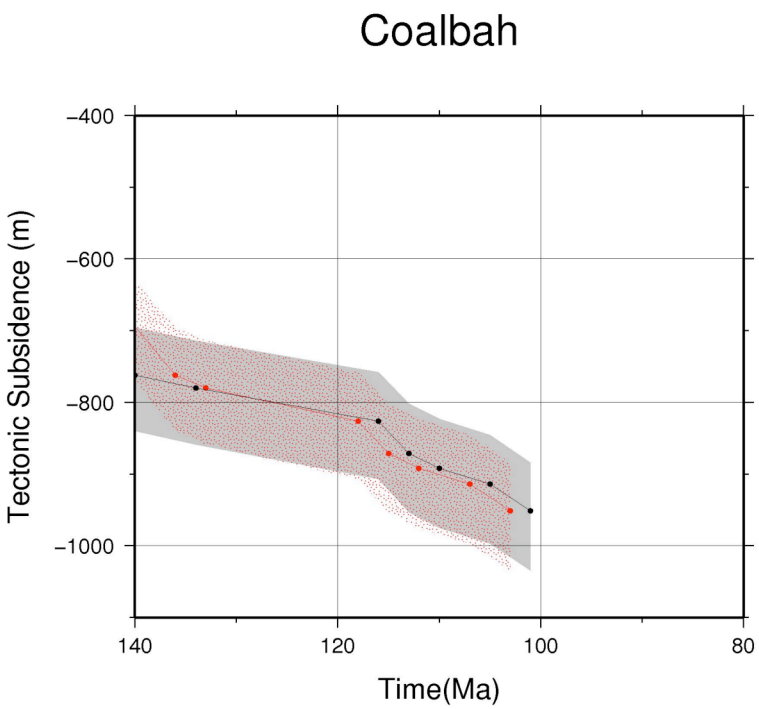

Figure 19. Tectonic subsidence curves for the location of Coalbah 1 (Surat Basin) based on different timescales: Harland et al. (1982) (black), and Cande and Kent (1995) and Gradstein et al. (1994) (red). Ages that data were sampled from are marked with filled circles and shaded regions define error polygons.

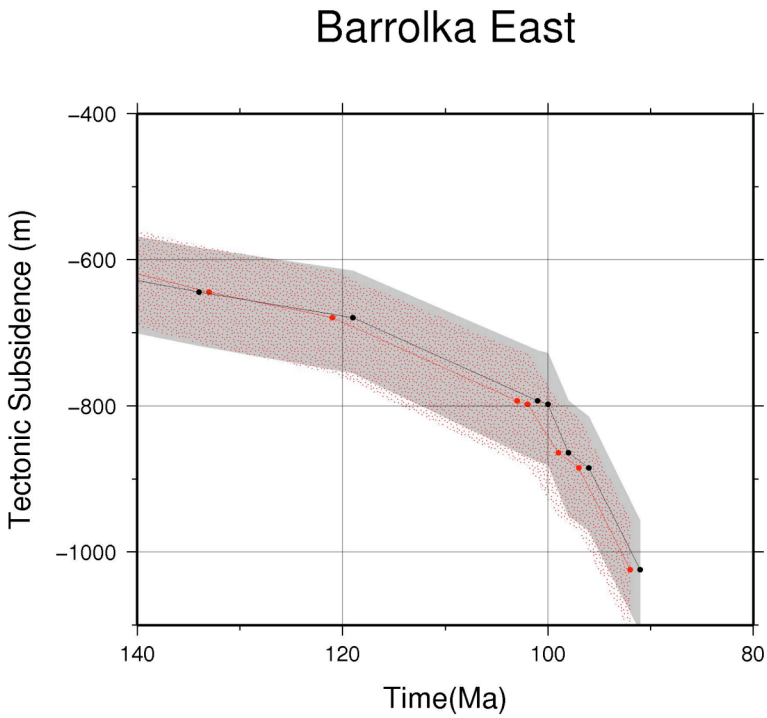

Figure 20. Tectonic subsidence curves at the location of Barrolka East 1 (Eromanga Basin) based on different timescales: Harland et al. (1982) (black) and Cande and Kent (1995) and Gradstein et al. (1994) (red). Ages that data were sampled from are marked with filled circles and shaded regions define error polygons.

4.5 Seismic Tomography

Seismic tomography enables 2- and 3-dimensional imaging of the Earth's interior. It is a complex procedure that relies on establishing how fast seismic waves (elastic waves), such as those generated by earthquakes, travel through the Earth. This information is then used to isolate regions of anomalously fast or slow velocities; judged as deviations from a global reference model (e.g. PREM – Dziewonski and Anderson, 1981; Figure 21). As the speed of seismic waves is influenced by density and modulus, which are in turn influenced by temperature, composition and phase, correlating seismic anomalies with deep Earth structures is not straightforward.

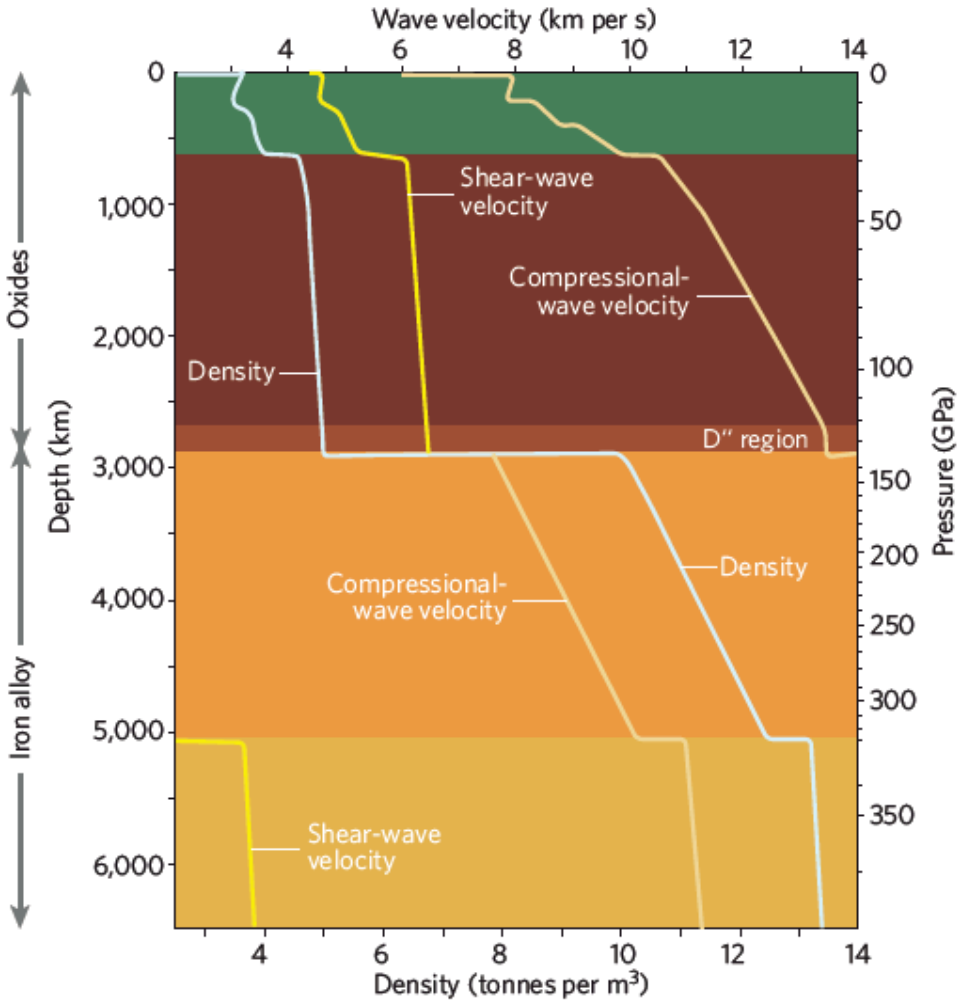

Figure 21. Radial structure of the Earth as inferred from density, and P-wave ("Compressional-wave) and S-wave velocity (Shear-wave) changes with depth (from Romanowicz, 2008). Crust and upper mantle – green, lower mantle – dark brown, D" region – light brown, outer core – orange, and inner core – yellow. Data are taken from the 1-D global seismic reference model 'PREM' of Dziewonski and Anderson (1981).

4.5.1 P- and S-wave Tomography Models

Tomography images can be constructed from P- or S-wave arrival times. P- and S-waves are elastic body waves; P-wave motion is parallel to the direction of wave propagation (causing compression and rarefraction), where as S-waves motion is perpendicular to direction of propagation (causing shear). Romanowicz (2003) discussed the relative merits of P- versus S-wave tomography models: P-wave models are particularly valuable for imaging subduction zones in high-resolution due to the high concentration of receiver stations in proximity to seismic wave sources (earthquakes), whereas S-wave models provide better coverage of large wavelength features and ocean basins due to the sampling of broadband data. As a result, P-wave models can be referred to as high-resolution models and S-wave models as long wavelength models. Incorporating arrival times of surface waves (e.g. Rayleigh waves) and converted waves (e.g. surface reflected waves – PP, SS, or waves converted at the liquid outer core boundary – PKP, SKS) help to improve resolution.

4.5.2 Application of Seismic Tomography to Validating Geodynamic Models

Seismic tomography provides a means to validate mantle convection models. As the speed of seismic wave propagation is influenced by temperature, comparing tomography images to equivalent model temperature cross-sections reveals similarities and differences between the 'observed' and predicted mantle structure. Although seismic tomography is itself a modelling technique, results are here after referred to as 'observed' as they are derived from present-day geological data.

In order to validate the preferred *CitcomS* models, the ~0 Ma temperature fields were compared to a series of equivalent whole-mantle seismic tomography images (Table 10). Vertical cross-sections were aligned E-W through the Eromanga and Surat basins (Figure 22).

Table 10. Seismic tomography models used to validate *CitcomS* models.

Model	Body Waves Used	Reference
S20RTS	S-waves	Ritsema et al. (1999)
TX2007	S-waves	Simmons et al. (2007)
TXBW	S-waves	Grand (2002)
MITP08	P-waves	Li et al. (2008)
PRI-P05	P-waves	Montelli et al. (2006)

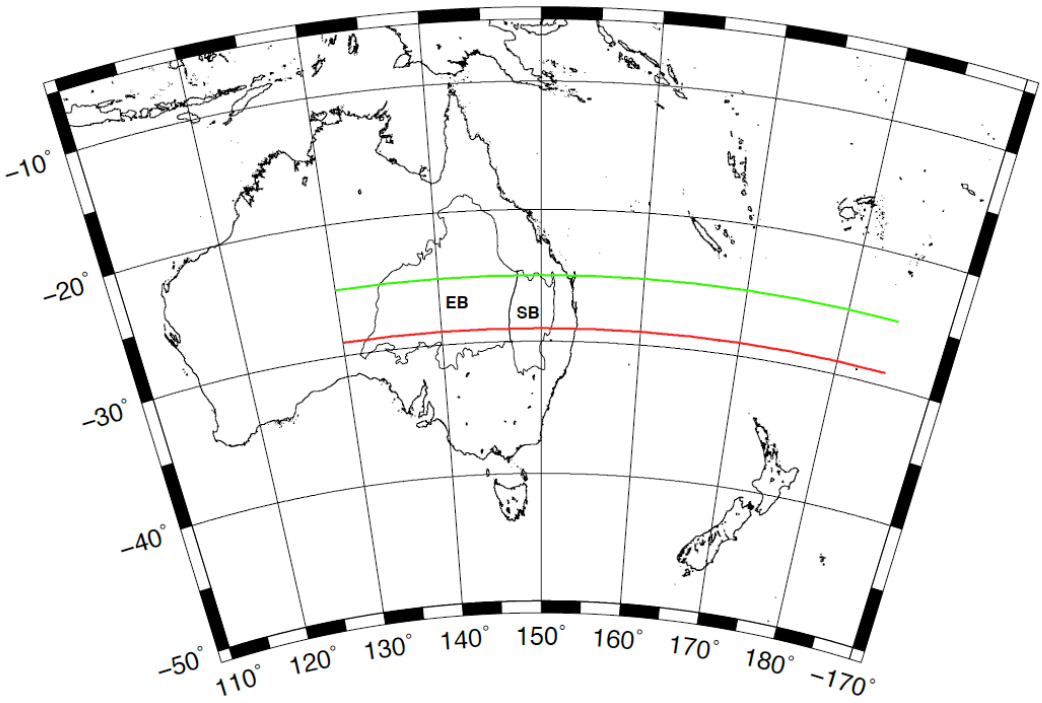

Figure 22. Location map of Australia and the western Pacific, including outlines of the Eromanga (EB) and Surat basins (SB). Locations where seismic tomography and *CitcomS* temperature cross-sections were produced are shown; green – north profile and red – south profile.

5 Results

5.1 Modelled Mantle Evolution Since 140 Ma

5.1.1 Initial Mantle Material Parameter Analysis

Mantle material parameters were altered in a series of model runs with the subduction zone positioned adjacent to the reconstructed continental margin 140 Ma (see Appendix 1 for the complete set of images for each model). These initial models formed a parameter analysis, whereby mantle viscosities, convectivity (via the Rayleigh number) and the temperature contrast between the mantle and slab were varied to test their influence on mantle evolution and dynamic topography. Our knowledge of the mantle is mainly derived from indirect measuring techniques, such as seismic tomography, post-glacial rebound analyses and geochemical analyses of "mantle-rocks" exposed at the surface (e.g. Xenoliths). As a result it is important to consider a range of different parameter values to account for uncertainties associated with these measurements.

As discussed in DiCaprio (2009), subducting slab material initially becomes smeared out along the 660 km phase boundary as the Australian plate migrates eastwards and the subduction hinge rolls back. This pattern continues until the earliest Cenozoic, when Australia commences northward motion. Due to an increased amount of eastward rotation of the Australian plate in the south, the volume of slab material that becomes trapped in the transition zone decreases in a northward direction (Figure 23). Although subduction ends in the Late Cretaceous, slab material trapped in the upper mantle continues to be dragged laterally by the overlying plate. The slab never becomes fully detached from the surface, and remains connected to the base of the lithosphere at ~150-160ºE at present-day. Beneath Australia and as far south as the Australian-Antarctic Discordance, thermally diffusing Cretaceous slab material remains trapped in the transition zone, approximately 40 Myr after subduction ends.

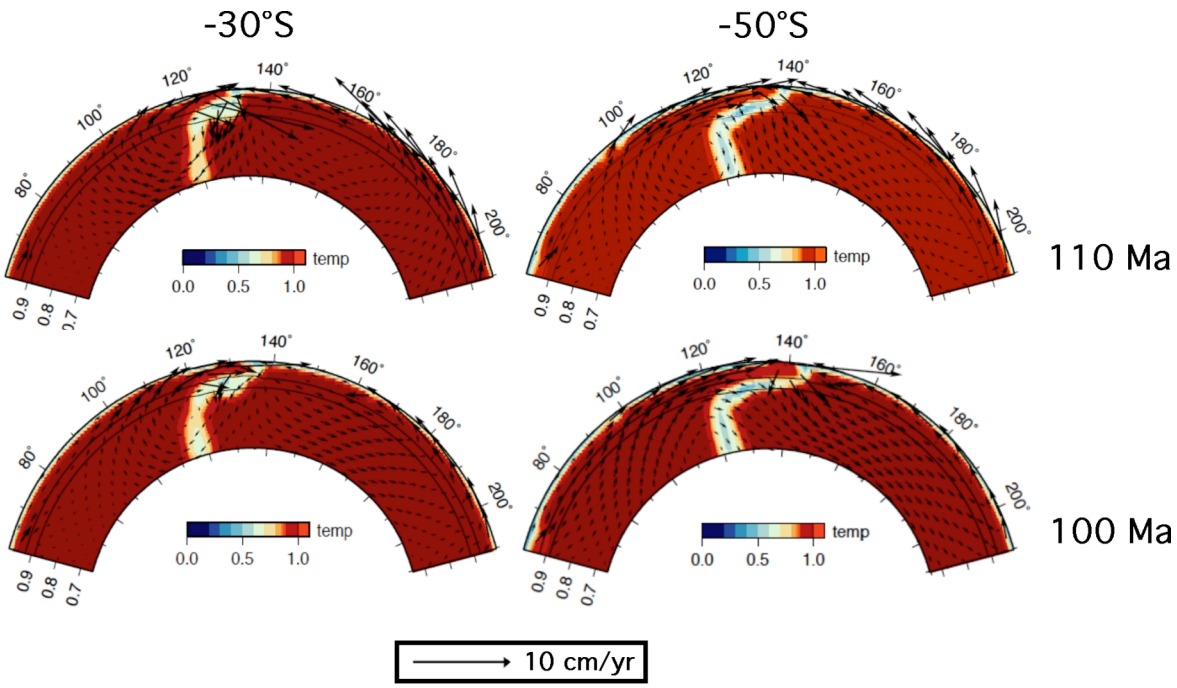

Figure 23. Mantle temperature cross-sections through the reference model (model RM) at different latitudes and times. The increased lateral smearing of the slab across the transition zone (bounded by black lines) in the south reflects a larger degree of eastward rotation (right). Depths and temperatures are non-dimensionalised (see section 4.3.1).

Varying the viscosities of the upper and lower mantle affects how long the slab remains in the transition zone. When the viscosity of the upper mantle is reduced to 5×10^{20} Pa s (simulating a weak asthenosphere component), slab material more rapidly descends through the upper mantle and subsequently penetrates the lower mantle sooner (Figure 24 – note the increased portion of slab material in the lower mantle in the model with lower η_{UM} compared to the reference model). In simulations with a strong upper and lower mantle, the slab material stays trapped in the transition zone for longer (Figure 2 – note the increased portion of slab material smeared out along the transition zone in the reference model and model with higher η_{LM} compared to the model with lower η_{UM}, particularly at 100 Ma around the time subduction ceases). Eastward migration of the slab hinge also results in the surface driving force of subduction being further away from the already subducted slab material, which may in turn accentuate this smearing effect.

Figure 24. Mantle temperature cross-sections at 50ºS through models (A) RM, (B) RM_2 (weak upper mantle) and (C) RM_3 (very strong lower mantle), at four different times in the Cretaceous. Between 120-100 Ma a larger volume of slab material penetrates the lower mantle in model RM_2 compared to the reference model, conversely model RM_3 retains a larger portion of slab material in the transition zone (bounded by black lines) compared to the reference model.

The Rayleigh number (Ra) is a measure of convectivity. It was varied to see how convective vigour affects slab and mantle evolution. Higher Rayleigh numbers indicate more vigorous convection, or rather a more 'mobile' system. Doubling the Rayleigh number relative to the reference model (to 2.7152×10^8) results in slab material more readily penetrating the lower mantle, with a diminished smearing effect observed at the transition zone (Figure 25). Stronger convection produces less resistance to the descent of the slab; it is essentially analogous to having a lower viscosity or higher temperature system. In the high Rayleigh number simulations, thermal diffusion is increased and the slab loses its shape more rapidly relative to the other simulations. DiCaprio (2009) observed that models with a strong upper and lower mantle (high η_{UM} and η_{LM}, respectively) result in slabs maintaining their shapes throughout the simulations. This is also observed when the Rayleigh number is reduced. Reducing the Rayleigh number by half (to 6.788×10^7) decreases convective vigour and thermal diffusion. In lower Rayleigh number simulations the smearing effect becomes particularly pronounced, similar to models with a very strong lower mantle (high η_{LM}) (Figure 24). These observations reflect that the system is less 'mobile' compared to higher Rayleigh number models.

Figure 25. Mantle temperature cross-sections at 50ºS through models (A) RM (reference model), (B) RM_4 (2x reference Ra) and (C) RM_5 (0.5x reference Rayleigh number), at four different times in the Cretaceous. As the Rayleigh number increases, the shape of the slab becomes deformed and there is faster descent through the transition zone (bounded by black lines) and the lower mantle.

Reducing the temperature contrast between the slab and mantle was achieved by generating a warmer slab as an initial condition. From Figure 26 it can be seen that the core of the slab is 50% warmer than in the previous simulations, with a non-dimensional temperature of approximately 0.75 compared to 0.5 at its core (see section 4.3.1 for non-dimensionalisation of temperature). Similarly to models with a reduced Ra and very strong lower mantle (high η_{LM}), a warmer slab generates a smearing effect that is particularly prominent, with more slab material stalling in the transition zone. This is likely a result of the lower density slab having a decreased downward driving force compared to the reference model.

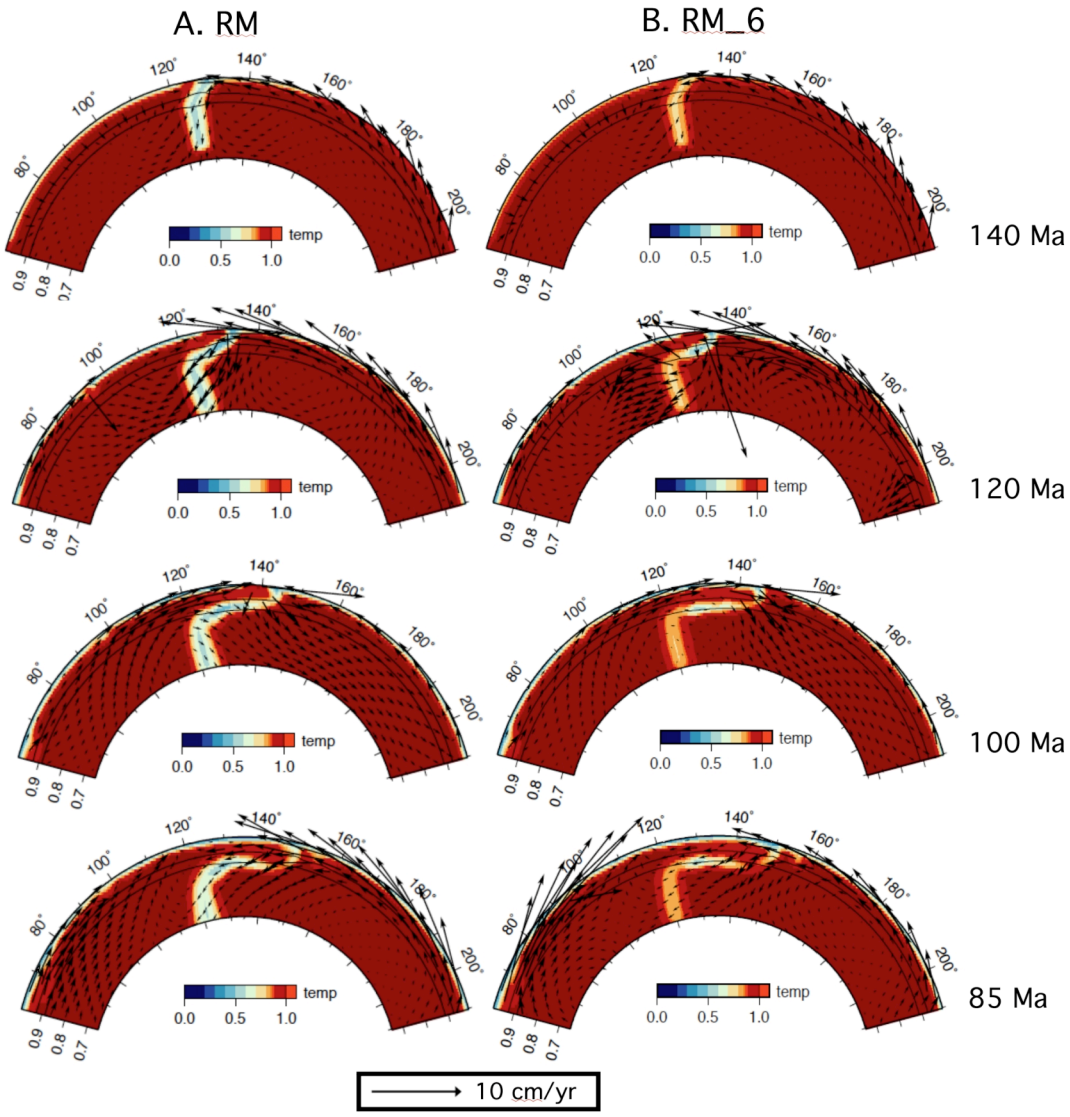

Figure 26. Mantle temperature cross-sections at 50ºS through models (A) RM and (B) RM_6, at four different times in the Cretaceous. Reducing the initial temperature contrast between the slab and the mantle results in a larger volume of slab material being retained in the transition zone in the Late Cretaceous.

The ‘Reference Model’ (RM) model series demonstrates how mantle rheological parameters affect the evolution of the mantle over 140 Myr. Results highlight their ability to increase or decrease resistance to the descent of a subducted slab (Figure 27). This is particularly evident when regarding the slab’s interaction with the 660 km phase boundary. While the slab evolved differently between the simulations, a noticeable commonality between the models is that the slab material is almost immediately descending through the mantle beneath the Eromanga and Surat basins in eastern Australia.

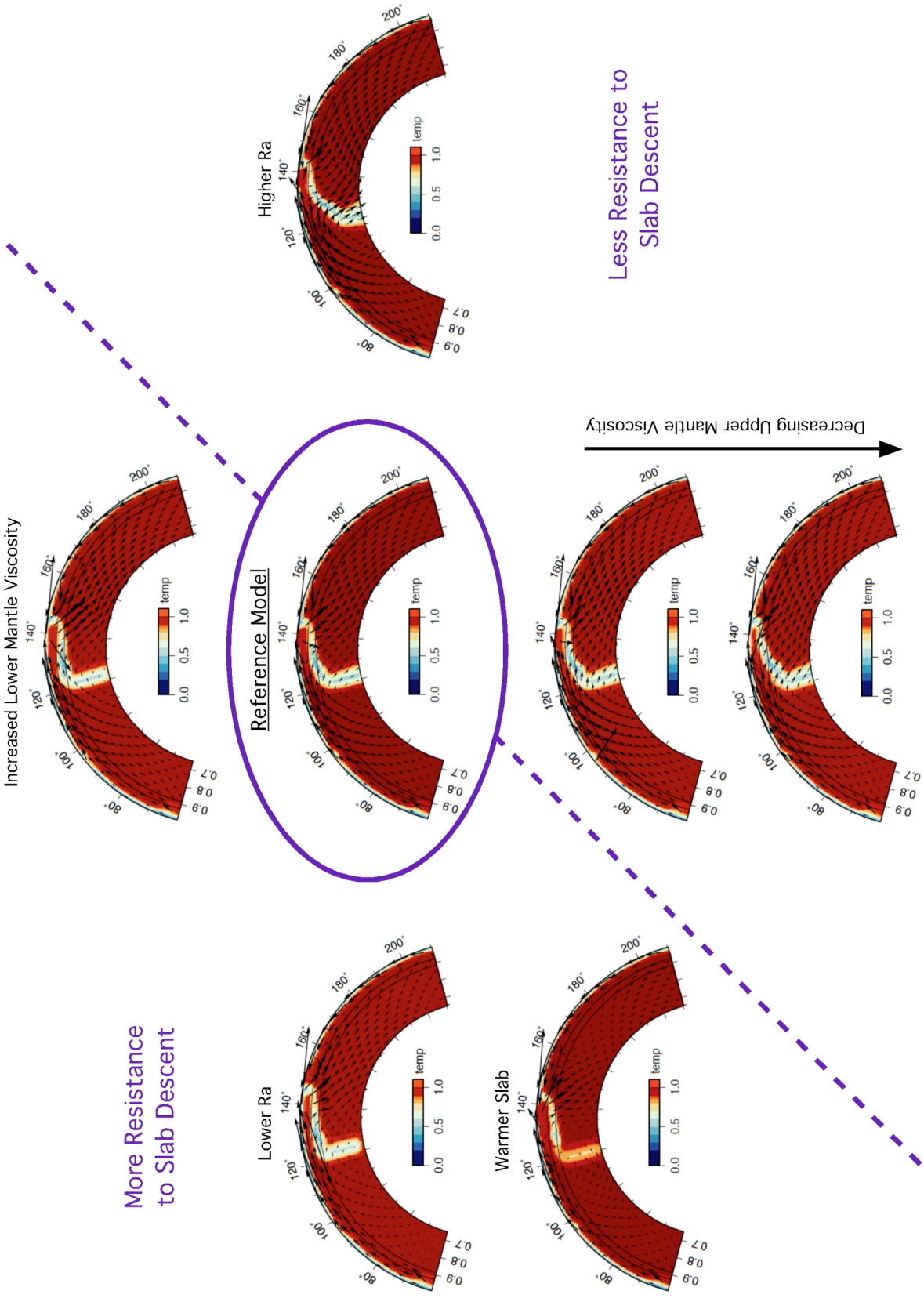

Figure 27. Mantle temperature cross-sections for each model in the RM model series, at 100 Ma. Cross-sections have a constant latitude of 50°S. Comparing the shape and depth of the slab between the models highlights how the altered mantle property affects the descent of the slab. Mantle properties that tend to resist the descent of the slab, compared to the reference model, are placed above the dashed line. While mantle conditions that pose less resistance to the descending slab are positioned below the dashed line.

5.1.2 Models with Subduction Shifted East

The most dominant effects of translating the subduction zone 23º east are (1) a delay in the timing of slab material intersecting the mantle beneath eastern Australia and (2) a reduced tendency for the slab material to stall in the transition zone. In the series of models with the subduction zone shifted east (the Slab23E model series – see Appendix 1 for the complete set of images for each model), the subducted slab is positioned beneath the Eromanga-Surat Basin System at ~120 Ma, approximately 20 Myr later than in the RM model series with subduction adjacent to the continental margin. These observations highlight the control that plate boundary geometries exert over mantle evolution. Slab evolution in the Slab23E model series also differs significantly from the RM model series. The slab appears to efficiently penetrate the lower mantle, even in simulations with identical mantle parameters (Figure 28). Less slab material becomes stalled in the transition zone as in previous models and lateral smearing across the 660 km boundary is less prominent. These observations are due in part to initial slab depth, compounded in the north by slab detachment.

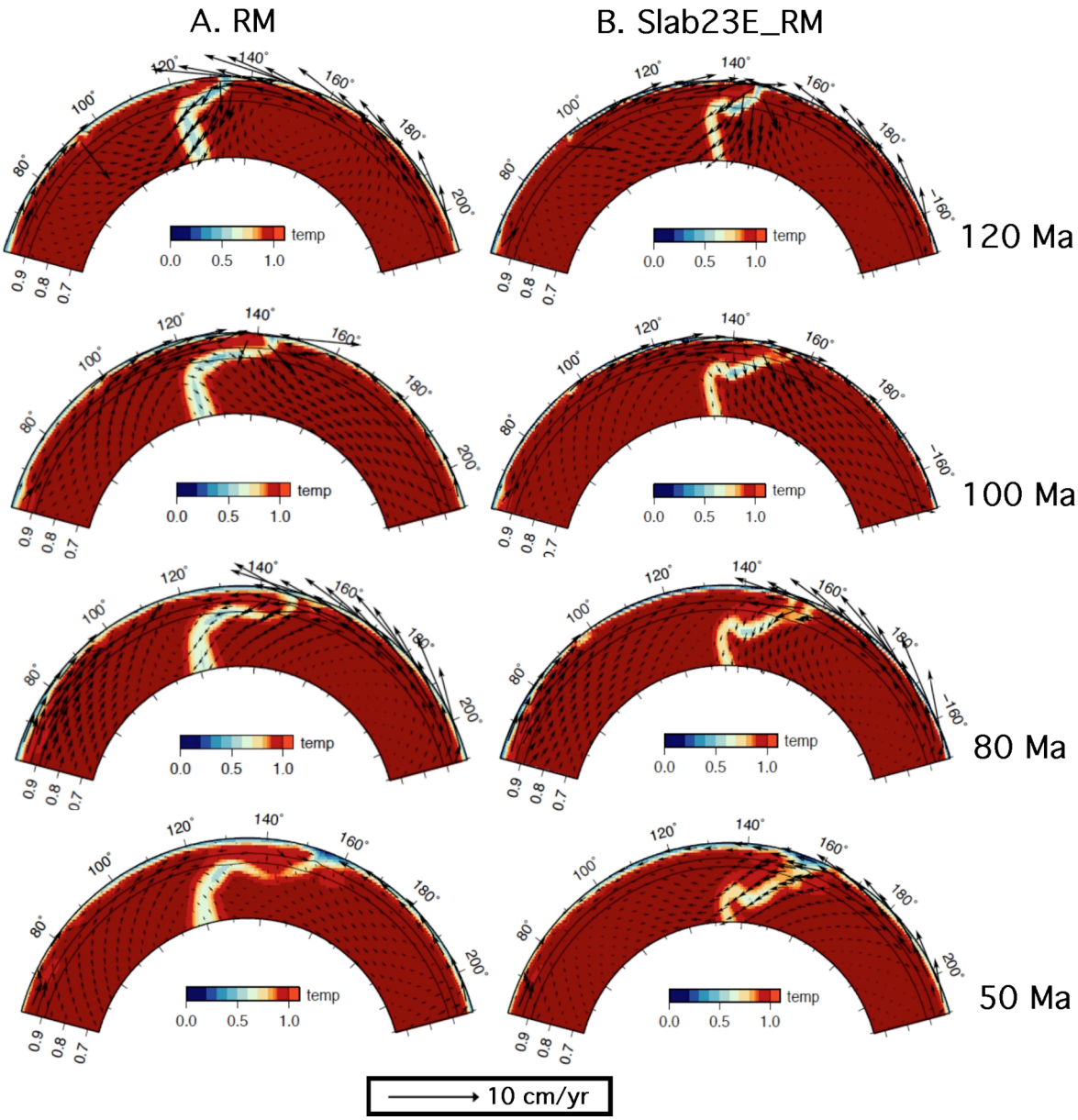

Figure 28. Mantle temperature cross-sections at 50ºS through (A) the reference model (model RM) and (B) the reference model with subduction shifted east by 23º (model Slab23E_RM), at four different times in the Cretaceous and Earliest Cenozoic. When subduction is shifted east (B) there appears to be minimal impediment to the slab's descent through the mantle.

In the Slab23E model series, the initial conditions were altered so that the slab extends to a greater depth than in the RM model series. From Figure 4 it can be seen that the slab is initialised to a depth of ~1900 km (a non-dimensionalised value of 0.7) in model RM, however in model Slab23E it extends to the core-mantle boundary. As there is more slab material, there is a greater pull acting on slab material at shallower levels. Thus extending the length of the slab increases the downward driving force, facilitating its descent. Although the slab remains approximately connected to the surface along the southern

section of the subduction zone, for example ~50ºS (13ºS in the rotated reference frame), further north ~30ºS (9ºN in the rotated reference frame) it completely detaches at approximately 97 Ma (Figure 29). This may have the effect of a "sinking stone" dragging material downwards. That is, as the slab is no longer tethered to the surface and being pulled laterally by the moving plates it is free to sink vertically. The complete series of images for model Slab23E shows that once the slab becomes detached it sinks vertically, easily penetrating the 660 km boundary where it continues to sink at a slower rate through the more viscous upper lower mantle (Appendix 1).

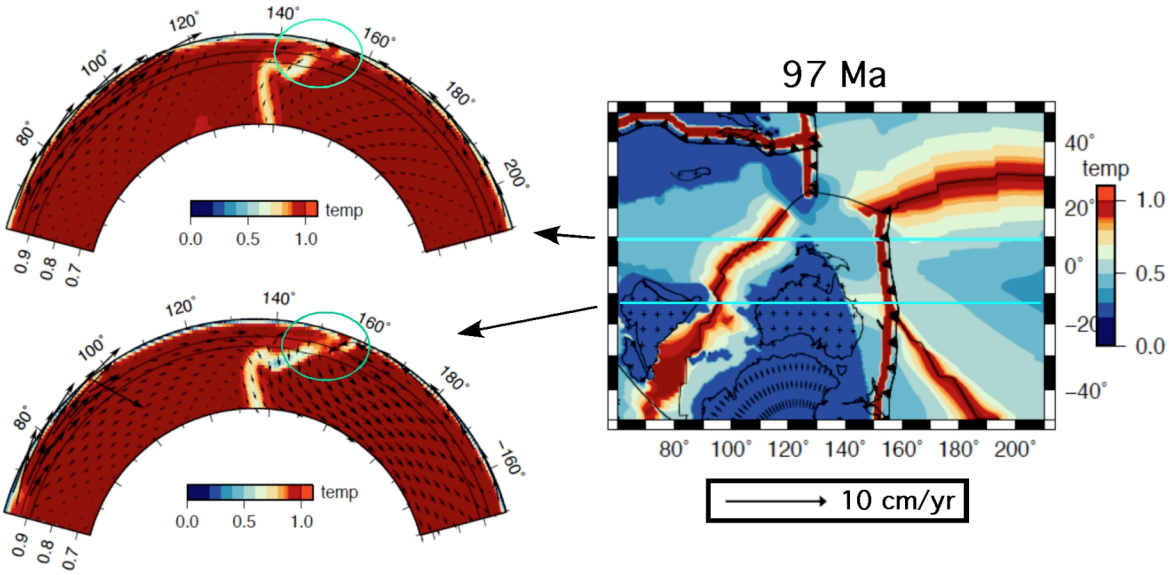

Figure 29. Mantle temperature cross-sections through model Slab23E_RM (left) at ~30ºS (9ºN in rotated reference frame) and ~50ºS (13ºS in rotated reference frame) highlighting slab detachment in the north. Location map (right), reconstructed to 97 Ma, showing surface temperatures.

5.2 Modelled Surface Evolution Since 140 Ma

Dynamic topography was computed from the *CitcomS* model output by assessing the influence of mantle flow on the vertical motion of the surface (see Appendix 1 for the complete set of dynamic topography images for each model run). The major trend consistent between all model runs is the immediate development of a band of negative topography west of the subduction zone. As Australia migrates east between 140-99 Ma this region of negative topography propagates westwards until it covers eastern Australia. The E-W extent of the negative dynamic topography is related to the extent and displacement of the slab material in the underlying mantle below. Although negative dynamic topography forms a maximum band ~40-50º in width for both series of models during active subduction, in the models with subduction adjacent to the continental margin the influence of negative dynamic topography extends further west into the continental interior. Figure 7 illustrates the lateral extent of the negative dynamic topography signal at 100 Ma, highlighting that the entire continent is affected when subduction is adjacent to the eastern margin (Figure 30A).

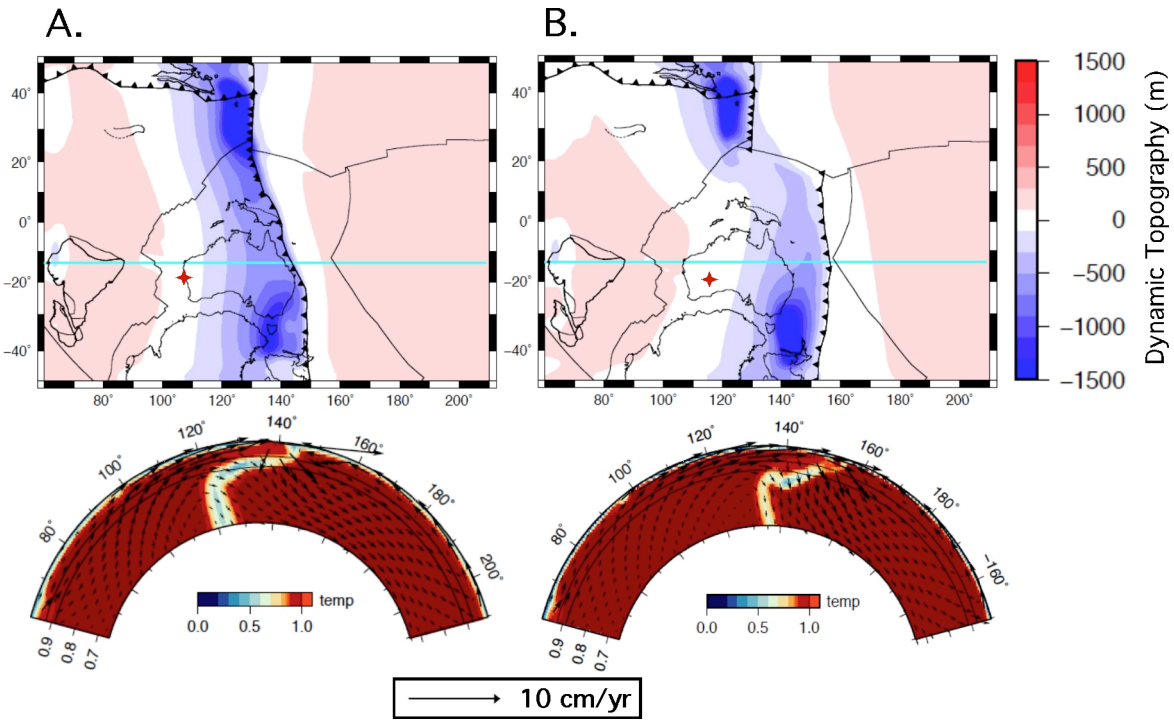

Figure 30. Surface dynamic topography (top) and mantle temperature cross-sections (bottom) at 100 Ma for models (A) RM and (B) Slab23E_RM. The location of negative surface dynamic topography correlates with the position of the slab at shallow levels in the mantle. As the slab is further west in (A), surface dynamic topography extends further west. Red star marks the western limits of negative dynamic topography on the Australian continent.

The magnitude of the negative dynamic topography signal and rate of subsidence are closely related to distance from the subduction zone, depth of the slab and the mantle material properties. When the slab is close to the surface the dynamic topography signal is stronger, and as the slab sinks deeper into the mantle the surface relatively uplifts as the negative signal diminishes in magnitude. The effects of dynamic corner flow (Mitrovica et al., 1989) on dynamic topography in eastern Australia are therefore amplified when the arc corner is situated closer to the continent; tilting of the continent increases towards the subduction zone. When subduction is modelled adjacent to the reconstructed margin, slab material is sinking higher in the mantle beneath eastern Australia compared to when the subduction zone is further east, consequently the magnitude of negative dynamic topography is greater in these simulations. This is highlighted in Figure 31, where deeper blues are seen in eastern Australia for the reference model (model RM) compared to the model with subduction shifted east (model Slab23E_RM).

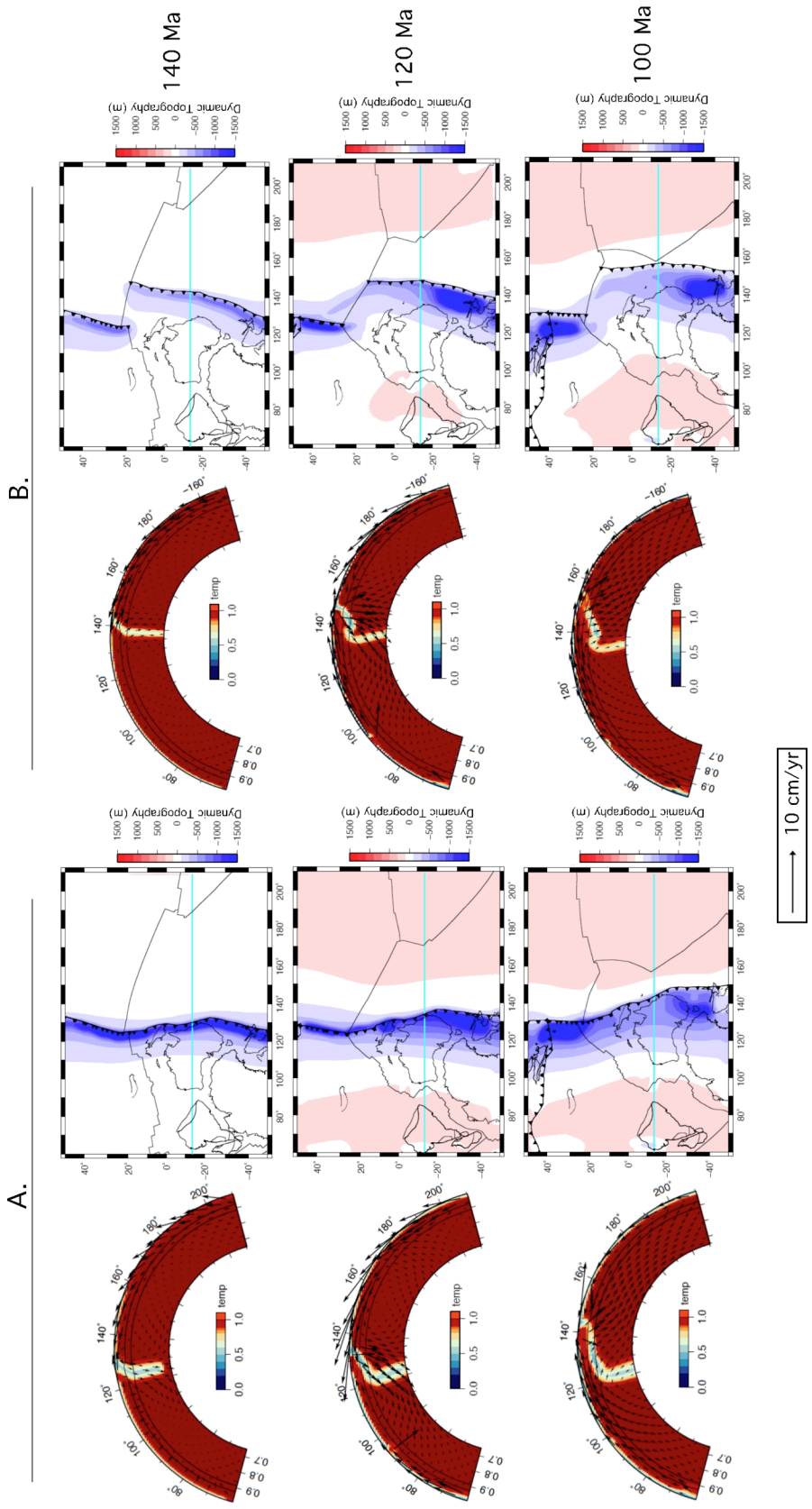

Figure 31. Mantle temperature cross-sections at ~50ºS (13ºS in rotated reference frame) and regional surface dynamic topography for models (A) RM and (B) Slab23E_RM, at three times in the Cretaceous. Eastern Australia experiences increased surface dynamic topography when subduction is adjacent to the palaeo-margin and when the slab is sinking through the mantle directly beneath (A).

The significance of mantle material properties to the magnitude of the surface dynamic topography signal is best highlighted in Figure 32, which shows surface dynamic topography at the borehole location Quilpie 1 in the Eromanga Basin, induced by different mantle conditions (see Appendix 2 for modelled tectonic subsidence at each borehole location). Increasing the Rayleigh number induces more vigorous convection (see section 5.1.1). This invokes less resistance for the subducting slab, which in turn drags down the overlying crust as it descends. As a result the model run with a Rayleigh number of 2.7152×10^8 (double the reference Ra) results in the maximum subsidence signal of all the model runs (model RM_4 – cyan line). The least amount of absolute subsidence results from reducing the Rayleigh number (model RM_5 – green line) or having a weaker upper mantle (model RM_2 – purple line). A mantle with reduced convective vigour (lower Rayleigh number) is more resistive to the descent of the slab. Hence the slab has a smaller down-going velocity, resulting in diminished subsidence. Subsidence can be regarded as a function of velocity and viscosity. Although the downward velocity of the slab may be larger when simulating a weaker upper mantle (low η_{UM}) as the slab is met with less resistance, the stresses associated with the slab's descent do not radiate as far. In higher viscosity regions, stresses exerted by a descending slab propagate over a larger distance. Although the downward velocities may be smaller when a strong upper and lower mantle is simulated (high η_{UM} and η_{LM}), the former effect dominates and subsidence is greater at the surface (models RM, RM_1 and RM_3 – red orange and blue lines, respectively).

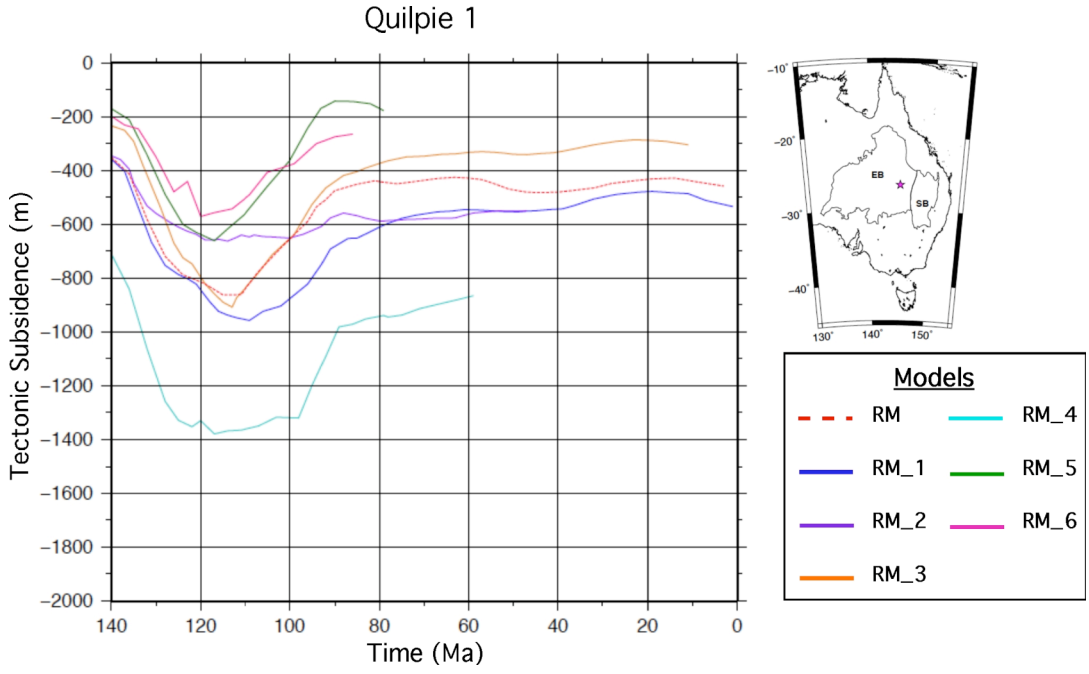

Figure 32. Model subsidence curves for Quilpie 1 in the Eromanga Basin (left), and location map (right). Coloured lines represent how the surface subsides and uplifts at that

location (star on location map) based on the different model parameters. EB – Eromanga Basin and SB – Surat Basin. See Table 7 for a list of mantle properties.

During the Cretaceous, increased negative dynamic topography, manifested as subsidence, occurs earlier in eastern Australia when the subduction zone is adjacent to the reconstructed margin. Subsidence accelerates almost instantly at the onset of the simulation (Figure 33). This is not surprising as oceanic crust is almost immediately descending through the mantle underlying Australia. The rate of subsidence does not increase significantly until ~20 Myr later (~120 Ma) when the subduction zone is shifted east.

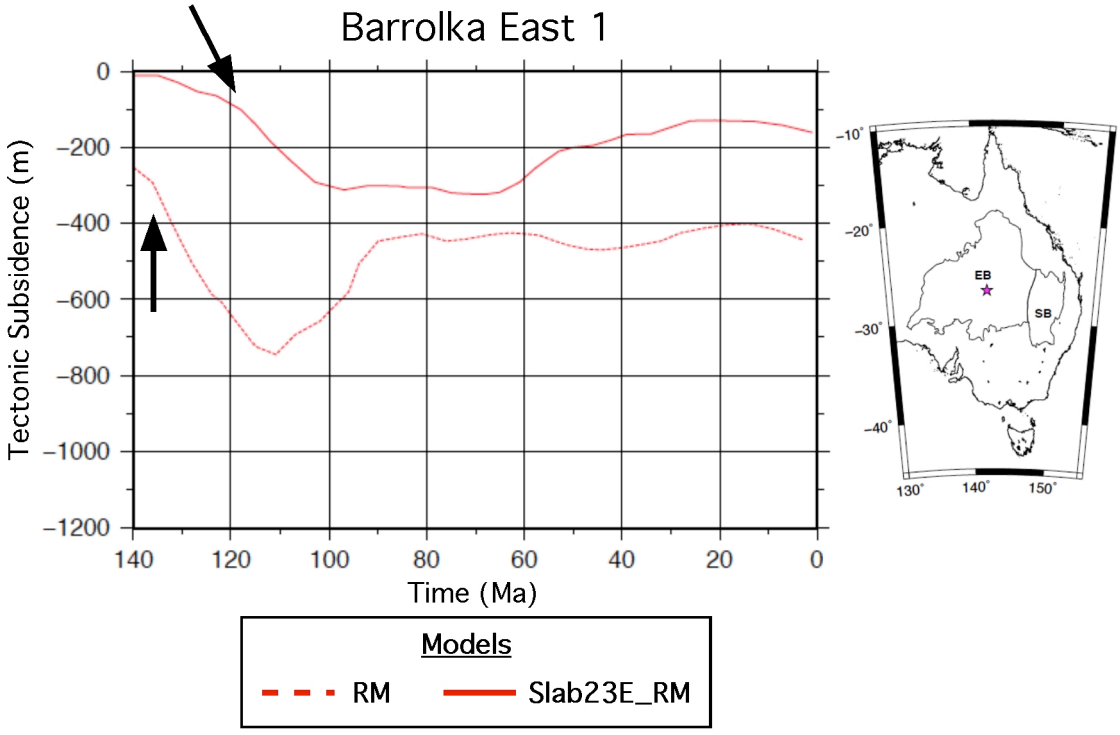

Figure 33. Model subsidence curves for Barrolka East 1 in the Eromanga Basin (left), and location map (right); star identifies the well site, EB – Eromanga Basin and SB – Surat Basin. Black arrows highlight the onset of increased subsidence, that is, ~140 Ma for the reference model (model RM – red dashed line) and ~120 Ma for model Slab23E_RM (solid red line).

A similarity between all the models is that timing of increased subsidence occurs simultaneously in the Surat Basin and the Eromanga Basin, however the magnitude of subsidence is higher and more laterally variable when subduction is adjacent to the reconstructed margin (Figure 34). This is probably because the slab is closer to the

surface, and it is positioned at a steep angle when below the basins. When the subduction zone is simulated further east, the slab is deeper in the mantle and lying at a relatively shallow angle by the time Eastern Australia passes over. Consistent between all models, is that the rate of subsidence in this episode is similar from E-W, with a slight increase in the east. For example, model Slab23E_RM predicts 14.9 m/Myr of subsidence between 120-100 Ma at the location of Basketyard Creek 1 in the Surat Basin (148.7ºE, 27.2ºS), grading to 11.1 m/Myr at the location of Cook North 1 in the Eromanga Basin (141.5ºE, 26.7ºS).

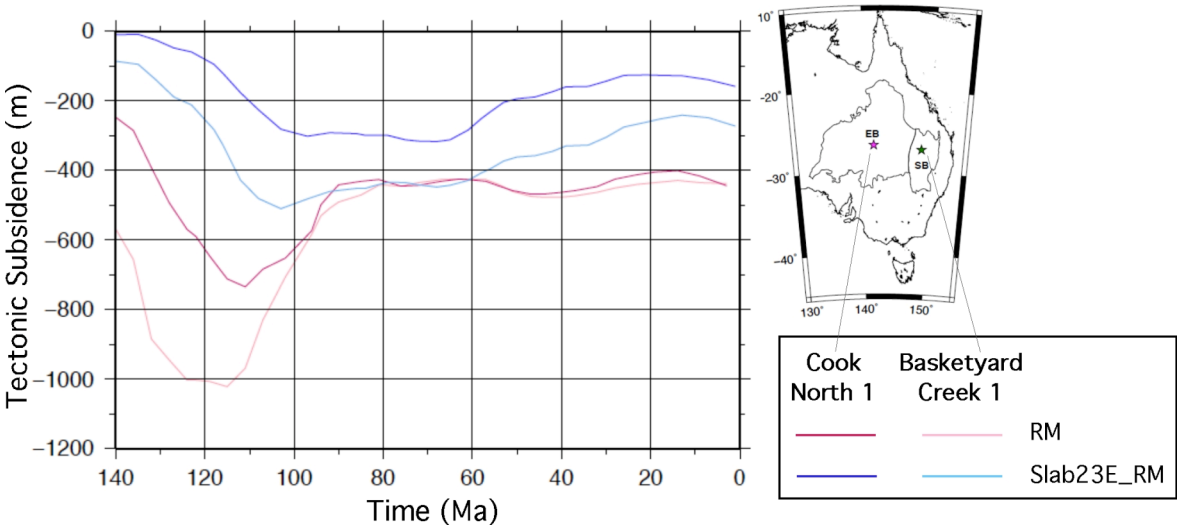

Figure 34. Model subsidence curves for Cook North 1 in the Eromanga Basin and Basketyard Creek 1 in the Surat Basin, for the reference model (model RM – pink) and model Slab23E_RM (blue) (left), and location map (right). Although the timing of increased subsidence varies between the models, there is no change from E-W within each model (pink and blue curves steepen at the same time, respectively). EB – Eromanga Basin and SB – Surat Basin.

The present-day dynamic topography signal of the Australian region is dominated by active subduction to the north and east of Australia. However, the effects of Cretaceous negative dynamic topography are not completely diminished by the present-day; represented by the light blue band of negative topography covering Eastern Australia in Figure 35. These results suggest that, although dynamic topography is transient, its effect can persist for tens of millions of years. This further highlights that attributing absolute dynamic topography to one event can be highly complex as a negative signal can have multiple sources (of varying ages) in regions of long-lived subduction.

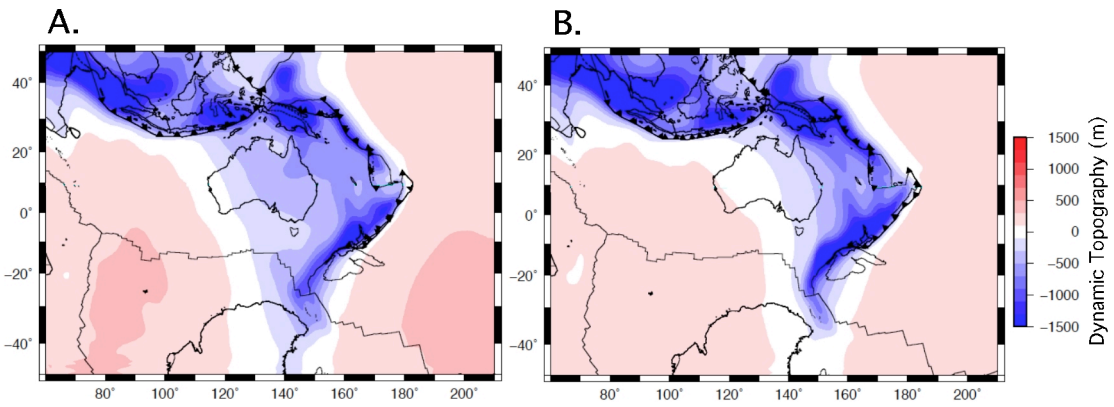

Figure 35. Predicted present-day dynamic topography signal for (A) the reference model (model RM) and (B) the reference model with subduction shifted east (model Slab23E_RM). A larger portion of the Australian continent is affected by Cretaceous negative dynamic topography at present-day for model RM.

5.3 Tectonic Subsidence History of the Eromanga-Surat Basin System

Tectonic subsidence histories were calculated for 42 wells from the Eromanga and Surat basins, using the backstripping methodology outlined in Figure 18 (see Appendix 2). Although this study is primarily concerned with Cretaceous aged subsidence and its links to mantle convection, a brief analysis of pre-Cretaceous subsidence is essential for identifying Cretaceous trends. That is, without understanding the earlier history of subsidence in the basins, it would be difficult to isolate time-dependent changes in one portion of the data.

5.3.1 Pre-Cretaceous Subsidence

Several wells located in the central regions of each basin preserve Late Permian and Triassic sediments from the older underlying basins (Figure 36). These wells record a period of very rapid subsidence of 8-13 m/Myr that persists until the Mid-Triassic. Subsidence at this time has been attributed to lithospheric flexure resulting from foreland basin loading, and also follows a phase of thermal relaxation that commenced in the Early Permian in response to mechanical extension (Korsch and Totterdell, 2009; Waschbusch et al., 2009).

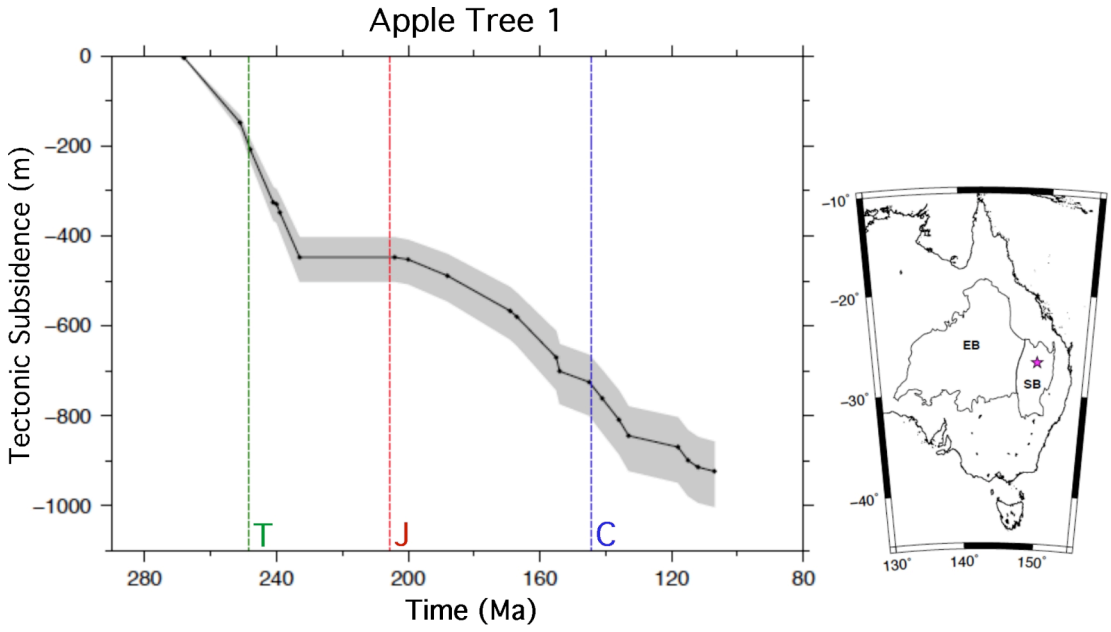

Figure 36. Tectonic subsidence curve for Apple Tree 1 in the Surat Basin (left), and location map (right). The steepness of the curve during the Permian and Early Triassic

illustrates rapid subsidence. Dashed lines mark the beginning of the Triassic (green), Jurassic (red) and Cretaceous (blue). Pink star marks the location of the well site. EB – Eromanga Basin; SB – Surat Basin.

At approximately 230 Ma, following rapid flexure-induced subsidence, a 30-40 Myr phase of erosion is evident in the well data; depicted by flattening of the tectonic subsidence curves (Figures 36 and 37). This period of erosion dominated eastern Australia (Senior et al., 1978) and has been noted in previous tectonic subsidence analyses of the eastern Australian basins (Gallagher, 1990; Korsch and Totterdell, 2009).

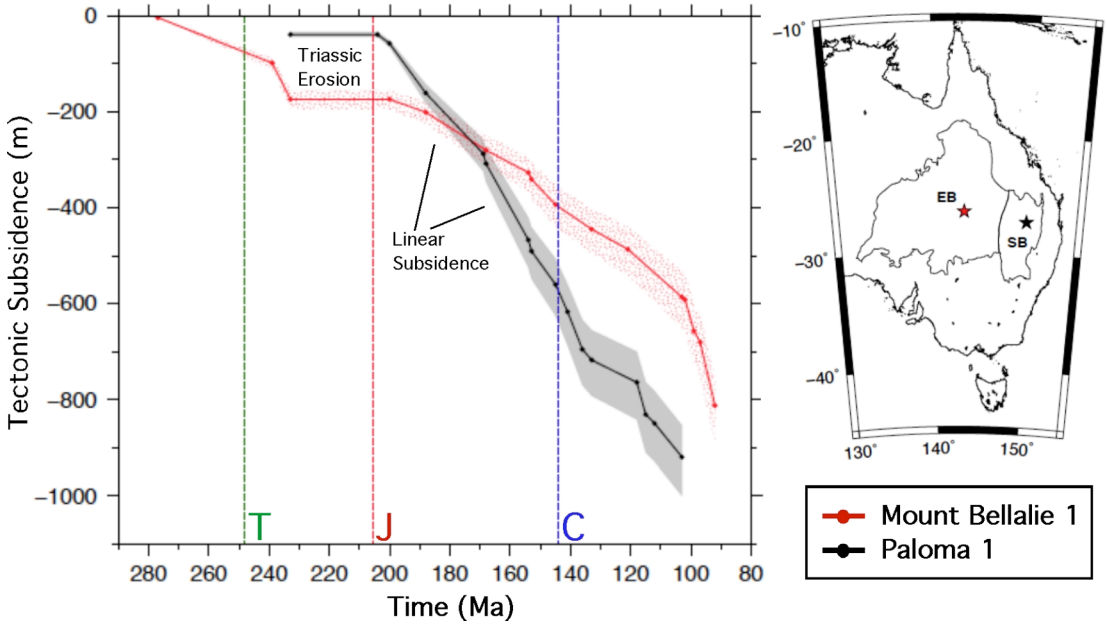

Figure 37. Tectonic subsidence curves for Mount Bellalie 1 and Paloma 1 (left), and location map (right). Mid-Late Triassic erosion is represented by the flattening of the subsidence curves. This is followed by linear subsidence in the Jurassic. Dashed lines mark the beginning of the Triassic (green), Jurassic (red) and Cretaceous (blue). Red and black stars mark the locations of Mount Bellalie 1 and Paloma 1, respectively. EB – Eromanga Basin; SB – Surat Basin.

Following Mid-Late Triassic erosion, subsidence re-commenced in the Eromanga and Surat basins in the Jurassic. Well data show linear subsidence that increases in an easterly direction (as previously concluded by Gallagher, 1990) (Figure 37). Maximum subsidence occurs in the central to central-eastern sections of the Surat Basin, 10 m/Myr (Arlington 1), and decreases to a minimum of 2 m/Myr (Eromanga 1) in the westerly wells of the Eromanga Basin (excluding Cook North 1, the most western well). Subsidence rates are on average 2-3 times higher in the most easterly wells compared to the most westerly

located wells (Gallagher, 1990). This increase in subsidence in the east appears to be a progressive regional trend, with no distinct subsidence jump seen in the wells around the boundary between the two basins. Waschbush et al. (2009) attribute Jurassic subsidence to tilting from dynamic corner flow (Mitrovica et al., 1989). The linearity of the curves argues against post-rift thermal decay, which is generally expressed as an exponential, concave down curve, and there is an absence of extensional faulting through Jurassic sediments in the basins precluding an extensional cause.

5.3.2 Cretaceous Subsidence

The linear subsidence trend that characterised the Jurassic continues until the Early Cretaceous. At ~120 Ma there is a basin wide increase in the rate of subsidence, observed as a steepening of the tectonic subsidence curves (Figure 38). This increase is slightly more pronounced in the east compared to the west. However, an absence of sampling between ~120-100 Ma and calculation errors (grey error polygons on graph) in wells west of 144ºE makes it difficult to assess the exact magnitude of subsidence in these wells at this time.

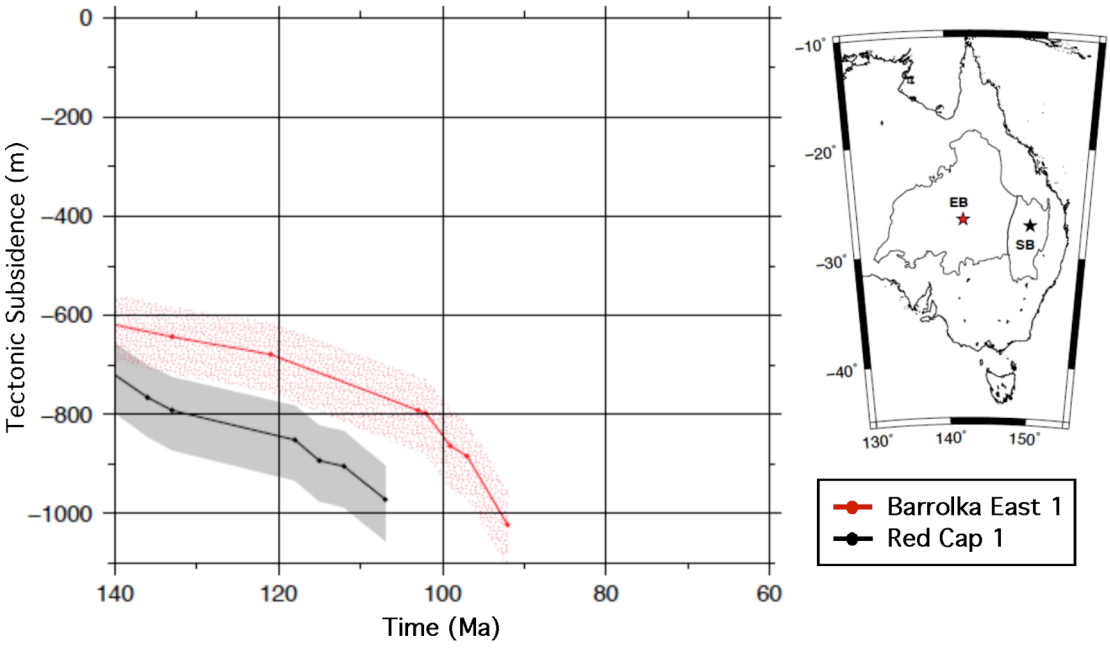

Figure 38. Cretaceous tectonic subsidence curves for Barrolka East 1 and Red Cap 1 (left), and location map (right). Steepening of the curves at 120 Ma represents an increase in subsidence, this event it more pronounced for Red Cap 1. Red and black stars mark the locations of Barrolka East 1 and Red Cap 1, respectively. EB – Eromanga Basin; SB – Surat Basin.

The rapid increase in subsidence is delayed by up to 20 Myr in the most westerly wells. For example, it is not until ~100 Ma that subsidence rates in the Eromanaga Basin exhibit a dramatic increase. Rates of subsidence at this time generally exceed those observed in wells from the Surat Basin 20 Myr earlier. The youngest sediments preserved in the Surat Basin date to approximately 103 Ma, making it impossible to determine how far east this second episode of subsidence extended. It is interesting to note too, that both phases of increased subsidence (~120 Ma and ~100 Ma) are simultaneously preserved in two wells from the eastern Eromanga Basin (Quilpie 1 and Quilberry 1 – Figure 39). These wells are located approximately mid-way along the E-W transect, just west of the boundary between the two basins, highlighting continuity of these subsidence events along the transect.

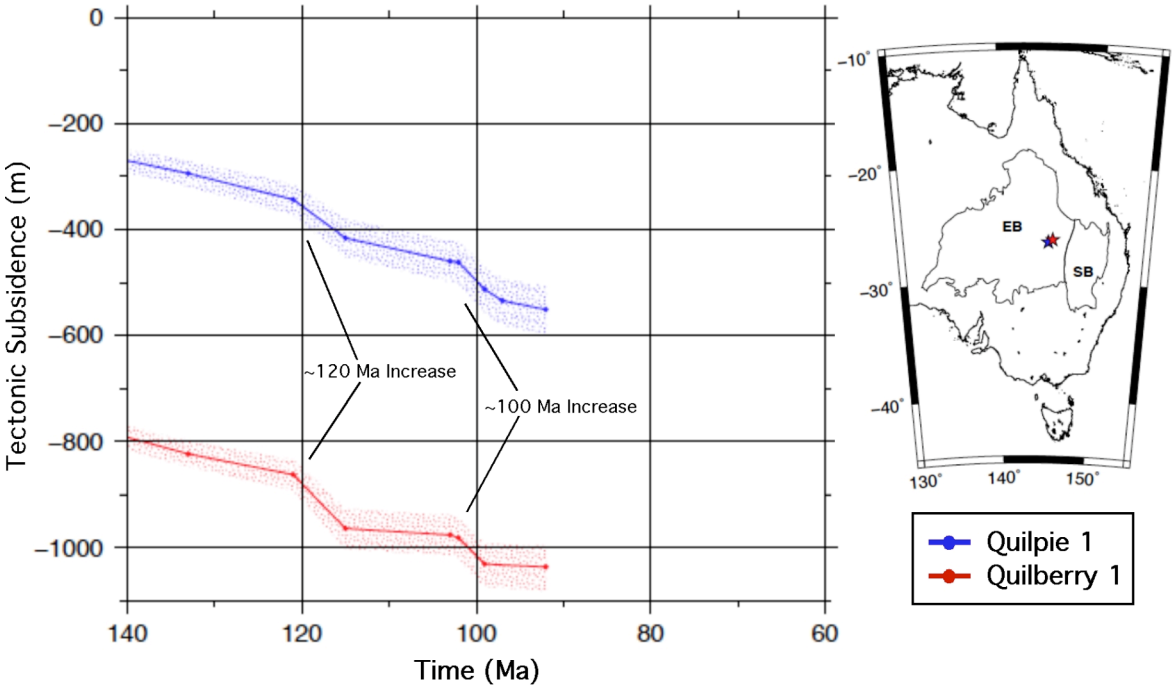

Figure 39. Cretaceous tectonic subsidence curves for Quilpie 1 and Quilberry 1 (left), and location map (right). Subsidence histories for these wells record increasing subsidence at ~120 Ma and ~100 Ma. The increase at 120 Ma is more pronounced than for wells further west (for example, Barrolka East 1 – Figure 38), although this may be an artefact of sparse sampling. Blue and red stars mark the locations of Quilpie 1 and Quilberry 1, respectively. EB – Eromanga Basin; SB – Surat Basin.

5.3.3 General Subsidence Trends

Tectonic subsidence patterns in the Eromanga and Surat basins exhibit a dominant E-W trend. Since the formation of the basins initiated in the Early Jurassic, following extensive Late Triassic erosion, subsidence rates have been higher in the east compared to the west.

Early Cretaceous episodes of rapid subsidence also occurred in the east earlier than in the west, implying that the driving mechanism had an easterly origin and its influence consequently propagated westward. These results are not surprising considering that eastern Australia was bounded by a convergent margin during the Mesozoic, and that dynamic platform tilting, mechanical extension, thermal relaxation and foreland basin loading have all been invoked to account for Permian-Triassic Subsidence in older eastern Australian basins in the same region (Korsch and Totterdell, 2009; Waschbusch et al., 2009).

5.4 Comparison of Modelled Subsidence to Tectonic Subsidence Inferred from Borehole Analyses

5.4.1 Timing of Accelerated Subsidence

When subduction is modelled as being located adjacent to the reconstructed margin at 140 Ma, modelled Cretaceous subsidence accelerates at approximately 140 Ma, 20 Myr earlier than observed in the borehole record (Figure 40). Shifting the subduction zone 23º east reconciles this timing mismatch (Figure 41). Although the magnitude and rate of subsidence vary between the models with the subduction zone initially shifted east, the rate of subsidence consistently increases at ~120 Ma along the E-W transect, in agreement with the local geology. However, tectonic subsidence analyses of borehole data from the Eromanga Basin also reveal a prominent increase in subsidence at ~100 Ma, following the more gentle acceleration at 120 Ma. Neither series of *CitcomS* models capture this second pulse of subsidence. Rather the Slab23E series of models predicts the initiation of uplift at this time. See Appendix 4 for the complete set of figures showing modelled and tectonic subsidence.

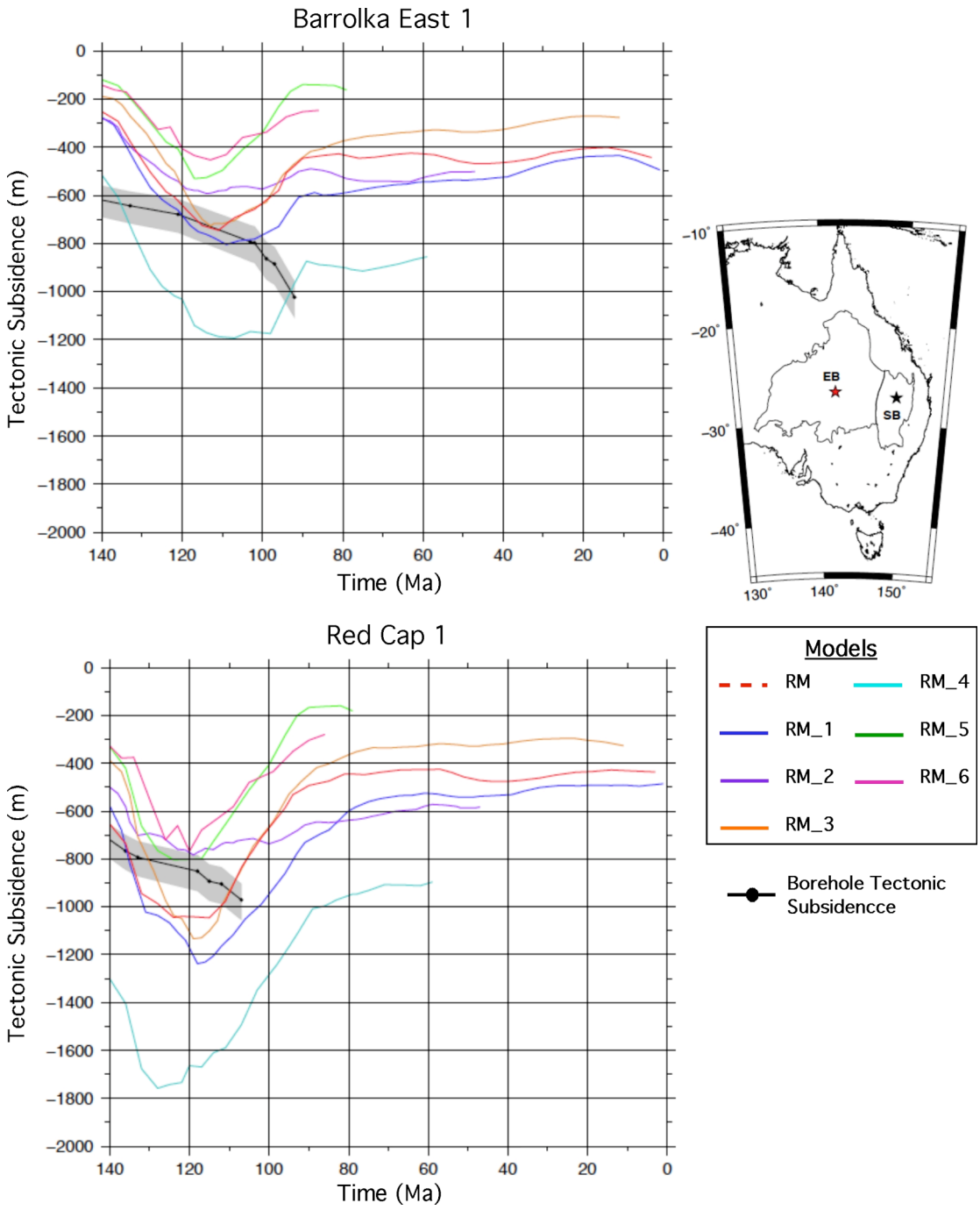

Figure 40. Modelled (coloured curves) and 'observed' tectonic subsidence (black line with grey error polygon) for Barrolka East 1 and Red Cap 1 during the Cretaceous. Models are from the RM model series (see Table 7 for model parameters). Red star-Barrolka East 1; black star-Red Cap 1; EB – Eromanga Basin; SB – Surat Basin. Note: Not all *CitcomS* models were solved to present-day and this is why the coloured curves stop at different ages.

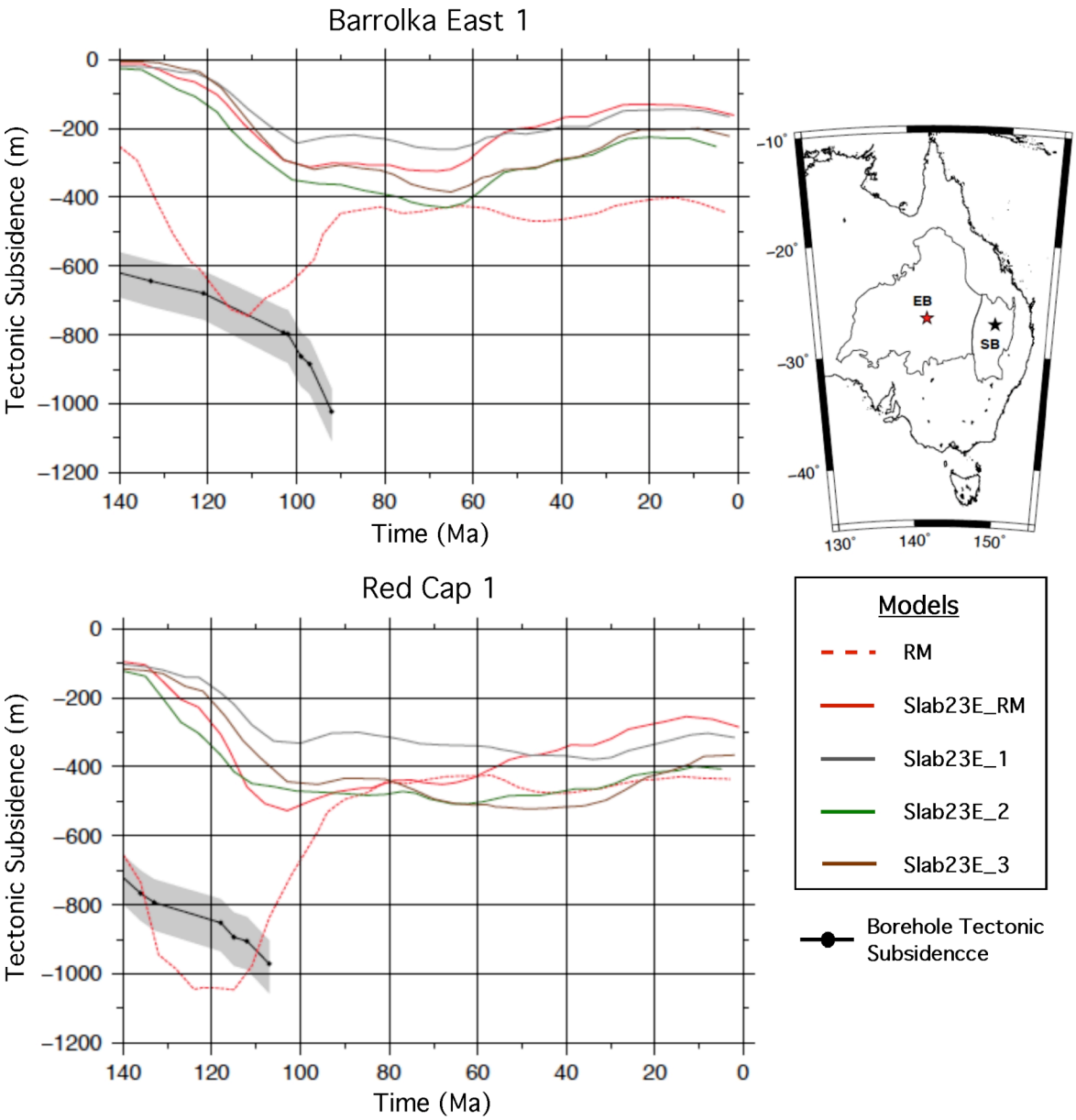

Figure 41. Modelled (coloured curves) and 'observed' tectonic subsidence (black line with grey error polygon) for Barrolka East 1 and Red Cap 1 during the Cretaceous. Models are from the Slab23E model series (see Table 8 for model parameters). Red star – Barrolka East 1; black star – Red Cap 1; EB – Eromanga Basin; SB – Surat Basin. Note: Not all *CitcomS* models were solved to present-day and this is why the coloured curves stop at different ages.

It should be noted that when comparing the observed (borehole derived) and predicted (modelled) subsidence curves, the initial depth of the surface is relative. The *CitcomS* models are not initialised with a 'memory', that is, the initial topography (140 Ma) does not capture any pre-existing dynamic signals, nor is palaeo-topography incorporated in its calculation. Rather the dynamic topography for the first timestep is computed with respect to an elevation of 0 m. Also, the well data are backstripped with respect to a datum of 0 m

at the beginning of the subsidence period being modelled. As the two data sets reveal relative subsidence with respect to different datums, it is therefore the timing and rate of subsidence that are important, rather than the positions of the subsidence curves along the y-axis.

5.4.2 Rate of Accelerated Subsidence

Mantle material properties influence how rapidly a basin subsides. Comparing the modelled subsidence curves and borehole data reveals that, although the timing of increased subsidence at 120 Ma can be consistently reproduced when subduction is shifted east, the rate of subsidence preceding and following this time varies according to the initial mantle rheological parameters. The tectonic subsidence curves for 5 boreholes (roughly evenly spaced along the E-W transect) have been shifted along the y-axis of the tectonic subsidence plots. This was carried out to equate their initial depths to those of two models from the 'Slab23E' model series at the same locations (Figure 42). This reveals how well the models reproduce subsidence rates from east to west in the basins.

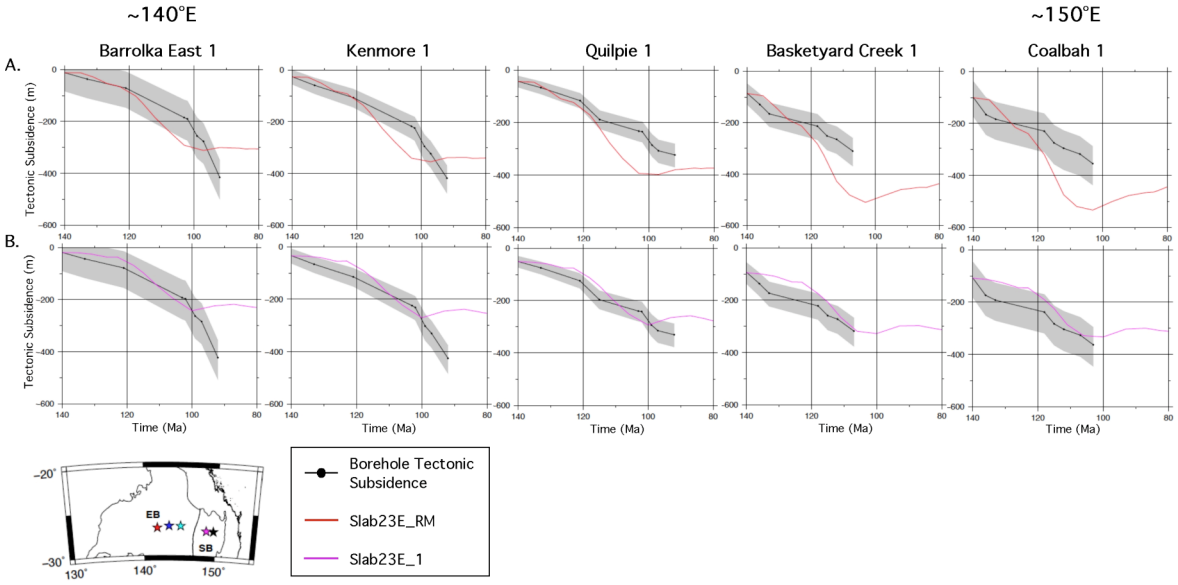

Figure 42. Modelled and 'observed' tectonic subsidence for 5 well locations during the Cretaceous. 'Observed' tectonic subsidence curves have been shifted along the y-axis to allow for a comparison between the gradients of the curves, and therefore the rates of subsidence. (A) Model Slab23E_RM and (B) model Slab23E_1 (see Table 8 for model parameters). Stars show the well locations: red – Barrolka East 1, blue – Kenmore 1, cyan – Quilpie 1, magenta – Basketyard Creek 1, black – Coalbah 1. EB – Eromanga Basin; SB – Surat Basin.

The models with subduction shifted 23º east of the reconstructed continental margin produce a good match for Early Cretaceous subsidence between 140-120 Ma in the Eromanga Basin. However, at this time further east in the Surat Basin, there is a mismatch between the observed and predicted patterns of subsidence. Borehole data in the east reflect the ending of linear Jurassic subsidence (see also Figure 37), represented as the steep curve between 140 and ~135 Ma, followed by ~15 Myr of very slow subsidence before accelerated subsidence at 120 Ma. However, model Slab23E_RM predicts the opposite, with 5 Myr of minimal subsidence followed by 15 Myr of increased subsidence. After 120 Ma the surface subsides too rapidly along the entire transect; as inferred from the modelled subsidence curve being much steeper than the borehole tectonic subsidence curve.

In order to improve the modelled rates of subsidence in the basins, additional models with subduction shifted east were tested (Figure 41). Increasing viscosities in the upper mantle, transition zone and lower mantle, while maintaining the same viscosity ratio as model Slab23E_RM (Table 8), produces a better fit between the observed and predicted rates of subsidence from 140 Ma. From Figure 42 it can be seen that the shapes of the slopes are highly comparable.

The *CitcomS* models all capture the general trend of more rapid subsidence in the east.

5.5 Comparison of Modelled Mantle Structure to Seismic Tomography

S- and P-wave seismic tomography models for the southwest Pacific (Ritsema et al., 1999; Grand, 2002; Montelli et al., 2006; Simmons et al., 2007; Li et al., 2008) reveal high velocity material extending from the upper mantle through the transition zone to the core-mantle boundary beneath eastern Australia (Figure 43). There is also a volume of more shallowly penetrating high velocity material beneath the South Fiji Basin, at approximately 180ºE (just west of the Tonga-Kermadec Trench), that extends to ~1200 km depth (non-dimensionalised depth of 0.8). It is inferred that cold subducted slabs produce these anomalous velocity signatures, due to the relationship between temperature and the speed of elastic waves through the mantle. Hence seismic tomography can show the locations of subducted slabs.

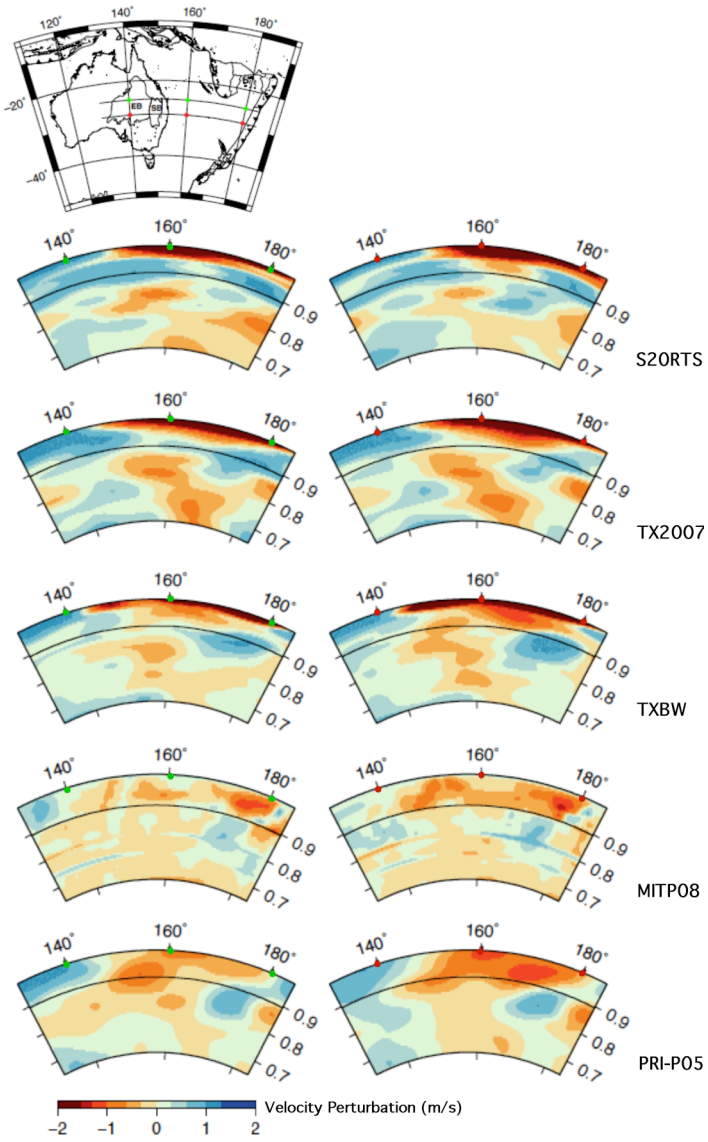

Figure 43. Location map showing profiles of seismic tomography at 25ºS and 29ºS (top), and seismic tomography cross-sections to the core-mantle boundary (bottom). Anomalously fast velocities (blue areas) are inferred to represent cold regions of the mantle, and anomalously slow velocities (red areas) are inferred to represent hot regions. S-wave models: S20RTS (Ritsema et al., 1999), TX2007 (Simmons et al., 2007), TXBW (Grand 2002). P-wave models: MITP08 (Li et al., 2008) and PRI-P05 (Montelli et al., 2006).

When Cretaceous subduction is modelled as being located adjacent to the palaeo-continental margin the resultant present-day temperature structure of the mantle shows no cold material in the lower mantle beneath eastern Australia (Figure 44). The slab is confined to the upper mantle where is appears to be laid out flat along the 660 km boundary (black line at non-dimensionalised depth of ~0.9), with limited penetration of the lower mantle. This presents a significant mismatch with geological data in this region.

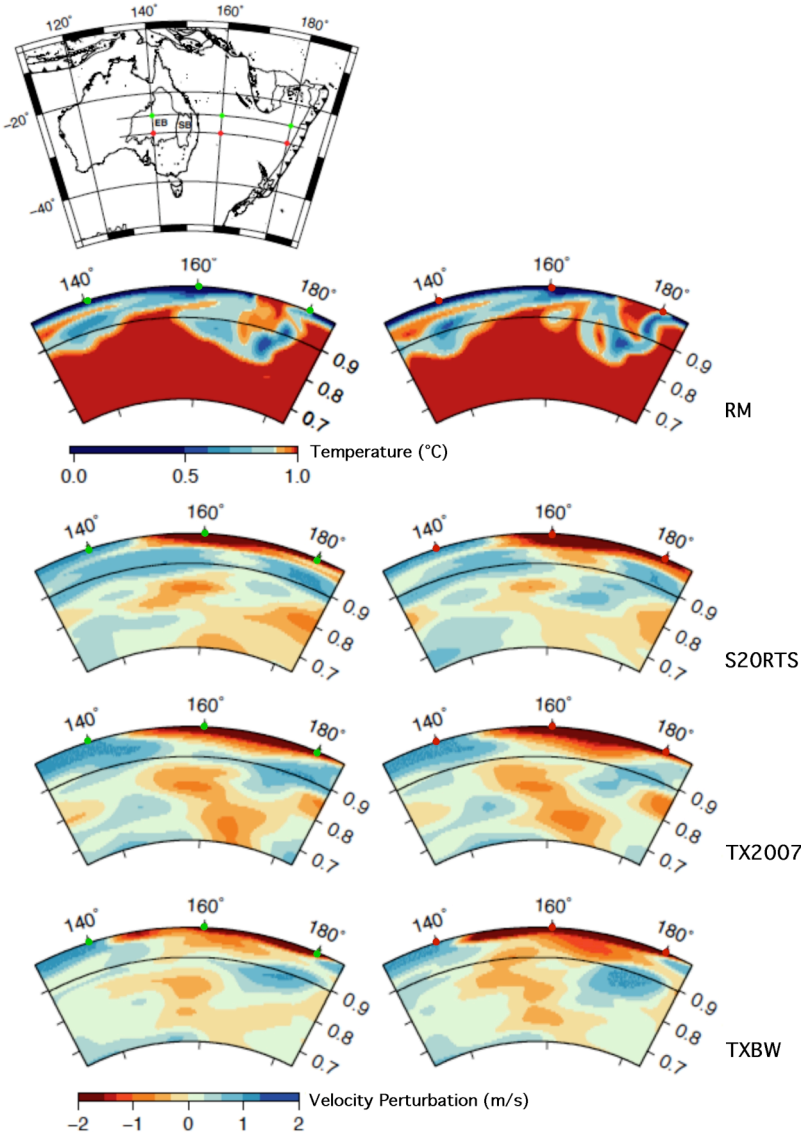

Figure 44. Location map showing profiles of *CitcomS* modelled temperature and seismic tomography at 25ºS and 29ºS (top), and temperature and S-wave seismic tomography cross-sections to the core-mantle boundary (bottom). Temperature cross-sections for the reference model (model RM) reveal cold slab material penetrating to ~1200 km, with the majority in the upper mantle and transition zone. This presents a partial mismatch with seismic tomography, which reveals velocity perturbations extending to the core-mantle boundary beneath eastern Australia. S-wave models: S20RTS (Ritsema et al., 1999), TX2007 (Simmons et al., 2007), TXBW (Grand 2002).

Simulating subduction 23º east of eastern Australia allows the mantle to evolve such that by present-day slab material extends from the surface to the core-mantle boundary beneath eastern Australia (Figure 45). Thus the modelled present-day temperature structure is in close agreement to seismic tomography. The majority of slab material is confined to the lower mantle, except where the slab is attached to the surface at ~150ºE. The current *CitcomS* models do not retain as much cold material in the upper mantle, as is inferred

from the seismic tomography models (Figure 46 – blue smear above 660 km between 130-160ºE). Increasing mantle viscosities resulted in a larger volume of slab material being retained higher up in the mantle, however the models were unsuccessful in producing the distinct band of inferred cold material in the upper 660 km.

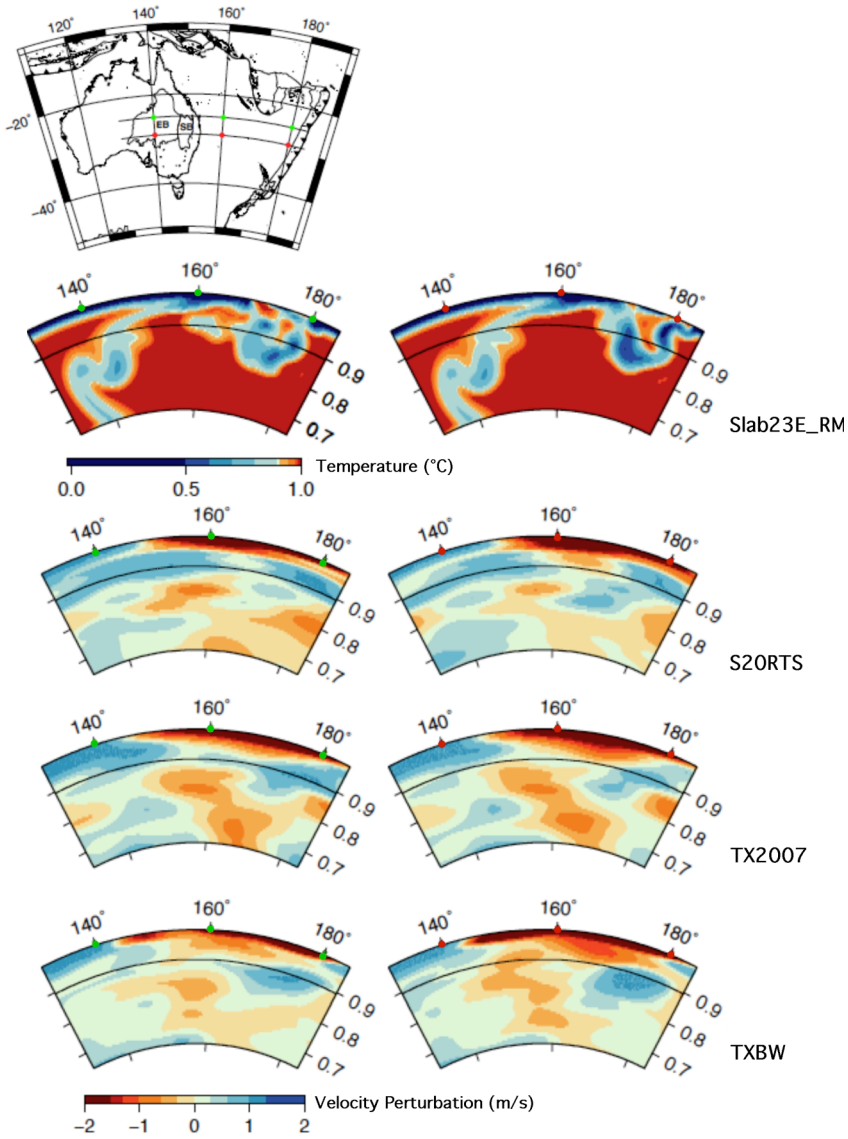

Figure 45. Location map showing profiles of *CitcomS* modelled temperature and seismic tomography at 25ºS and 29ºS (top), and temperature and S-wave seismic tomography cross-sections to the core-mantle boundary (bottom). Temperature cross-sections for the reference model with subduction shifted east (model Slab23E_RM) (top two profiles) reveal a deformed slab penetrating to the core-mantle boundary beneath eastern Australia, with a majority of cold material in the lower mantle between ~700-1600 km depth. A second mass of cold slab material penetrate to ~1200km west of the Tonga-Kermadec Trench. These results are in good spatial agreement with the underlying S-wave seismic tomography images. S-wave models: S20RTS (Ritsema et al., 1999), TX2007 (Simmons et al., 2007), TXBW (Grand, 2002).

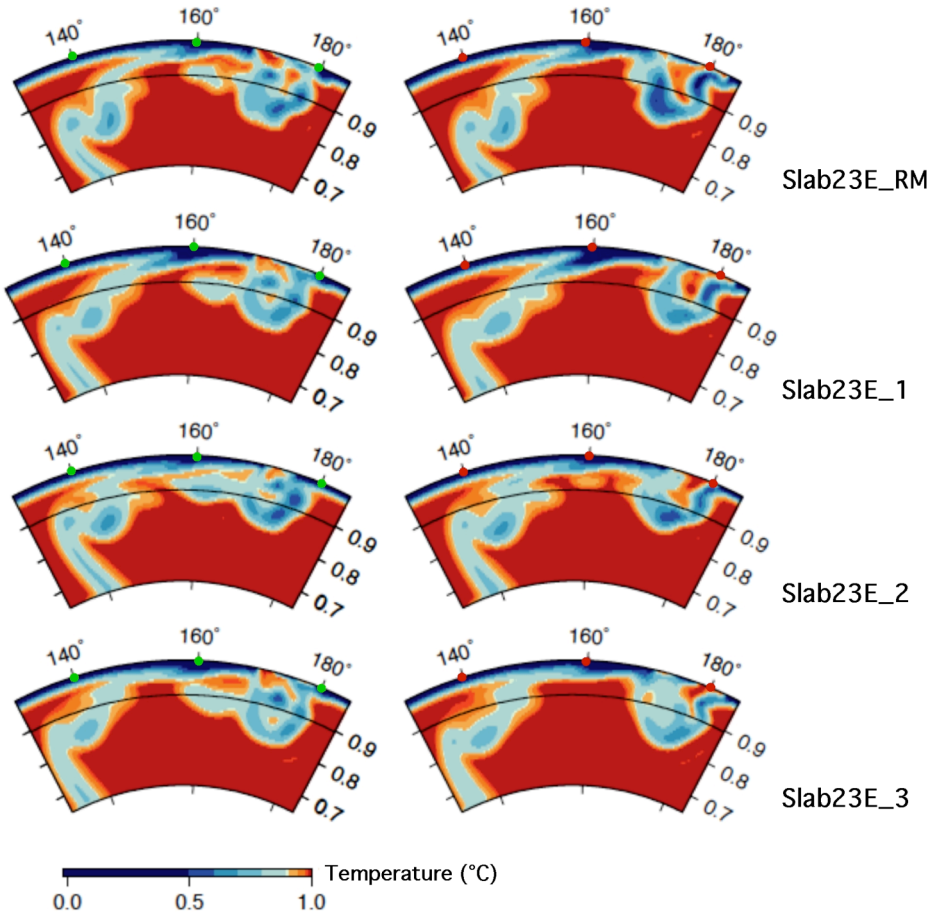

Figure 46. Temperature profiles for models with subduction shifted east (see Table 8 for model parameters). General trends are consistent between models, with the major difference being the amount of slab material sitting near the 660 km boundary beneath eastern Australia. See Figure 45 above for profile locations.

All *CitcomS* models produce a second mass of cold material in the upper 1200 km of the mantle between 160-180ºE. This is in excellent agreement with seismic tomography. The lateral extent of cold material in the upper mantle is also slightly larger further north, again consistent with seismic tomography (cross-sections with green dots in Figure 20).

6 Discussion

6.1 Cretaceous Dynamic Topography in Eastern Australia

Geodynamic modelling of the Australian region since 140 Ma predicts surface vertical motion in eastern Australia consistent with geological data. As the Australian plate moves in an eastward direction between 140 Ma and ~100 Ma, it overrides subducted oceanic lithosphere originating from subduction between Eastern Gondwanaland and the Phoenix plate, part of the palaeo-Pacific Ocean (Panthalassa). As the subducting slab descends through the upper mantle it viscously drags down the overlying crust, creating a broad region of negative dynamic topography in eastern Australia. This zone of deflection expands westward towards the continental interior between 140-100 Ma, covering the entire western half of the continent by 100 Ma. These findings are in agreement with Gurnis et al. (1998), Waschbusch et al. (2009) and Korsch and Totterdell (2009) who have previously attributed Cretaceous subsidence in eastern Australian basins to mantle convection processes.

The geodynamic models with Cretaceous subduction 23º east of the reconstructed margin result in accelerated subsidence in the Eromanga and Surat basins at 120 Ma, in agreement with borehole data along an E-W transect ~27ºS, between ~141ºE and 152ºE. This coincides with a 4.5 cm/yr increase in the eastward velocity of the Australian plate (Figure 47), and as a result the overriding plate more rapidly moves across slab material that is descending higher up in the mantle. The increase in the rate of subsidence occurs simultaneously in the two basins but at a slightly higher rate in the east, consistent with geological data. Comparing the slopes of the modelled and geologically predicted subsidence curves reveals a high degree of similarity, highlighting that both timing and rate of subsidence can be reproduced using geodynamic models.

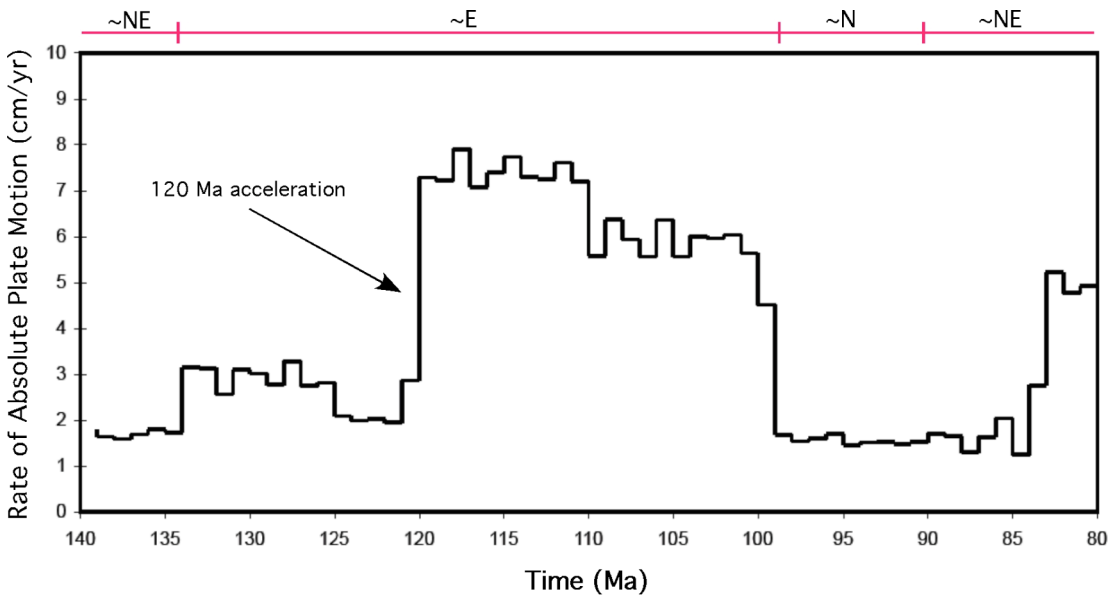

Figure 47. Rate of absolute motion of the Australian plate from 140-80 Ma; averaging interval is 1 Myr. The approximate direction of plate movement is labelled for different intervals during this timeframe (annotated pink line above graph).

Dynamic topography is a transient phenomenon and as a result its geological effects are reversible. Dynamic subsidence creates accommodation space and can allow more than 1km of sediment to be deposited in basin depressions. However, when the causal anomaly is removed, the surface rebounds and widespread erosion occurs. Reversals of negative dynamic topography, as well as transitions to positive dynamic topography are expressed as unconformities in the stratigraphic record (Burgess et al., 1997).

Uplift of eastern Australia occurred in response to cessation of subduction, related to major changes in absolute plate motion of the Australian plate. It resulted in basin inversion and erosion of up to ~3 km of sediments from the Eromanga and Surat basins in the Late Cretaceous and Early Tertiary (Gallagher et al., 1994; Raza et al., 2009). This transition from subsidence to uplift removed a larger volume of sediments from the Surat basin (Gallagher et el., 1994). This is not surprising, as more accommodation space can be created towards cratonic margins (near the subduction zone), resulting in higher erosion rates when the surface rebounds (Burgess et al., 1997). As a result, younger sediments are preserved in the Eromanga Basin (~90 Ma), compared to the Surat Basin (~100 Ma). This trend is similar to the easterly increase in ages of outcrops observed in North America, resulting from the reversal of dynamic tilting of the eastern part of the continent caused by Iapetus subduction in the Late Palaeozoic (Burgess et al., 1997). The main limitation of the current models is that they do not capture the ~100 Ma episode of rapid subsidence in

the Eromanga Basin following gentle acceleration at 120 Ma. The models prematurely simulate uplift at this time, which continues until present-day.

This 100Ma phase of rapid subsidence in the Eromanga Basin may have been caused by a mantle avalanche, whereby a build up of slab material in the transition zone penetrates the lower mantle in a "dramatic downwelling" event (Pysklywec and Mitrovica, 1997). Pysklywec and Mitrovica (1997) predict that mantle avalanches can cause up to 2.5 km of subsidence. Although these conditions are not currently simulated, model results coupled with trends in the geological record and seismic tomography, make a mantle avalanche a plausible scenario.

While the location of the subduction zone at 140 Ma clearly controls the timing of subsidence acceleration, extensive model experimentation has revealed that mantle material parameters exert a major control over the magnitude of subsidence. In initial models with subduction adjacent to the continent (the RM model series), the magnitude of subsidence is highly variable depending on the mantle material parameters. However, consistent between all these models is an immediate (~140-135 Ma) stalling of the slab in the transition zone for approximately 20-40 Myr (depending upon the mantle material parameters), before it begins to penetrate the lower mantle. A more resistive mantle traps a larger volume of slab material in the transition zone, for a longer period of time, compared to a less resistive mantle (see Figure 27 for a qualitative assessment of which models were more, or less, resistive to the descent of the slab). When subduction is shifted east (the 'Slab23E' model series) and a pre-existing slab is initialised down to the core-mantle boundary, these effects are reduced as the slab easily descends through the transition zone; it does not appear to be hindered by increasing viscosity until the mid lower mantle. Therefore, these latter models are not currently simulating the conditions required for a mantle avalanche.

In contrast to the current geodynamic models, S- and P-wave seismic tomography models infer a larger volume of slab material in the transition zone and upper mantle beneath eastern Australia. Although subduction ends in the Cretaceous, the slab has still not fully penetrated the lower mantle by present-day. Slowing down slab descent, for example by increasing the resistance of the lower mantle, in future modelling will reconcile this mismatch. Tomography models further support the proposition that during the Cretaceous slab material stalled in the transition zone beneath eastern Australia. The key to recreating

the 100 Ma subsidence event in the Eromanga Basin is most likely in further refinement of the initial mantle rheological parameters to accentuate build up of slab material in the transition zone.

By 140 Ma, Australia as a part of Eastern Gondwanaland had been moving in a ~E-SE direction at least since the Late Jurassic (Torsvik et al., 2008). As a result older slab material is already emplaced in, and descending through, the mantle beneath Australia by the Cretaceous, and may be the cause of Jurassic subsidence. This also implies that in the Cretaceous the slab may not have extended to the core-mantle boundary (as set up as the initial condition in the preferred models), rather it may have been dragged out for thousands of kilometres across the upper lower mantle and transition zone. A shorter slab is likely to reduce the downward pull on the slab and therefore provide less of a driving force through the transition zone, allowing it to be laid out flat above the 660 km phase boundary as the overlying plate moves east.

During the Cretaceous, the age of oceanic crust being subducted progressively decreases as the subduction hinge rolls back towards the fossil Phoenix-Pacific spreading ridge. As oceanic lithosphere ages it cools, thickens and subsides until it reaches equilibrium (Sclater et al., 1980). Younger lithosphere is weaker and able to bend more easily than older more rigid lithosphere (e.g. Morra et al., 2006; Goes et al., 2008). As progressively younger lithosphere entered the mantle in the Mid-Cretaceous, it may have sunk more sluggishly due its higher buoyancy, but at a steeper angle due to a greater propensity for bending at the subduction hinge. This process may have accentuated the trapping of subducted crust in the transition zone, leading to a build up of material required for the proposed avalanche. Subduction of younger crust may also have contributed to the initiation of post-subduction uplift, as descending slab material would have been inducing less drag on the overlying lithosphere compared to earlier times when older lithosphere was being actively subducted. Approach of the Phoenix-Pacific spreading ridge and the subduction of relatively young crust may also have played a role in the cessation of subduction.

The above arguments, coupled with a lack of evidence for lithospheric extension in the Eromanga Basin (and Surat Basin), strongly suggests that the cause of the 100Ma accelerated subsidence event in eastern Australia is related to mantle dynamics. However, contrary to the conclusions of Waschbusch et al. (2009) these results do not necessarily support dynamic tilting from mantle corner flow (Mitrovica et al., 1989) as the sole cause

of Cretaceous dynamic subsidence. Uplift initiated in the Surat Basin approximately 100-80 Ma, coinciding with an episode of accelerated subsidence in the Eromanga Basin. If subsidence in the Eromanga Basin at 100 Ma was due to dynamic tilting, it is counterintuitive that the rate of subsidence would accelerate at the same time as uplift further east. Current geodynamic models suggest that subsidence is due to a combination of dynamic effects, that is, arc-corner flow induced tilting and a Late Cretaceous mantle avalanche further west. Although mantle avalanches are rare events (Pysklywec and Mitrovica, 1998), a sudden breakthrough of slab material trapped in the transition zone may have induced more rapid subsidence in the Eromanga Basin at 100 Ma, than is observed earlier in the geological record. Analysing tectonic subsidence from boreholes further west in the Eromanga Basin will help determine the westward extent of this 100 Ma accelerated subsidence event in future investigations.

Despite the above limitation of the current models, the present-day modelled mantle temperature structure beneath Australia and the southwest Pacific fits well with S- and P-wave seismic tomography models (Ritsema et al., 1999; Simmons et al., 2007; Grand, 2002; Li et al., 2008; Montelli et al., 2006). Slab material penetrates to the core mantle boundary beneath eastern Australia and a second mass of cold material extends to ~1200 km depth beneath the South Fiji Basin (west of the Tonga-Kermadec Trench) ~165-180ºE, in excellent agreement with tomography data. This latter observation highlights the robustness of the model, in that it successfully predicts geology beyond the region of investigation.

6.2 Constraining the Location of Cretaceous Aged Subduction East of Australia

Our assimilation of geological observations with geodynamic models strongly suggests that the Cretaceous subduction zone that paralleled eastern Australia was located up to ~1000 km offshore, ~23º east of the reconstructed continental margin. A combination of geodynamic modelling, tectonic subsidence analysis and seismic tomography analysis precludes subduction further west. In simulations with subduction adjacent to the continental margin, subsidence in the Eromanga and Surat basins accelerates 20 Myr earlier than inferred from well data. This time lag is consistently observed for a variety of mantle conditions, including different mantle viscosities, Rayleigh numbers and thermal conditions. A mismatch between the modelled present-day mantle temperature structure

and whole-mantle seismic tomography also arises when subduction is too far west. While S- and P-wave seismic tomography reveals anomalously fast material in the lower mantle beneath eastern Australia, inferred to represent slab material, these models do not predict slab material beneath ~900 km in regions east of longitude ~130ºE (this is west of the western boundary of the Eromanga Basin).

Eastern Australia has had a very active tectonic history. A convergent margin paralleled eastern Gondwanaland from at least the Carboniferous, with evidence for subduction related magmatism preserved in the New England Fold Belt (Leitch, 1975; McPhie, 1985). It is known that throughout this time the Australian plate (as a part of eastern Gondwanaland) and the subduction zone were highly mobile, yet the relative distance of the subduction zone from the continental margin has remained enigmatic for much of the Mesozoic.

Despite being further back in time, the Palaeozoic history of subduction has been well constrained by a combination of structural and geochemical investigations. The Late Palaeozoic to early Triassic subduction zone was highly mobile (Jenkins et al., 2002). According to Jenkins et al. (2002), during the Early Carboniferous the subduction zone remained stationary at the continental margin, and fuelled volcanic eruptions of the New England Fold Belt, a volcanic arc at this time. This was followed by a phase of subduction zone retreat in the Late Carboniferous-Early Permian, inferred from lithospheric extension and back-arc magmatism. In the Late Permian the subduction zone began to advance back towards the palaeo-coastline, expressed by compressional tectonics that initiated the Hunter-Bowen Orogeny and foreland basin loading, and re-established a magmatic arc. This advancement continued until the Early Triassic. By the Late Triassic, extension had recommenced in eastern Australia, forming elongate basins. Holcombe et al. (1997) speculate that this extension may have been driven by slab rollback and oceanward migration of the subduction hinge.

These Palaeozoic and Early Triassic trends support a distal subduction zone during the Cretaceous. Although it has been suggested that the Cretaceous margin of Australia was analogous to the present-day Chilean margin, with subduction adjacent to the coast (Veevers, 1984; Veevers, 2000), the current results combined with indicators from the geologic record suggest that this is unlikely. During the Cretaceous there is a lack of evidence for subduction zone magmatism in eastern Australia, yet during the

Carboniferous and Late Permian, when subduction is inferred to have been adjacent to the coast, there is abundant geological evidence for arc volcanism and convergent margin tectonism such as foreland basin loading and orogeny. Although there are volcanogenic sediments preserved in the Eromanga and Surat basins, there is strong evidence to suggest that they have an extensional origin. Ewart et al. (1992) and Bryan et al. (1997) describe a large-scale extensional volcanic event in the Whitsundays Volcanic Province (offshore northeast Queensland) 120-105 Ma. Volcanic debris was distributed thousands of kilometres inland by wind and palaeo-rivers, as far south as the Otway and Gippsland basins off Australia's southern margin (Bryan et al., 1997; Norvick et al., 2001).

Geodynamic modelling of Cretaceous subduction 23º east of the reconstructed eastern Australian margin successfully predicts accelerated subsidence in the Eromanga and Surat basins at 120 Ma. These findings are in agreement with well data and seismic tomography, and are consistent with earlier Late Palaeozoic-Early Triassic subduction trends in eastern Australia (Holcombe et al., 1997; Jenkins et al., 2002). The Cretaceous convergent margin during the Cretaceous is therefore likely to have resembled the present-day Aleutian Trench with subduction separated from the coast of eastern Russia. These results further reveal that timing of subsidence depends critically on plate kinematic reconstructions.

6.3 Tertiary Subduction in the Southwest Pacific

The modelled present-day temperature structure of the upper mantle mantle beneath the South Fiji Basin is in good agreement with seismic tomography. This highlights successful modelling of Tonga-Kermadec subduction since the Early Tertiary, and illustrates that our *CitcomS* models are spatially and temporally robust. P- and S-wave seismic tomography models reveal a large high-velocity anomaly beneath the Tasman Sea, northwest of New Zealand between ~1000-1400 km depth (Figure 48). The signal is roughly NW-SE trending, and forms part of a larger N-S trending anomaly that extends in the north to approximately 10ºS. As the southwest Pacific has had a highly complex tectonic history, having been influenced by multiple episodes of subduction and extensive back-arc basin formation since the Late Cretaceous, determining the origin of this material is not straightforward.

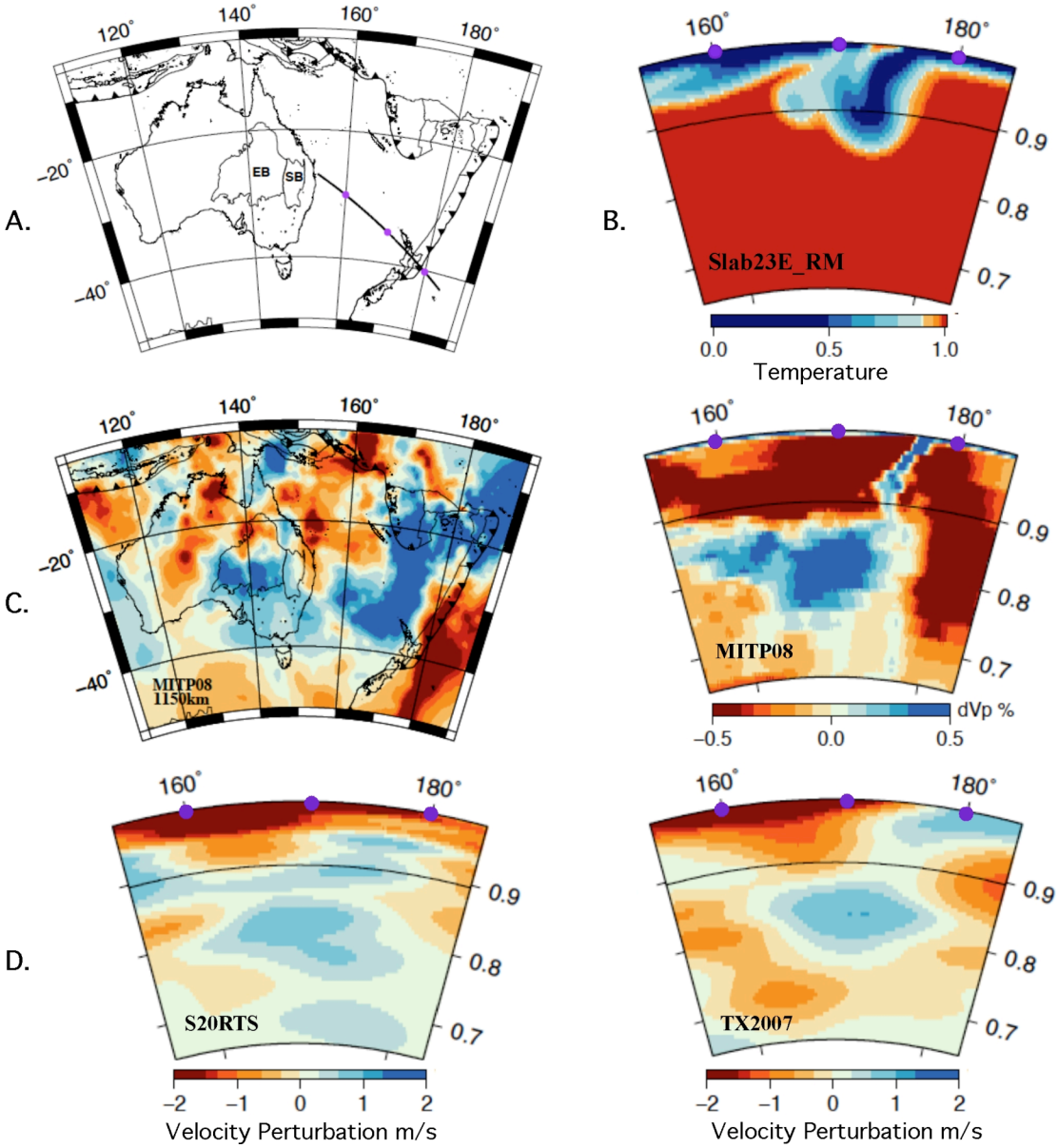

Figure 48. (A) Location map showing profiles of modelled mantle temperature structure and seismic tomography. (B) Cross-section of present-day modelled mantle temperature structure (reference model with subduction shifted east, model Slab23E_RM – see Table 8). (C) Depth slice at 1150 km, and cross-section through the P-wave tomography model MITP08 (Li et al., 2008). (D) Cross-sections through S-wave seismic tomography models S20RTS and TX2007, respectively (Ritsema et al., 1999; Simmons et al., 2007). Seismic tomography reveals a distinctive mass of high-velocity material between ~1000-1400 km depth beneath the Tasman Sea, northwest of the North Island of New Zealand. The modelled slab material penetrates to ~1000 km depth in the same region, between 170-180ºE. See Appendix 5 for a complete set of depth slices through model MITP08. Note: Cross-sectional depths are non-dimensionalised, black line is the 660 km phase boundary, 0.8=1200km depth and 0.7=1900 km depth.

The exact nature of Early Tertiary subduction in the southwest Pacific remains controversial, with disagreement over the location, timing and polarity of subduction.

Several authors propose that east to northeast dipping subduction occurred between ~50-26 Ma along the "New Caledonia subduction zone", contemporaneous with westward dipping Tonga-Kermadec subduction (Schellart et al., 2006; Schellart, 2007; Schellart et al., 2009). While other authors argue in favour of separate subduction zones, for example Sdrolias et al. (2003) propose a tectonic model with longer lived eastward dipping subduction (initiating in the Late Cretaceous) preceding the initiation of westward dipping Tonga-Kermadec subduction at ~45 Ma, or no eastward-dipping subduction at all (e.g. Yan and Koenke 1993). Our *CitcomS* models incorporate westward dipping subduction from 45 Ma to the present (Tonga-Kermadec subduction) and east to northeast dipping subduction from 50-26 Ma (New Caledonia subduction). The latter subduction zone spans from New Caledonia to Northland and terminates earlier in the north. However, our implementation of the "New Caledonia subduction zone" does not involve as much rollback as that suggested by Schellart et al. (2009).

A NW-SE trending cross-section of the modelled mantle temperature structure reveals that subducted slab material preserves the same shape, yet does not quite penetrate as deeply, as the high-velocity seismic tomography anomaly beneath the Tasman Sea (Figure 48). The mantle structure in this region is dominated by 45 Myr old Tonga-Kermadec subduction, with a large volume of subducted slab material (~1000-2200 km) resulting from this westward dipping subduction zone. Although the subducted slab does not penetrate as deeply as is inferred from seismic tomography models (Figure 48), we suggest that our mantle rheological parameters may have reduced the depth penetration of the Tonga-Kermadec slab. From Figure 48 it can be seen that the lower edge of the slab appears to be curling up in the transition zone, in response to descending into the lower mantle. Our mantle viscosity and Clapeyron slope values are within, yet towards the higher end of inferred values, therefore there is ample room to simulate a lower mantle less resistant to slab descent in this region. Such a model could easily reproduce most of the slab material imaged beneath the Tasman Sea in the upper part of the lower mantle (Figure 48). This suggests that eastward dipping subduction is not necessarily required to produce this deep high-velocity anomaly mapped by seismic tomography.

The Pacific-Australian convergence rates are very well known for the last 50 million years. There is little room for major errors with regard to plate convergence velocities during this time interval. Consequently, clarifying Cenozoic plate boundary locations and

configurations in the Tasman sea, and further refinement of mantle rheological parameters will be the key to resolving the origin of this deep high-velocity tomography anomaly.

7 Conclusions

We demonstrate that geodynamic models driven by plate kinematics and linked to geological and geophysical observations, can be used to test alternative plate boundary scenarios and to unravel the driving mechanisms and history of intracontinental basin evolution. Our results have constrained the location of the subduction zone that paralleled Eastern Gondwanaland during the Cretaceous, to approximately 23º east of the reconstructed continental margin. The subduction zone at this time was therefore located east of Gondwanaland's margin by more than 1000 km, analogous to the present day Aleutian Trench that is separated from eastern Russia by the Bering Sea. When this plate boundary configuration is assimilated into geodynamic forward models of the Australian region since 140 Ma, Early Cretaceous accelerated subsidence in the Eromanga and Surat basins in eastern Australia is reproduced, consistent with geological data. The modelled present-day mantle beneath eastern Australia, and as far east as the South Fiji Basin, matches S- and P-wave seismic tomography models. This highlights the temporal and spatial robustness of the model.

The timing of continental subsidence and uplift events is highly sensitive to plate boundary configurations. While mantle material rheological parameters exert significant control over the rate and magnitude of vertical motions; this is largely a consequence of their influence over resistance to slab descent. Further refinement of mantle parameters, such as reducing the initial depth penetration of the slab at 140 Ma, will likely reproduce the 100 Ma subsidence acceleration in the Eromanga Basin that is not currently captured by the models. We propose that following the accumulation of slab material at the 660 km phase boundary, mantle avalanching may have triggered a rapid increase in the rate of subsidence that preceded widespread Late Cretaceous uplift of eastern Australia. Regardless, the absence of Jurassic and Cretaceous extensional faulting in the Eromanga and Surat basins, further supports the mantle dynamic nature of Cretaceous vertical motions.

We have demonstrated that geodynamic models coupled with high-performance computing enable the development of "holistic" earth models that reconcile deep Earth structure with plate boundary reconstructions and geological observations such as tectonic subsidence and basin stratigraphy. The workflow we have developed (Appendix 6) is also highly

adaptable, and applying it to other regions of the globe will facilitate attempts to constrain plate boundary reconstructions elsewhere in time and space.

8 References

Anderson, D. L. (1994), Superplumes or supercontinents?, *Geology*, *22*(1), 39-42.

Armstrong, J. D., and T. M. Barr (1986), The Eromanga Basin, an overview of exploration and potential, in *Contributions to the Geology and Hydrocarbon Potential of the Eromanga Basin*, edited by D. I. Gravestock, P. S. Moore and G. M. Pitt, Geological Society of Australia Inc.

Billen, M. I., and M. Gurnis (2001), A low viscosity wedge in subduction zones, *Earth and Planetary Science Letters*, *193*(1-2), 227-236.

Billen, M. I., and M. Gurnis (2003), Multiscale dynamics of the Tonga-Kermadec subduction zone, *Geophysical Journal International*, *153*(2), 359-388.

Bina, C. R., and G. Helffrich (1994), Phase transition Clapeyron slopes and transition zone seismic discontinuity topography, *Journal of Geophysical Research*, *99*, 15853-15860.

Boyden, J., R. D. Müller, M. Gurnis, T. Torsvik, J. Clark, M. Turner, H. Ivey-Law, J. Farrow, and R. Watson (2009), Next-generation plate-tectonic reconstructions using GPlates, in *Geoinformatics: Cyberinfrastructure for the Solid Earth Sciences*, edited by G. R. Keller and C. Baru, Cambridge University Press, Cambridge.

Bradshaw, J. D. (1989), Cretaceous geotectonic patterns in the New Zealand region, *Tectonics*, *8*(4), 803-820.

Bryan, S. E., A. E. Constantine, C. J. Stephens, A. Ewart, R. W. Schön, and J. Parianos (1997), Early Cretaceous volcano-sedimentary successions along the eastern Australian continental margin: Implications for the break-up of eastern Gondwana, *Earth and Planetary Science Letters*, *153*(1-2), 85-102.

Burgess, P. M., M. Gurnis, and L. Moresi (1997), Formation of sequences in the cratonic interior of North America by interaction between mantle, eustatic, and stratigraphic processes, *Geological Society of America Bulletin*, *109*(12), 1515-1535.

Cande, S. C., and D. V. Kent (1995), Revised calibration of the geomagnetic polarity timescale for the Late Cretaceous and Cenozoic, *Journal of Geophysical Research*, *100*, 6093-6095.

Christensen, U. R. (1996), The influence of trench migration on slab penetration into the lower mantle, *Earth and Planetary Science Letters*, *140*(1-4), 27-39.

Coakley, B., and M. Gurnis (1995), Far-field tilting of Laurentia during the Ordovician and constraints on the evolution of a slab under an ancient continent, *Journal of Geophysical Research*, *100*.

Conrad, C. P., and L. Husson (2009), Influence of dynamic topography on sea level and its rate of change, *Lithosphere*, *1*(2), 110-120.

Crosby, A. G. (2007), Aspects of the relationship between depth and age on the Earth and Moon, PhD thesis, 220 pp, University of Cambridge, Cambridge.

Davies, G. F. (1999), *Dynamic Earth: Plates, Plumes and Mantle Convection*, Cambridge University Press.

DiCaprio, L. (2009), The Geodynamic History of the Australian Region Since the Cretaceous, 182 pp, The University of Sydney, Sydney.

DiCaprio, L., M. Gurnis, and R. D. Müller (2009), Long-wavelength tilting of the Australian continent since the Late Cretaceous, *Earth and Planetary Science Letters*, *278*(3-4), 175-185.

DiCaprio, L., R. D. Müller, and M. Gurnis (In Press), A dynamic process for drowning carbonate reefs on the Norheastern Australian margin, *Geology*

Draper, J. J. (2002), *Geology of the Cooper and Eromanga Basins, Queensland*, 85 pp., Queensland Department of Natural Resources and Mines.

Dziewonski, A. M., and D. L. Anderson (1981), Preliminary reference Earth model, *Physics of The Earth and Planetary Interiors*, *25*(4), 297-356.

Ewart, A., R. W. Schon, and B. W. Chappell (1992), The Cretaceous volcanic-plutonic province of the central Queensland (Australia) coast - a rift related 'calc-alkaline' prvince, *Transactions of the Royal Society of Edinburgh: Earth Sciences*, *83*, 327-345.

Exon, N. F. (1976), *Geology of the Surat Basin in Queensland*, Bureau of Mineral Resources, Australia - Bulletin 166.

Exon, N. F., and B. R. Senior (1976), The Cretaceous of the Eromanga and Surat Basins, *Bureau of Mineral Resources Journal of Australian Geology and Geophysics 1*, 33-50.

Gallagher, K. (1990), Permian to Cretaceous subsidence history along the Eromanga-Brisbane Geoscience Transect, in *The Eromanga-Brisbane Geoscience Transect: A guide to basin development across Phanerozoic Australia*, edited by F. D.M., pp. 133-151, Southern Queensland Bureau of Mineral Resources, Australia.

Gallagher, K., and K. Lambeck (1989), Subsidence, sedimentation and sea-level changes in the Eromanga Basin, Australia, *Basin Research*, *2*(2), 115-131.

Gallagher, K., T. A. Dumitru, and A. J. W. Gleadow (1994), Constraints on the vertical motion of eastern Australia during the Mesozoic, *Basin Research*, *6*(2-3), 77-94.

Goes, S., F. A. Capitanio, and G. Morra (2008), Evidence of lower-mantle slab penetration phases in plate motions, *Nature*, *451*(7181), 981-984.

Gradstein, F. M., F. P. Agterberg, J. G. Ogg, J. Hardenbol, P. van Veen, J. Thierry, and Z. Huang (1994), A Mesozoic time scale, *Journal of Geophysical Research*, *99*, 24051-24074.

Grand, S. P. (2002), Mantle shear-wave tomography and the fate of subducted slabs, *Philosophical Transactions of the Royal Society of London. Series A: Mathematical, Physical and Engineering Sciences*, *360*(1800), 2475-2491.

Gurnis, M. (1990), Bounds on global dynamic topography from Phanerozoic flooding of continental platforms, *Nature*, *344*(6268), 754-756.

Gurnis, M., and B. H. Hager (1988), Controls of the structure of subducted slabs, *Nature*, *335*(6188), 317-321.

Gurnis, M., R. D. Müller, and L. Moresi (1998), Cretaceous vertical motion of Australia and the Australian-Antarctic Discordance, *Science*, *279*(5356), 1499-1504.

Gurnis, M., J. Mitrovica, J. Ritsema, and H.-J. van Heijst (2000), Constraining mantle density structure using geological evidence of surface uplift rates: The case of the African superplume, *Geochemistry, Geophysics, Geosystems*, *1*(7).

Gurnis, M., M. Turner, L. DiCaprio, S. Spasojevic, R. D. Müller, J. Boyden, M. Seton, V. C. Manea, and D. J. Bower (2009), Global plate reconstructions with continuously closing plates, *Geochemistry, Geophysics, Geosystems (submitted)*, *Special theme "Plate Reconstructions, Mantle Convection, and Tomography Models: A Complementary Vision of Earth's Interior"*.

Harland, W. B., A. V. Cox, P. G. Llewellyn, C. A. G. Pickton, A. G. Smith, and R. Walters (1982), *A Geologic Time Scale*, Cambridge University Press, Cambridge.

Holcombe, R. J., C. J. Stephens, C. R. Fielding, D. Gust, T. A. Little, R. Sliwa, J. Kassan, J. McPhie, and A. Ewart (Eds.) (1997), *Tectonic evolution of the northern New England Fold Belt: The Permian-Triassic Hunter-Bowen event*, 14 pp., Geological Society of Australia, Special Publication 19.

Horton, D. (2002), Australian sedimentary opal: why is Australia unique?, *The Australian Gemmologist*, *21*, 287-294.

Hughes, T. J. R. (1987), *The Finite Element Method: Linear Static and Dynamic Finite Element Analysis*, 672 pp., Prentice-Hall Inc, Englewood Cliffs, New Jersey.

Ita, J., and L. Stixrude (1992), Petrology, Elasticity, and Composition of the Mantle Transition Zone, *Journal of Geophysical Research*, *97*, 6849-6866.

Jenkins, R. B., B. Landenberger, and W. J. Collins (2002), Late Palaeozoic retreating and advancing subduction boundary in the New England Fold Belt, New South Wales, *Australian Journal of Earth Sciences*, *49*(3), 467-489.

Katsura, T., H. Yamada, T. Shinmei, A. Kubo, S. Ono, M. Kanzaki, A. Yoneda, M. J. Walter, E. Ito, S. Urakawa, K. Funakoshi, and W. Utsumi (2003), Post-spinel transition in Mg2SiO4 determined by high P-T in situ X-ray diffractometry, *Physics of The Earth and Planetary Interiors*, *136*(1-2), 11-24.

Katsura, T., H. Yamada, O. Nishikawa, M. Song, A. Kubo, T. Shinmei, S. Yokoshi, Y. Aizawa, T. Yoshino, M. J. Walter, E. Ito, and K.-i. Funakoshi (2004), Olivine-wadsleyite transition in the system (Mg,Fe)2SiO4, *Journal of Geophysical Research*, *109*.

Korsch, R. J., and J. M. Totterdell (2009), Subsidence history and basin phases of the Bowen, Gunnedah and Surat Basins, eastern Australia, *Australian Journal of Earth Sciences*, *56*(3), 335 - 353.

Korsch, R. J., J. M. Totterdell, T. Fomin, and M. G. Nicoll (2009), Contractional structures and deformational events in the Bowen, Gunnedah and Surat Basins, eastern Australia, *Australian Journal of Earth Sciences*, *56*(3), 477 - 499.

Krassay, A. A., and J. M. Totterdell (2003), Seismic stratigraphy of a large, Cretaceous shelf-margin delta complex, offshore southern Australia, *AAPG Bulletin*, *87*(6), 935-963.

Laird, M. G., and J. D. Bradshaw (2004), The Break-up of a Long-term Relationship: the Cretaceous Separation of New Zealand from Gondwana, *Gondwana Research*, *7*(1), 273-286.

Leitch, E. C. (1975), Plate Tectonic Interpretation of the Paleozoic History of the New England Fold Belt, *Geological Society of America Bulletin*, *86*(1), 141-144.

Li, C., R. D. van der Hilst, E. R. Engdahl, and S. Burdick (2008), A new global model for P wave speed variations in Earth's mantle, *Geochemistry, Geophysics, Geosystems*, *9*.

Lithgow-Bertelloni, C., and M. Gurnis (1997), Cenozoic subsidence and uplift of continents from time-varying dynamic topography, *Geology*, *25*(8), 735-738.

Lithgow-Bertelloni, C., and P. G. Silver (1998), Dynamic topography, plate driving forces and the African superswell, *Nature*, *395*(6699), 269-272.

Liu, L., S. Spasojevic, and M. Gurnis (2008), Reconstructing Farallon plate subduction beneath North America back to the Late Cretaceous, *Science*, *322*(5903), 934-938.

Manea, V., and M. Gurnis (2007), Subduction zone evolution and low viscosity wedges and channels, *Earth and Planetary Science Letters*, *264*(1-2), 22-45.

McNamara, A. K., and S. Zhong (2004), Thermochemical structures within a spherical mantle: Superplumes or piles?, *Journal of Geophysical Research*, *109*.

McPhie, J. (1987), Andean analogue for the Late Carboniferous volcanis arc and arc flank environments of the western New England Orogen, New South Wales, Australia, *Tectonophysics*, *138*, 269-288.

Mitrovica, J. X., C. Beaumont, and G. T. Jarvis (1989), Tilting of continental interiors by the dynamical effects of subduction, *Tectonics*, *8*(5), 1079-1094.

Montelli, R., G. Nolet, F. A. Dahlen, and G. Masters (2006), A catalogue of deep mantle plumes: New results from finite-frequency tomography, *Geochemistry, Geophysics, Geosystems*, *7*.

Morishima, H., T. Kato, M. Suto, E. Ohtani, S. Urakawa, W. Utsumi, O. Shimomura, and T. Kikegawa (1994), The Phase Boundary Between α- and β-Mg2SiO4 Determined by in Situ X-ray Observation, *Science*, *265*(5176), 1202-1203.

Morra, G., K. Regenauer-Lieb, and D. Giardini (2006), Curvature of oceanic arcs, *Geology*, *34*(10), 877-880.

Müller, R. D., W. R. Roest, and J. Y. Royer (1998), Asymmetric sea-floor spreading caused by ridge-plume interactions, *Nature*, *396*(6710), 455-459.

Müller, R. D., M. Sdrolias, C. Gaina, and W. R. Roest (2008a), Age, spreading rates and spreading asymmetry of the world's ocean crust, *Geochemistry, Geophysics, Geosystems*, *9*(4), Q04006, doi:04010.01029/02007GC001743

Müller, R. D., M. Sdrolias, C. Gaina, B. Steinberger, and C. Heine (2008b), Long-Term Sea-Level Fluctuations Driven by Ocean Basin Dynamics, *Science*, *319*(5868), 1357-1362.

Norvick, M. S., M. A. Smith, and M. R. Power (2001), The Plate Tectonic Evolution of Eastern Australasia Guided by the Stratigraphy of the Gippsland Basin, in *Eastern Australasian Basins Symposium, A Refocused Energy Perspective for the Future*, edited by K. C. Hill and T. Bernecker, pp. 15-23, Petroleum Exploration Society of Australia, Special Publication.

Nyblade, A. A., and S. W. Robinson (1994), The African Superswell, *Geophysical Research Letters*, *21*(9), 765-768.

O'Neill, C., D. Müller, and B. Steinberger (2005), On the uncertainties in hot spot reconstructions and the significance of moving hot spot reference frames, *Geochemistry, Geophysics, Geosystems*, *6*.

Peacock, S. M. (1990), Fluid processes in subduction zones, *Science*, *248*(4953), 329-337.

Pysklywec, R. N., and J. X. Mitrovica (1997), Mantle avalanches and the dynamic topography of continents, *Earth and Planetary Science Letters*, *148*(3-4), 447-455.

Pysklywec, R. N., and J. X. Mitrovica (1998), Mantle flow mechanisms for the large-scale subsidence of continental interiors, *Geology*, *26*(8), 687-690.

Ranero, C. R., J. Phipps-Morgan, K. McIntosh, and C. Reichert (2003), Bending-related faulting and mantle serpentinization at the Middle America trench, *Nature*, *425*(6956), 367-373.

Raza, A., K. C. Hill, and R. J. Korsch (2009), Mid-Cretaceous uplift and denudation of the Bowen and Surat Basins, eastern Australia: relationship to Tasman Sea rifting from apatite fission-track and vitrinite-reflectance data, *Australian Journal of Earth Sciences*, *56*(3), 501 - 531.

Ritsema, J., H. J. v. Heijst, and J. H. Woodhouse (1999), Complex Shear Wave Velocity Structure Imaged Beneath Africa and Iceland, *Science*, *286*(5446), 1925-1928.

Romanowicz, B. (2003), GLOBAL MANTLE TOMOGRAPHY: Progress Status in the Past 10 Years, *Annual Review of Earth and Planetary Sciences*, *31*(1), 303-328.

Romanowicz, B. (2008), Using seismic waves to image Earth's internal structure, *Nature*, *451*(7176), 266-268.

Russell, M., and M. Gurnis (1994), The planform of epeirogeny: Vertical motions of Australia during the Cretaceous, *Basin Research*, *6*(2-3), 63-76.

Sandiford, M. (2007), The tilting continent: A new constraint on the dynamic topographic field from Australia, *Earth and Planetary Science Letters*, *261*(1-2), 152-163.

Schellart, W. P. (2007), North-eastward subduction followed by slab detachment to explain ophiolite obduction and Early Miocene volcanism in Northland, New Zealand, *Terra Nova*, *19*(3), 211-218.

Schellart, W. P., G. S. Lister, and V. G. Toy (2006), A Late Cretaceous and Cenozoic reconstruction of the Southwest Pacific region: Tectonics controlled by subduction and slab rollback processes, *Earth-Science Reviews*, *76*(3-4), 191-233.

Schellart, W. P., B. L. N. Kennett, W. Spakman, and M. Amaru (2009), Plate reconstructions and tomography reveal a fossil lower mantle slab below the Tasman Sea, *Earth and Planetary Science Letters*, *278*(3-4), 143-151.

Sclater, J. G., C. Jaupart, and D. Galson (1980), The Heat Flow Through Oceanic and Continental Crust and the Heat Loss of the Earth, *Rev. Geophys.*, *18*(1), 269-311.

Sdrolias, M., R. D. Müller, and C. Gaina (2003), Tectonic evolution of the southwest Pacific using constraints from back-arc basins, in *Evolution and Dynamics of the Australian Plate*, edited by H. R. R. and R. D. Müller, Geological Society of Australia Special Publication 22 and Geological Society of America Special Paper 372, 343-359.

Senior, B. R., A. Mond, and P. L. Harrison (1978), *Geology of the Eromanga Basin*, Bureau of Mineral Resources, Australia - Bulletin 167.

Simmons, N. A., A. M. Forte, and S. P. Grand (2007), Thermochemical structure and dynamics of the African superplume, *Geophysical Research Letters*, *34*.

Spasojević, S., L. Liu, M. Gurnis, and R. D. Müller (2008), The case for dynamic subsidence of the U.S. east coast since the Eocene, *Geophysical Research Letters*, *35*.

Steckler, M. S., and A. B. Watts (1978), Subsidence of the Atlantic-type continental margin off New York, *Earth and Planetary Science Letters*, *41*(1), 1-13.

Steinberger, B. (2007), Effects of latent heat release at phase boundaries on flow in the Earth's mantle, phase boundary topography and dynamic topography at the Earth's surface, *Physics of the Earth and Planetary Interiors*, *164*, 2-20.

Stevenson, D. J., and J. S. Turner (1977), Angle of subduction, *Nature*, *270*(5635), 334-336.

Tan, E., M. Gurnis, and L. Han (2002), Slabs in the lower mantle and their modulation of plume formation, *Geochemistry, Geophysics, Geosystems*, *3*.

Tan, E., E. Choi, P. Thoutireddy, M. Gurnis, and M. Aivazis (2006), GeoFramework: Coupling multiple models of mantle convection within a computational framework, *Geochemistry, Geophysics, Geosystems*, *7*.

Tatsumi, Y., M. Sakuyama, H. Fukuyama, and I. Kushiro (1983), Generation of Arc Basalt Magmas and Thermal Structure of the Mantle Wedge in Subduction Zones, *Journal of Geophysical Research*, *88(B7)*.

Torsvik, T. H., R. D. Müller, R. Van der Voo, B. Steinberger, and C. Gaina (2008), Global plate motion frames: Toward a unified model, *Rev. Geophys.*, *46*.

Tovish, A., G. Schubert, and B. P. Luyendyk (1978), Mantle flow pressure and the angle of subduction: non-Newtonian corner flows, *Journal of Geophysical Research*, *83*, 5892-5898.

Tulloch, A. J., and D. L. Kimbrough (1989), The Paparoa metamorphic core complex, New Zealand: Cretaceous extension associated with fragmentation of the Pacific margin of Gondwana, *Tectonics*, *8*(6), 1217-1234.

Turcotte, D. L., and G. Schubert (2002), *Geodynamics* 2ed., Cambridge University Press, Cambridge.

Veevers, J. J. (1982), Australian-Antarctic depression from the mid-ocean ridge to adjacent continents, *Nature*, *295*(5847), 315-317.

Veevers, J. J. (1984), *Phanerozoic Earth History of Australia*, 418 pp., Oxford University Press, New York.

Veevers, J. J. (2000), *Billion-year earth history of Australia and neighbours in Gondwanaland*, xi, 388 pp., Gemoc Press, North Ryde, N.S.W.

Vry, J. K., J. Baker, R. Maas, T. A. Little, R. Grapes, and M. Dixon (2004), Zoned (Cretaceous and Cenozoic) garnet and the timing of high grade metamorphism, Southern Alps, New Zealand, *Journal of Metamorphic Geology*, *22*(3), 137-157.

Waschbusch, P., R. J. Korsch, and C. Beaumont (2009), Geodynamic modelling of aspects of the Bowen, Gunnedah, Surat and Eromanga Basins from the perspective of convergent margin processes, *Australian Journal of Earth Sciences*, *56*(3), 309 - 334.

Wessel, P., Y. Harada, and L. W. Kroenke (2006), Toward a self-consistent, high-resolution absolute plate motion model for the Pacific, *Geochemistry, Geophysics, Geosystems*, *7*.

Wheeler, P., and N. White (2000), Quest for dynamic topography: Observations from Southeast Asia, *Geology*, *28*(11), 963-966.

Yan, C. Y., and L. W. Kroenke (1993), A plate tectonic reconstruction of the southwest Pacific, 0-100 Ma, in *Proceedings of the Ocean Drilling Program, Scientific Results*, edited by W. H. Berger, L. W. Kroenke and L. W. Mayer, Ocean Drilling Program, Texas A&M University, College Station, Texas.

Zhong, S., and M. Gurnis (1997), Dynamic interaction between tectonic plates, subducting slabs, and the mantle, *Earth Interactions*, *1*(3), 1-18.

Zhong, S., M. T. Zuber, L. Moresi, and M. Gurnis (2000), Role of temperature-dependent viscosity and surface plates in spherical shell models of mantle convection, *Journal of Geophysical Research*, *105(B5)*, 11063-11082.

9 Appendices

Please see 'Digital Appendices' CD located on the inside of the back cover of this thesis.

9.1 Appendix 1 – Complete Set of CitcomS Models

9.2 Appendix 2 – Complete Set of Borehole Tectonic Subsidence Curves

9.3 Appendix 3 – Complete Set of Modelled Tectonic Subsidence Curves

9.4 Appendix 4 – Complete Set of Figures Showing Modelled Versus Observed Tectonic Subsidence

9.5 Appendix 5 – Depth Slices Through Tomography Model MITP08 (Li et al., 2008)

9.6 Appendix 6 – Collection of Scripts Used to Generate Models, and Post-process and Visualise Output